SEP. - DEC. 2024 • Volume XXV Number

THE ASEAN

JOURNAL OF RADIOLOGY

Highlight

- Original Article
- Case Report
- Review Article
- ASEAN Movement in Radiology
- Memorial

Official Journal of The

Royal College of Radiologists of Thailand

Radiological Society of Thailand

Foundation for Orphan and Rare Lung Disease

Thai Society of Vascular and Intervention Radiology

ASEAN Association of Radiology

ASEAN

JOURNAL OF RADIOLOGY

ISSN 2672-9393

The ASEAN
Journal of Radiology

Editor: *Wiwatana Tanomkiat, M.D.*
Associate Editors: *Pham Minh Thong, M.D., Ph.D.*
Narufumi Suganuma, M.D., Ph.D.
Kwan Hoong Ng, Ph.D.
Keerati Hongsakul, M.D.
Siriporn Hirunpat, M.D.
Chang Yueh Ho, M.D.
Maung Maung Soe, M.D.
Kyaw Zaya, M.D.
Assistant Editor: *Nucharin Supakul, M.D.*
Statistical Consultant: *Alan Frederick Geater, B.Sc., Ph.D.*
Language Consultant: *Siriprapa Saparat, EIL*
Publishing Consultant: *Ratchada Chalarat, M.A.*
Editorial Coordinator: *Supakorn Yuenyongwannachot, B.A., M.Sc.*
Graphics: *Kowa Saeooi, B.A.*

Publisher: *Foundation for Orphan and Rare Lung Disease*

CONTENTS

From The Editor

Original Article

Case Report

Review Article

ASEAN Movement in Radiology

Memorial

From The Editor

COVID-19 boosted not only digital health but also cyber crimes

Received 25 December 2024; accepted 25 December 2024
doi:10.46475/asean-jr.v25i3.932

Thailand, the country in the top three of the highest road accidents causing an average of 17,914 fatalities each year, mourned a tragic incident near Bangkok on 1 October [1]. The fire broke out on a coach bus carrying 44 students and teachers during a field trip; 20 students' and 3 teachers' lives were lost, while three others were injured. It was revealed that the bus involved in the fire had been in operation for over 50 years and had undergone several unauthorized modifications, including being improperly converted to gas-powered vehicles, with far more cylinders than legally permitted. What contributed to the accident is that one of the 11 illegally installed gas tanks had come loose, causing a gas leak from a connecting pipe, and the front axle had broken, dragging against the road and sparking the fire [2]. That was not an isolating incidence. Past accidents include a 2019 bus crash in Eastern Thailand with one fatality and 24 injuries, and another in Southern Thailand last year, injuring 25 students. Earlier this year, a similar incident in central Thailand resulted in 25 injuries [3]. In fact, over the past decade, more than 26,930 children have tragically died in road crashes which accounts for one in three child deaths in Thailand, highlighting the severity of the problem [4]. The blaze, which consumed a 54-year-old bus, underscored severe safety lapses, prompting an immediate governmental action. Crucial safety measures, including comprehensive inspections of all 13,426 CNG buses and heightened safety protocols for non-regular buses, were announced [5].

COVID-19 pandemic boosted not only the digital medical service but also everything digitally reformed, including E-commerce and scams. Social media influencers became online business owners and cultivated an image of trustworthiness by showcasing an extravagant lifestyle and inviting numerous Thai celebrities or other influencers to be their business partners or appear in their personal events. Jaw-dropping promotions or benefits were launched to attract attentions initially but the victims later lost their money when they placed further orders. There were 2 gold retailers involving more than 300 victims reporting to the Cyber Crime Investigation Bureau in October [6]. A company attracted more than 300,000 investors by its online advertisements along with social media campaigns, enticed by the promise of high profits and celebrity endorsements [7]. However, after investing large amounts of money, they found they couldn't sell the company's merchandise but were instead urged to bring in more investors. Some victims even resorted to taking loans or selling their possessions to fund their investment. Many ended up losing their life savings. The victims claimed that the company was operating a pyramid scheme, where earnings came primarily from recruiting more members than from selling products or services. In a significant move to bolster consumer protection, a new law in Thailand now permits online shoppers to examine their packages before making payment. This regulation came into force on October 3, allowing recipients to return the entire batch of goods within five days and must be refunded within 15 days as long as the complaint is validated [8]. Thailand is the country in the axis of continental South East Asia which shares the longest borders of Myanmar (2, 202 kms), Laos (1, 750 kms), Cambodia (798 kms), and Malaysia (576 kms). These far-reaching borders are the perfect places for criminal networks to escape the constraints of law enforcement to operate industrial-scale scam compounds. In addition, at the border between Thailand and Myanmar where majorities are Myanmar ethnic minorities who have unique regional conditions which cause internal political conflicts between groups or with the central government, the dimensions of the networks, initially based on illegal online gambling, are getting even more complex. The investors, laborers, operations and victims of the crimes seem to be transnational. It is estimated that most laborers are forced and trafficked from more than 60 countries around the world as well as the victims who lost money. The funds stolen by these cyber scamming is calculated to likely exceed 43.8 billion US dollars a year. Relationships between these criminal groups and the governments are being investigated as the stolen funds are almost 40% of some countries' GDP and the complex money-laundering operations to move funds into the formal economy is beyond the scale of the criminal organization [9].

The President of Malaysian College of Radiology, the President of Vietnamese Society of Radiology and Nuclear Medicine, the representative from the Philippine College of Radiology, the representatives from the Chinese Society of Radiology, and the editor as the representative from the Radiological Society of Thailand in the Belt-Road-Initiative session on 16 November 2024 at the Chinese Congress of Radiology, Shanghai, China.

China is thought to be the most influential country in the ASEAN region [10]. Belt-Road-Initiative (BRI), once one of the strategies to drive economic and political power into the region, now expands to education and cultures. As also the president of the Radiological Society of Thailand, the editor was invited to give a talk in "Belt-Road-Initiative session" in the Chinese Congress of Radiology (CCR) held on 14-17 November 2024 in Shanghai, China.

In 2025, The ASEAN Journal of Radiology will publish 3 issues a year, with the first issue in January, the second issue in May, and the third issue in September. On behalf of the editorial board, I would like to extend my sincere appreciation for your valuable contributions and really hope that The ASEAN Journal of Radiology will be a platform for the scholar community of Radiology in ASEAN countries and beyond.

I sincerely wish all the readers, authors, our valued reviewers, and editors a prosperous 2025.

Wiwatana Tanomkiat, M.D.
Editor,
The ASEAN Journal of Radiology
Email: aseanjournalradiology@gmail.com

References

1. ASEAN NOW [Internet]. Bangkok: The Thaiger; c2002-2024 [cited 2024 Dec 25]. Deadly bus fire tragedy highlights safety failures on Thai roads. Available from: https://aseannow.com/topic/1340104-deadly-bus-fire-tragedy-highlights-safety-failures-on-thai-roads/?utm_source=241008-11

2. ASEAN NOW [Internet]. Bangkok: The Thaiger; c2002-2024 [cited 2024 Dec 25]. Transport department clarifies fatal bus fire incident to committee: CNG leak confirmed. Available from: https://aseannow.com/topic/1339748-transport-department-clarifies-fatal-bus-fire-incident-to-committee-cng-leak-confirmed/?utm_source=241004-03

3. ASEAN NOW [Internet]. Bangkok: The Thaiger; c2002-2024 [cited 2024 Dec 25]. Thai school cancels field trip after tragic bus fire Incident. Available from: https://aseannow.com/topic/1339660-thai-school-cancels-field-trip-after-tragic-bus-fire-incident/?utm_source=241003-03

4. ASEAN NOW [Internet]. Bangkok: The Thaiger; c2002-2024 [cited 2024 Dec 25]. Save the children urges action on child road deaths in Thailand. Available from: https://aseannow.com/topic/1339708-save-the-children-urges-action-on-child-road-deaths-in-thailand/?utm_source=241003-10

5. ASEAN NOW [Internet]. Bangkok: The Thaiger; c2002-2024 [cited 2024 Dec 25]. School bus fire claims multiple lives and injures young students in Rangsit. Available from: https://aseannow.com/topic/1339544-school-bus-fire-claims-multiple-lives-and-injures-young-students-in-rangsit/page/9/#comment-19276877

6. ASEAN NOW [Internet]. Bangkok: The Thaiger; c2002-2024 [cited 2024 Dec 25]. Fraudulent gold sales: E-commerce couple face charges. Available from: https://aseannow.com/topic/1340626-fraudulent-gold-sales-e-commerce-couple-face-charges/?utm_source=241014-20#google_vignette

7. ASEAN NOW [Internet]. Bangkok: The Thaiger; c2002-2024 [cited 2024 Dec 25]. Alleged MLM scam victims press charges against celebrities, company. Available from: h ttps://aseannow.com/topic/1340360-alleged-mlm-scam-victims-press-charges-against-celebrities-company/

8. ASEAN NOW [Internet]. Bangkok: The Thaiger; c2002-2024 [cited 2024 Dec 25]. New law allows buyers to inspect online orders before payment. Available from: https://aseannow.com/topic/1340203-new-law-allows-buyers-to-inspect-online-orders-before-payment/?utm_source=241009-10

9. The United States Institute of Peace [Internet]. Washington, DC: The Institute; 2024 [cited 2024 Dec 25]. Transnational Crime in Southeast Asia: A growing threat to global peace and security. Available from: https://www.usip.org/publications/2024/05/transnational-crime-southeast-asia-growing-threat-global-peace-and-security

10. Seah S, Lin J, Martinus M, Fong K, Aridati I, Pham TPT, et al. The state of Southeast Asia 2024 survey report. Singapore: ISEAS - Yusof Ishak Institute; 2024 [cited 2024 Dec 25]. Available from: https://www.iseas.edu.sg/wp-content/uploads/2024/03/The-State-of-SEA-2024.pdf

THE ASEAN JOURNAL OF RADIOLOGY
ISSN 2672-9393

Original Article

Differentiation of malignant and benign breast lesions with diffusion-weighted imaging: What is the optimum apparent diffusion coefficient value?

Jenjeera Prueksadee, M.D.[1]
Chawisa Lerdwatanakiet, M.D.[2]
From [1]Department of Radiology, Faculty of Medicine, Chulalongkorn University, Bangkok, Thailand,
[2]Department of Radiology, King Chulalongkorn Memorial Hospital, The Thai Red Cross Society, Bangkok, Thailand.
Address correspondence to J.P. (email: pjenjeera@gmail.com)

Received 9 September 2023; revised 3 August 2024; accepted 5 August 2024
doi:10.46475/asean-jr.v25i3.878

Abstract

Background and objective: To determine the optimum apparent diffusion coefficient (ADC) value in differentiating benign from malignant breast lesions.

Materials and Methods: The study is a retrospective review of the patients who underwent breast magnetic resonance imaging (MRI) at King Chulalongkorn Memorial Hospital between January 2017 and May 2020. ADC values were measured by placement of region of interest (ROI) within the breast lesions using Philips DynaCAD breast analysis system and comparing it with histopathological diagnosis. A receiver-operating-characteristics (ROC) analysis was plotted and the area under the curve (AUC) was evaluated to find the ideal ADC value in the differentiation of benign and malignant breast lesions.

Results: Two hundred and ten lesions in 163 female patients were included in the present study. One hundred twenty-six lesions (60%) were malignant and eighty-four lesions (40%) were benign. The mean ADC values of malignancy (0.913×10^{-3} mm^2/s) were statistically lower than that of benign lesions (1.080×10^{-3} mm^2/s) (mean difference 0.169×10^{-3} mm^2/s, $P < 0.001$). According to the ROC analysis, the optimum cut-off ADC value of 0.991×10^{-3} mm^2/s was an excellent predictor for differentiated benign and malignant breast lesions (AUC = 0.835, sensitivity 78.6%, specificity 82.5%, accuracy 81%, PPV 85.3% and NPV 75%).

Conclusion: Diffusion-weighted imaging (DWI) was an effective MRI sequence to assess breast cancer by using ADC value as a key parameter in addition to other important imaging findings from MRI. The present study showed the mean ADC value of malignancy was statistically significantly lower than that of benign lesions. The cut-off ADC value of 0.991×10^{-3} mm^2/s had good specificity, accuracy, and PPV to differentiate benign from malignant breast lesions.

Keywords: ADC, Benign breast lesion, DWI, Malignant breast lesion, MRI.

Introduction

Breast cancer is the most common cancer in women worldwide and a major leading cause of cancer-related death in women in developing countries [1-2]. Therefore, women must be properly screened to detect breast cancer early to get effective treatment and better outcomes [3].

A mammogram is a common modality for breast cancer screening in average-risk women, but it has lower sensitivity in dense breast tissue [3, 4]. Ultrasound is an additional tool for mammograms in screening dense breasts [5]. However, it is an operator-dependent procedure and limited detection of breast calcifications [6]. Nevertheless, for high-risk women, magnetic resonance imaging (MRI) is highly recommended as a supplement modality [4].

Nowadays, MRI is an essential imaging modality for screening, diagnosis, staging, and follow-up for breast lesions, because of high sensitivity in the detection of breast cancer [7-8]. Diffusion-weighted imaging (DWI) is an advanced MRI technique that provides the apparent diffusion coefficient (ADC) value as a quantitative parameter, measuring the Brownian motion of water molecules within tissues and demonstrating the difference in cellular density, membrane integrity, and tissue microstructure [9-10]. In malignancy, a lower ADC value is commonly reflected due to increased cellular density while a benign lesion has a higher ADC value [8]. Therefore, DWI with ADC value is one of the effective tools to detect malignant breast lesions [11]. Nevertheless, there is no exact specific ADC value to differentiate malignant from benign breast lesions [11-12].

The purpose of this study was to find the optimum ADC value in DWI to accurately predict malignant breast lesions and to determine the ADC values among different types of breast cancers and benign breast lesions.

Materials and methods

Patients and lesions

This retrospective study was approved by the Institutional Review Board of the Faculty of Medicine, Chulalongkorn University, with a waiver of informed consent. Demographic and clinical data were reviewed from the medical records in the hospital information system (HIS).

The study reviews all MRI data of female patients who underwent breast MRI at King Chulalongkorn Memorial Hospital between January 2017 and May 2020. The inclusion criteria were: 1) The size of the focal breast lesion was more than 5 mm, 2) MRI underwent DWI with a b-value of 800 s/mm², and 3) Pathologic or cytologic diagnosis was required in all breast lesions. When more than one pathological result was available for a patient, only the most clinically significant pathological result was recorded.

Patients with a history of chemotherapy, breast intervention, or radiotherapy on the lesion side, or insufficient imaging follow-up period (less than 2 years) were excluded from the study. Lesions with indeterminate pathological results or poor MRI quality such as significant artifacts or inadequate fat suppression were also excluded. A total of 210 lesions in 163 patients were enrolled in this study.

MRI technique

All MRIs were performed using a 1.5-Tesla system with a standard protocol. The pre-contrast sequences are as follows: axial T1-weighted with fat suppression, T2-weighted turbo spin echo (TSE), short-T1 inversion recovery (STIR), and coronal T1-weighted sequences.

Dynamic contrast-enhanced (DCE)-MRI was obtained, using a bolus injection of 0.1 mmol/kg gadobutrol (Gadovist; Bayer Healthcare Pharmaceuticals, Inc., Whippany, NJ, USA). Axial 3D T1-weighted high resolution, T1-weighted with fat suppression with and without subtraction, and sagittal T2-weighted with fat suppression were obtained. Maximum intensity projection (MIP) reconstruction images and DWI sequence were also acquired. ADC maps were created automatically by using b values of 800 s/mm².

Imaging analysis

The authors reviewed the MRI images according to the American College of Radiology, Breast Imaging Reporting and Data System (ACR BI-RADS) MR Lexicon edition 2013. The MRI was reviewed to define patients with mass or non-mass enhancement. The kinetic curve type (1, 2, or 3), DWI, and ADC were assessed. ADC values were delineated by manual placement of region of interest (ROI) within the breast lesions using the Philips DynaCAD breast analysis system. Then, MRI findings were concluded into ACR-BIRADS categories. All clinical data and pathological diagnoses were blinded to the authors.

Histopathological acquisition

Pathological diagnosis was obtained subsequent to fine needle biopsy (FNA), core needle biopsy (CNB), excisional biopsy, lumpectomy, or mastectomy, based on pathological reports in HIS and considered as the reference standard. All of the breast lesions were classified as benign or malignant groups and subdivided into benign and malignant diseases.

Statistical analysis

Descriptive statistical data were reported as mean, standard deviation (SD), frequency, and percentage. Receiver Operating Characteristic (ROC) curve was plotted and Youden's index was used to identify the optimal cut-off of ADC value. Sensitivity, specificity, accuracy, positive predictive value (PPV), and negative predictive value (NPV) of this ADC value were reported.

The mean ADC values were compared within subgroups of benign and malignant lesions, using one-way analysis of variance and Tukey Post-Hoc Test as a multiple comparison method.

P value < 0.05 was considered to indicate the statistical significance.

All statistical analyses were performed using Jamovi version 2.3.21.0 [13].

Results

Patient demographics

A total of 163 patients with 210 lesions were evaluated. Demographic data of the patients were summarized in Table 1, the mean age of the patients was 51.1 years (range 20-84 years). About 37 (22.7%) patients had a family history of breast cancer.

The clinical indications for breast MRI were abnormal mammography or ultrasound in 53 (32.5%) cases, palpable mass in 86 (52.8%) cases, mastalgia or breast discomfort in 10 (6.1%) cases, nipple discharge in 10 (6.1%) cases, nipple retraction 1 (0.6%) case, and for screening 3 (1.8%) cases.

Table 1. *Demographic data of the patients.*

Patients, n = 163	Total
Age, years	
Mean (SD)	51.1 (12.1)
Range	20-84
Clinical indications, n (%)	
Abnormal mammography or ultrasound	53 (32.5)
Palpable mass	86 (52.8)
Mastalgia or breast discomfort	10 (6.1)
Nipple discharge	10 (6.1)
Nipple retraction	1 (0.6)
Screening	3 (1.8)
Family history, n (%)	
Breast cancer	37 (22.7)
None	105 (64.4)
Not mentioned	21 (12.9)

Lesions characteristics

Characteristics of a total of 210 lesions were demonstrated in Table 2, which included benign and malignant lesions of 84 and 126 lesions, respectively. One hundred sixty-seven lesions (79.5%) were mass lesions, including 99 (59.3%) malignant lesions and 68 (40.7%) benign lesions. The other 43 lesions (20.5%) were non-mass lesions, including 27 (62.8%) malignant lesions and 16 (37.2%) benign lesions.

In DCE-MRI, the dynamic curve features were categorized into 3 types of enhancement (type 1: persistent enhancement, type 2: plateau, type 3: rapid enhancement with washout) and no enhancement. The malignant group was more likely to present as type 3 (82.9%) compared with benign lesions (17.1%), while the benign lesions had type 1 (69.5%) ($P < 0.001$), predominantly. All the non-enhancing lesions were pathologically confirmed as benign.

According to BI-RADS, the majority of BI-RADS 4b, 4c, and 5 categories were pathologically diagnosed as malignancy ($P = 0.003$), about 19 lesions (61.3%), 13 lesions (61.9%) and 66 lesions (72.5%), respectively.

Table 2. *Lesions characteristics.*

Total lesions, n	210	Pathological diagnosis Benign, n (%) 84 (40)	Pathological diagnosis Malignant, n (%) 126 (60)	P-value
Types				
Mass lesions, n (%)	167	68 (40.7)	99 (59.3)	0.675
Non-mass lesions, n (%)	43	16 (37.2)	27 (62.8)	
Contrast uptake phase				
Type 1: Persistent enhancement, n (%)	82	57 (69.5)	25 (30.5)	
Type 2: Plateau, n (%)	49	11 (22.4)	38 (77.6)	< 0.001
Type 3: Rapid enhancement with washout, n (%)	76	13 (17.1)	63 (82.9)	
No enhancement, n (%)	3	3 (100)	0 (0)	
BIRADS				
2, n (%)	11	8 (72.7)	3 (27.3)	
3, n (%)	5	2 (40.0)	3 (60.0)	
4a, n (%)	51	29 (56.9)	22 (43.1)	0.003
4b, n (%)	31	12 (38.7)	19 (61.3)	
4c, n (%)	21	8 (38.1)	13 (61.9)	
5, n (%)	91	25 (27.5)	66 (72.5)	

ADC analysis

The mean ADC value of malignant lesions ($0.913 \times 10^{-3} mm^2/s$) was significantly lower than that of benign lesions ($1.08 \times 10^{-3} mm^2/s$), showing a mean difference of about $0.169 \times 10^{-3} mm^2/s$, $P < 0.001$ (Table 3). Representative images of benign and malignant breast lesions were exhibited in Figure 1 and Figure 2, respectively.

Table 3. *Comparison of the mean ADC values between benign and malignant breast lesions.*

Mean ADC values ($1.08x10^{-3}mm^2/s$)		Means difference (95% CI)	P-value
Benign	Malignant		
1.080	0.913	0.169 (0.27-0.71)	< 0.001

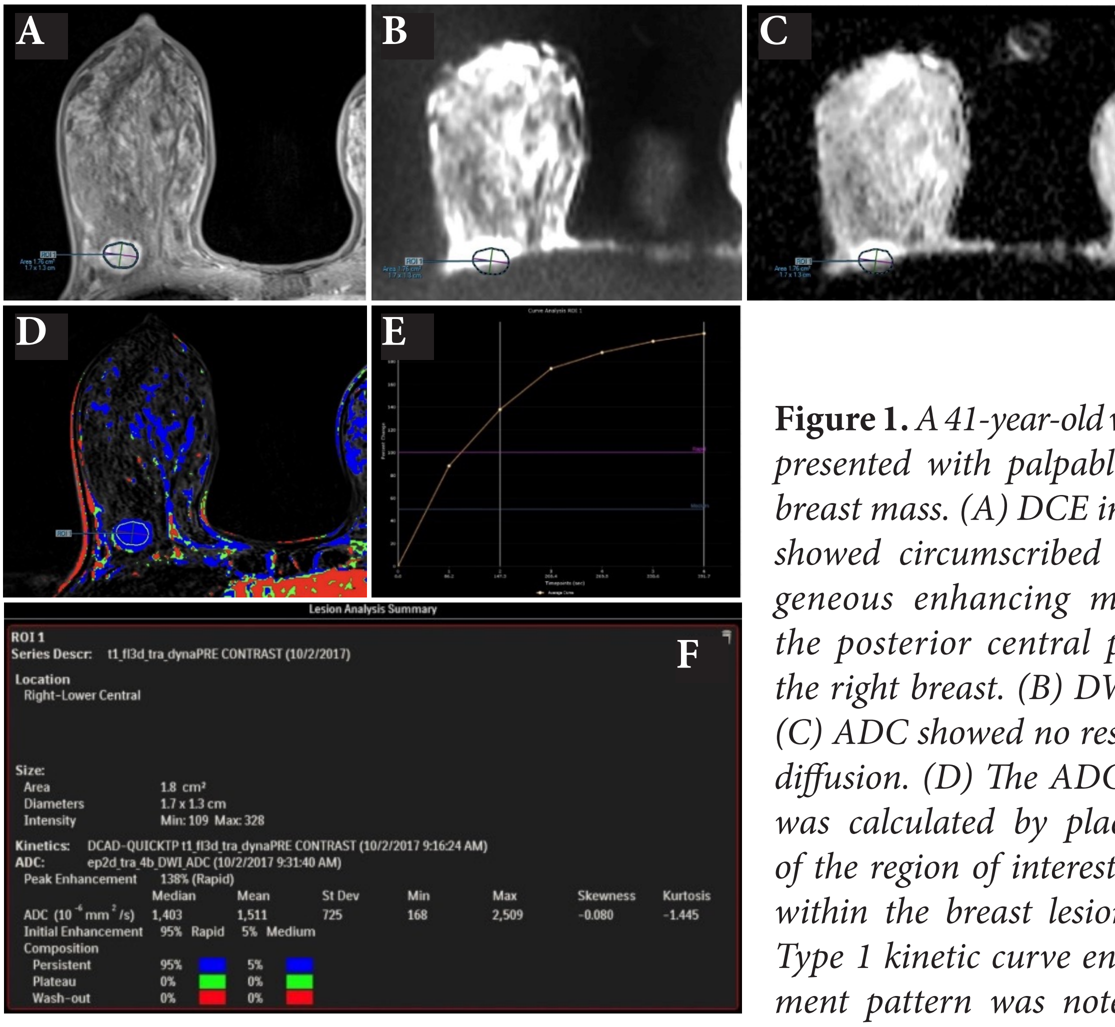

Figure 1. *A 41-year-old woman presented with palpable right breast mass. (A) DCE imaging showed circumscribed homogeneous enhancing mass in the posterior central part of the right breast. (B) DWI and (C) ADC showed no restricted diffusion. (D) The ADC value was calculated by placement of the region of interest (ROI) within the breast lesions. (E) Type 1 kinetic curve enhancement pattern was noted. (F) The mean ADC value of the ROI placed within the lesion was $1.511x10^{-3}$ mm^2/s. The patient underwent lumpectomy and pathology revealed benign dense fibrotic breast tissue.*

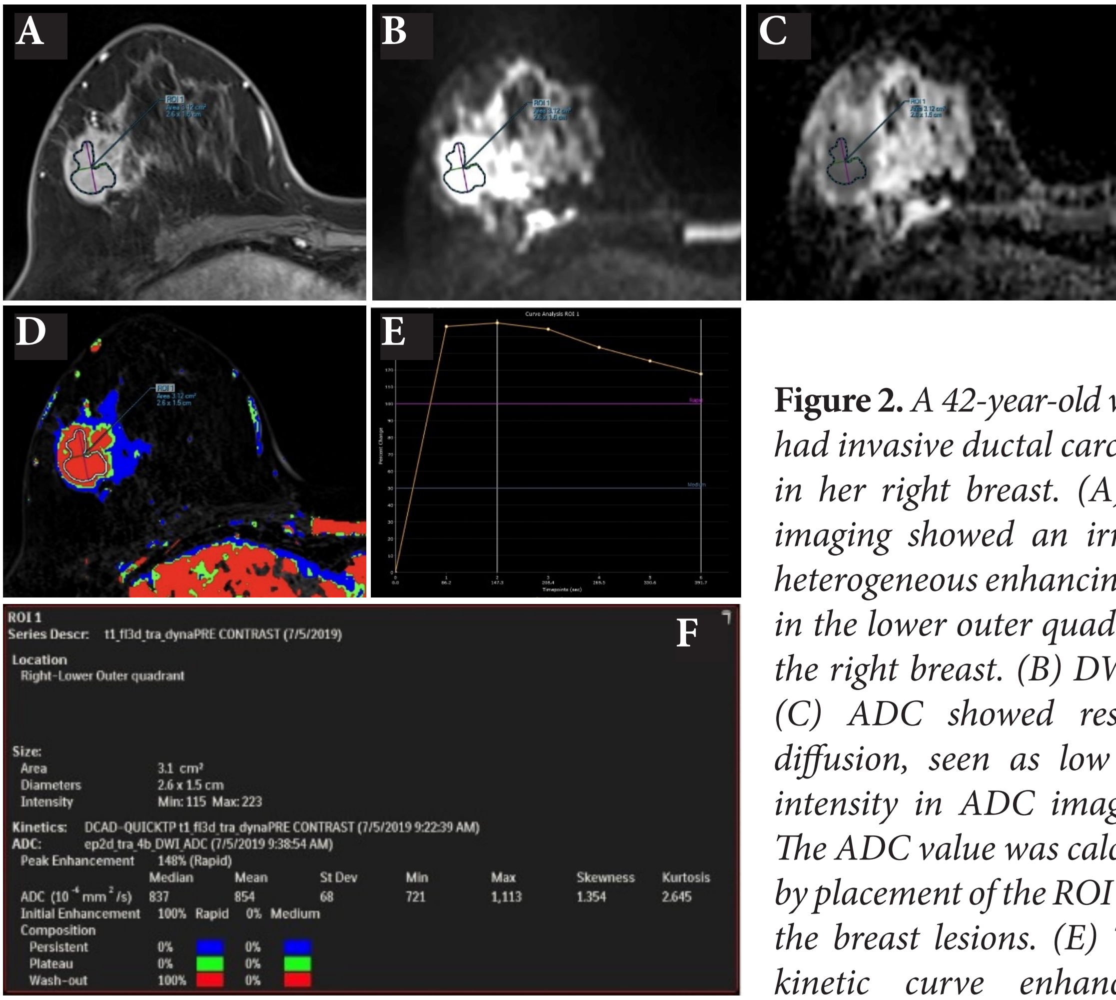

Figure 2. *A 42-year-old woman had invasive ductal carcinoma in her right breast. (A) DCE imaging showed an irregular heterogeneous enhancing mass in the lower outer quadrant of the right breast. (B) DWI and (C) ADC showed restricted diffusion, seen as low signal intensity in ADC image. (D) The ADC value was calculated by placement of the ROI within the breast lesions. (E) Type 3 kinetic curve enhancement pattern was seen. (F) The mean ADC value of the ROI placed within the lesion was 0.854x10^{-3} mm^2/s.*

The box plot of the ADC values of benign and malignant lesions was demonstrated in Figure 3. According to ROC analysis (Figure 4), the AUC was 0.837 and the optimum cut-off ADC value of 0.991x10^{-3} mm^2/s was an excellent predictor for differentiated benign and malignant breast lesions, showing sensitivity (78.6%), specificity (82.5%), accuracy (81%), PPV (85.3%) and NPV (75%) as shown in Table 4.

Table 4. *The optimal ADC value.*

ADC value (mm^2/s)	Sensitivity (95%CI)	Specificity (95%CI)	Accuracy (95%CI)	PPV (95%CI)	NPV (95%CI)
0.991×10^{-3}	78.6% (74.8-88.7)	82.5% (68.3-86.8)	81% (75.0-86.0)	85.3% (79.2-89.8)	75.0% (66.9-81.7)

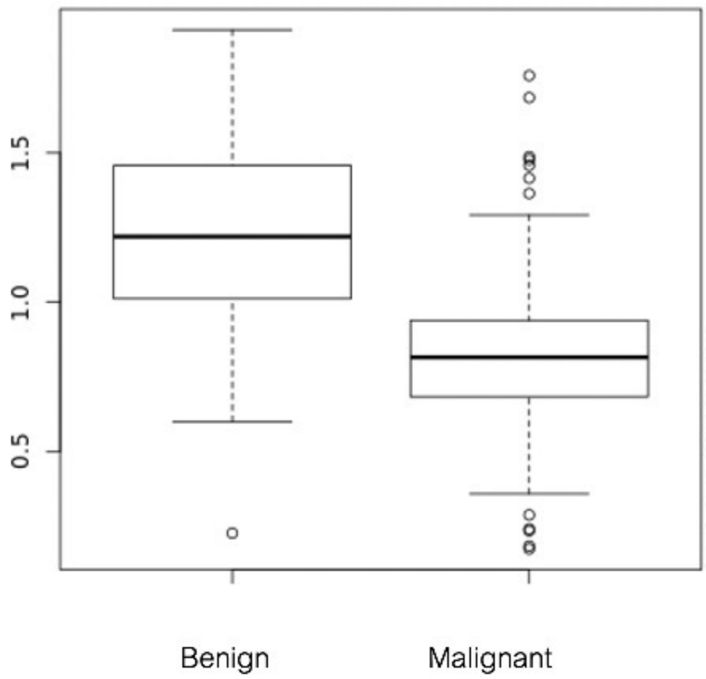

Figure 3. *Box plot of ADC values of benign and malignant breast lesions.*

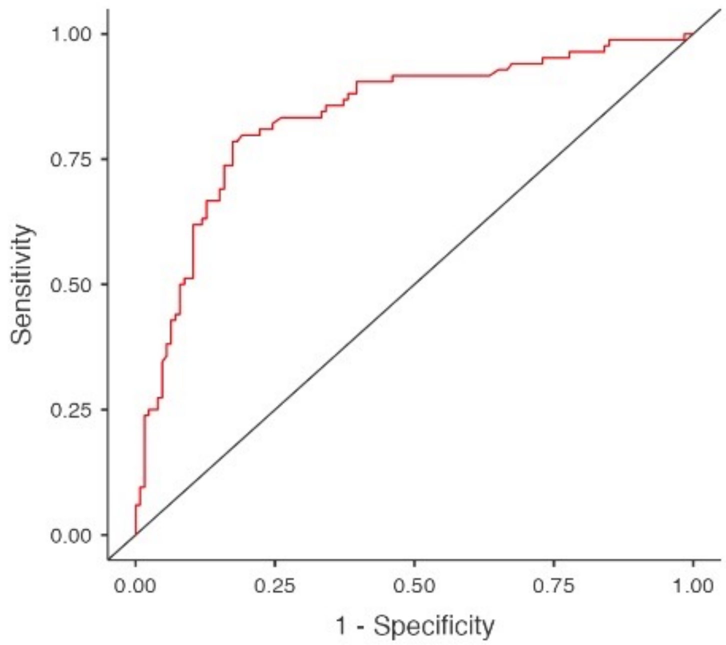

Figure 4. *Graph of ROC Curve demonstrates the diagnostic performance of ADC value of all breast lesions.*

According to the histopathological diagnosis (Table 5), the 126 malignant lesions were divided into 5 subtypes, including ductal carcinoma in situ (DCIS) (n = 21), invasive ductal carcinoma (IDC) (n = 94), invasive lobular carcinoma (ILC) (n = 3), papillary carcinoma (n = 6), and mixed IDC with ILC (n = 2). The 84 benign lesions were categorized into 7 subtypes, including fibroadenoma/fibrocystic change (n = 27), ductal hyperplasia (n = 2), papilloma (n = 19), sclerosing lesion (n = 3), mastitis (n = 2), benign lesions with unspecified pathological diagnosis (n = 16), normal breast tissues (n = 6), and mixed subtypes (n = 9). Mixed subtypes included fibrocystic change with sclerosing adenosis, complex sclerosing with ductal hyperplasia, fibrocystic change with ductal hyperplasia, papilloma with ductal hyperplasia, and fibrocystic change with sclerosing adenosis with ductal hyperplasia. The mean ADC values of all subtypes of the benign and malignant lesions were reported in Table 5, showing the first and second lowest mean ADC values of all lesions were mixed IDC with ILC (0.638 $x10^{-3}$ mm^2/s) and IDC (0.784 $x10^{-3}$ mm^2/s), respectively. As compared with the cut-off ADC value of $0.991x10^{-3}$ mm^2/s, the maximal ADC values of ILC (0.989 $x10^{-3}$ mm^2/s), and mixed IDC with

ILC (0.713 x10^{-3} mm^2/s) were lower than the cut-off ADC value, whereas mastitis was the only benign breast lesion presented as higher minimum ADC value than the cut-off ADC value.

Table 5. *The optimal ADC value.*

ADC value (mm^2/s)	n (%)	Mean ADC (x10^{-3} mm^2/s) (SD)	Minimum ADC (x10^{-3} mm^2/s)	Maximum ADC (x10^{-3} mm^2/s)
Subtypes				
Fibroadenoma/Fibrocystic change/Cyst	27 (32.1)	1.320 (0.26)	0.607	1.790
Ductal hyperplasia	2 (2.4)	1.123 (0.52)	0.754	1.490
Papilloma	19 (22.6)	1.176 (0.30)	0.879	1.710
Benign complex sclerosing/ Sclerosing adenoma	3 (3.6)	1.196 (0.45)	0.701	1.910
Mastitis	2 (2.4)	1.444 (0.07)	1.393	1.500
Benign lesion, unspecified	16 (19)	1.200 (0.37)	0.600	1.890
Normal breast tissue	6 (7.1)	1.367 (0.43)	0.636	1.870
Mixed subtypes	9 (10.7)	0.978 (0.35)	0.226	1.520
Malignant, n = 126	**n (%)**	**Mean ADC (x10^{-3} mm^2/s) (SD)**	**Minimum ADC (x10^{-3} mm^2/s)**	**Maximum ADC (x10^{-3} mm^2/s)**
Subtypes				
DCIS	21 (16.7)	1.004 (0.36)	0.240	1.685
IDC	94 (74.6)	0.784 (0.24)	0.173	1.759
ILC	3 (2.4)	0.840 (0.17)	0.654	0.989
Papillary carcinoma	6 (4.8)	0.879 (0.43)	0.287	1.415
Mixed IDC with ILC	2 (1.6)	0.638 (0.11)	0.563	0.713

Among the mean ADC values of subtypes of malignancy, the mean ADC values of IDC and DCIS showed significant differences (mean difference = 0.220, P Tukey = 0.009), as displayed in Table 6. On the other hand, there was no statistically significant difference between the mean ADC values of subtypes of the benign group.

Table 6. *Post Hoc test shows mean difference of mean ADC values among different subtypes of breast cancers.*

	ILC	DCIS	Papillary carcinoma	Mixed IDC with ILC
IDC				
Mean difference	- 0.0555	- 0.220	- 0.0947	0.146
P-value	0.997	0.009	0.921	0.943
ILC				
Mean difference	-	- 0.165	- 0.0392	0.202
P-value	-	0.862	1.000	0.926
DCIS				
Mean difference	-	-	0.1256	0.366
P-value	-	-	0.855	0.363
Papillary carcinoma				
Mean difference	-	-	-	0.241
P-value	-	-	-	0.812

Discussion

In the present study, BI-RADS 4b, 4c, and 5 categories show more likely to be malignant lesions than other BI-RADS categories. In the detail of lesion characteristics, the pathological diagnosis and kinetic curve features in DCE-MRI are significantly correlated, showing more likely to be malignancy in the type 3 kinetic curve, which has been reported in the previous literature [14]. However, our subgroup analyses of mass and non-mass lesions were found to be insignificant parameters in the differentiation of benign and malignant lesions.

Overall, the malignant group showed a significantly lower mean ADC value than that of the benign group, which agrees with the results of previous studies [15, 16, 17]. Nevertheless, there was still an overlapping of ADC values between these two groups. As shown in our study, the ideal cut-off ADC value of 0.991x $10^{-3}mm^2/s$ is an excellent predictor and improves the diagnostic performance of breast cancer with good specificity (82.5%), accuracy (81%), and PPV (85.3%). In several previous studies, ADC threshold values were still a broad spectrum to differentiate benign and malignant lesions due to several variable factors that could affect the ADC values such as different tesla strength [12]. One study also reported influencing factors, including MRI machine types and different b-values, with significant ADC diagnostic values in Asians [18]. Another study suggested that a b-value of 800 s/mm^2 be obtained as the best cut-off ADC value for the diagnosis of breast cancer [14] which is consistent with our study.

Furthermore, the comparison with our cut-off ADC value may imply that any breast lesion with a higher ADC value could be excluded from ILC, and mixed IDC with ILC. On the other hand, breast lesions with lower ADC values could be excluded from benign lesions such as mastitis. We observed that the ADC value among the malignant subtypes (DCIS, IDC, and papillary carcinoma) can present as high ADC values as compared to this cut-off ADC value which is consistent with the previous report by Gity et al. indicating that the highest ADC values of all benign and malignant lesions were papillary carcinoma and DCIS [19]. While the maximal ADC value of the IDC in their study was not predominantly high, our study investigated a larger number of IDC subtypes than the previous studies. Thus, these lesions should be carefully interpreted and correlated with other MRI sequences.

The current study also demonstrated that mean ADC values of IDC and DCIS were significantly different, consistent with the results reported by the previous study [12, 14]. Several studies have assessed the correlation between subgroups of benign and malignant breast lesions and ADC values, but there were still no previous studies that suggested the efficient ADC threshold for each subtype of benign and malignant lesions.

The limitations of our study include the fact that it has a retrospective design and it was conducted in a single institution with a relatively small sample size. Further prospective studies using the same MRI techniques with a larger number of malignant and benign lesions could increase statistical power.

Finally, the parameters adopted as predictors of breast cancer, including the cut-off ADC value, were unique in each institution due to several influencing factors such as tesla strength and b-value.

Conclusion

DWI was an effective MRI sequence to assess breast cancer by using ADC value as a key parameter. The present study showed that the mean ADC value of malignancy was statistically significantly lower than that of benign lesions. The cut-off ADC value of $0.991 \times 10^{-3} mm^2/s$ had good specificity, accuracy, and PPV to differentiate benign from malignant breast lesions. Moreover, using this cut-off ADC value can exclude some of the subgroups of benign and malignant breast lesions. However, some other breast lesions cannot be diagnosed using ADC alone due to variations in ADC values. To improve diagnostic performance, using ADC values with other important MRI findings is recommended.

Disclosure of Potential Conflicts of Interest

The authors declare that they have no conflict of interest.

References

1. Seely JM, Alhassan T. Screening for breast cancer in 2018— what should we be doing today? Curr Oncol [Internet]. 2018 [cited 2024 Aug 13];25(Suppl 1): 115. Available from: https://www.ncbi.nlm.nih.gov/pmc/articles/PMC6001765/.

2. Akram M, Iqbal M, Daniyal M, Khan AU. Awareness and current knowledge of breast cancer. Biol Res [Internet]. 2017 [cited 2024 Aug 13];50:33. Available from: https://www.ncbi.nlm.nih.gov/pmc/articles/PMC5625777/.

3. Roganovic D, Djilas D, Vujnovic S, Pavic D, Stojanov D. Breast MRI, digital mammography and breast tomosynthesis: comparison of three methods for early detection of breast cancer. Bosn J Basic Med Sci [Internet]. 2015 [cited 2024 Aug 13];15:64-8. Available from: https://www.ncbi.nlm.nih.gov/pmc/articles/PMC4690445/.

4. Gilbert FJ, Pinker-Domenig K. Diagnosis and staging of breast cancer: When and how to use mammography, tomosynthesis, ultrasound, contrast-enhanced mammography, and magnetic resonance imaging. 2019 Feb 20. In: Hodler J, Kubik-Huch RA, von Schulthess GK, editors. diseases of the chest, breast, heart and vessels 2019-2022: diagnostic and interventional imaging [Internet]. Cham (CH): Springer; 2019 [cited 2024 Aug 13]. Chapter 13. Available from: https://www.ncbi.nlm.nih.gov/books/NBK553859/.

5. Guo R, Lu G, Qin B, Fei B. Ultrasound imaging technologies for breast cancer detection and management: a review. Ultrasound Med Biol [Internet]. 2018 [cited 2024 Aug 13];44:37–70. Available from: https://www.ncbi.nlm.nih.gov/pmc/articles/PMC6169997/.

6. Wang Y, Chen H, Li N, Ren J, Zhang K, Dai M, et al. Ultrasound for breast cancer screening in high-risk women: results from a population-based cancer screening program in China. Front Oncol [Internet]. 2019 [cited 2024 Aug 13];9:286. Available from: https://www.ncbi.nlm.nih.gov/pmc/articles/PMC6491776/.

7. Maric J, Boban J, Ivkovic-Kapicl T, Djilas D, Vucaj-Cirilovic V, Bogdanovic-Stojanovic D. Differentiation of breast lesions and distinguishing their histological subtypes using diffusion-weighted imaging and ADC values. Front Oncol [Internet]. 2020 [cited 2024 Aug 13];10:332. Available from: https://www.ncbi.nlm.nih.gov/pmc/articles/PMC7083136/.

8. Ren C, Zou Y, Zhang X, Li K. Diagnostic value of diffusion weighted imaging derived apparent diffusion coefficient and its association with histological prognostic factors in breast cancer. Oncol Lett [Internet]. 2019 [cited 2024 Aug 13];18:3295-303. Available from: https://www.ncbi.nlm.nih.gov/pmc/articles/PMC6704298/.

9. Chen X, He XJ, Jin R, Guo YM, Zhao X, Kang HF, et al. Conspicuity of breast lesions at different b values on diffusion-weighted imaging. BMC Cancer [Internet]. 2012 [cited 2024 Aug 13];12:334. Available from: https://www.ncbi.nlm.nih.gov/pmc/articles/PMC3464932/.

10. Partridge SC, Nissan N, Rahbar H, Kitsch AE, Sigmund EE. Diffusion-weighted breast MRI: clinical applications and emerging techniques. J Magn Reson Imaging [Internet]. 2017 [cited 2024 Aug 13];45:337–55. Available from: https://www.ncbi.nlm.nih.gov/pmc/articles/PMC5222835/.

11. Pereira FP, Martins G, Figueiredo E, Domingues MN, Domingues RC, da Fonseca LM, et al. Assessment of breast lesions with diffusion-weighted MRI: comparing the use of different b values. AJR Am J Roentgenol [Internet]. 2009 [cited 2024 Aug 13];193:1030–5. Available from: https://www.ajronline.org/doi/full/10.2214/AJR.09.2522.

12. Surov A, Meyer HJ, Wienke A. Can apparent diffusion coefficient (ADC) distinguish breast cancer from benign breast findings? A meta-analysis based on 13 847 lesions. BMC Cancer [Internet]. 2019 [cited 2024 Aug 13];19:955. Available from: https://www.ncbi.nlm.nih.gov/pmc/articles/PMC6794799/.

13. The jamovi project : jamovi. Version 2.3 [software]. 2022 [cited 2024 Aug 13]. Available from: https://www.jamovi.org.

14. Shao G, Fan L, Zhang J, Dai G, Xie T. Association of DW/DCE-MRI features with prognostic factors in breast cancer. Int J Biol Markers [Internet] 2017 [cited 2024 Aug 13];32:e118–25. Available from: https://journals.sagepub.com/doi/10.5301/jbm.5000230?url_ver=Z39.88-2003&rfr_id=ori:rid:crossref.org&rfr_dat=cr_pub%20%200pubmed.

15. Bozkurt Bostan T, Koç G, Sezgin G, Altay C, Fazıl Gelal M, Oyar O. Value of apparent diffusion coefficient values in differentiating malignant and benign breast lesions. Balkan Med J [Internet]. 2016 [cited 2024 Aug 13];33:294–300. Available from: https://www.ncbi.nlm.nih.gov/pmc/articles/PMC4898988/.

16. Jiang X, Xie F, Liu L, Peng Y, Cai H, Li L. Discrimination of malignant and benign breast masses using automatic segmentation and features extracted from dynamic contrast enhanced and diffusion weighted MRI. Oncol Lett [Internet]. 2018 [cited 2024 Aug 13]; 16:1521-8. Available from: https://www.spandidos-publications.com/10.3892/ol.2018.8805?text=fulltext.

17. Horvat JV, Durando M, Milans S, Patil S, Massler J, Gibbons G, et al. Apparent diffusion coefficient mapping using diffusion-weighted MRI: impact of background parenchymal enhancement, amount of fibroglandular tissue and menopausal status on breast cancer diagnosis. Eur Radiol [Internet]. 2018 [cited 2024 Aug 13];28:2516–24. Available from: https://europepmc.org/article/MED/29330631.

18. Qu RF, Guo DR, Chang ZX, Meng J, Sun Y, Hao SH, et al. Differential diagnosis of benign and malignant breast tumors using apparent diffusion coefficient value measured through diffusion-weighted magnetic resonance imaging. J Comput Assist Tomogr [Internet]. 2015 [cited 2024 Aug 13];39:513–22. Available from: https://journals.lww.com/jcat/abstract/2015/07000/differential_diagnosis_of_benign_and_malignant.11.aspx. Subscription required.

19. Gity M, Moradi B, Arami R, Arabkheradmand A, Kazemi MA. Two different methods of region-of-interest placement for differentiation of benign and malignant breast lesions by apparent diffusion coefficient value. Asian Pac J Cancer Prev [Internet].2018 [cited 2024 Aug 13];19:2765–70. Available from: https://www.ncbi.nlm.nih.gov/pmc/articles/PMC6291064/.

THE ASEAN JOURNAL OF RADIOLOGY
ISSN 2672-9393

Original Article

Sonographic findings of recurrent disease at the thyroid bed in differentiated thyroid cancer

Pinyaporn On-Ekkasit, M.D.
Sorasich Subhadhirasakul, M.D.
Jalat Busaman, M.D.
Songklod Pakdeejit, M.D.
From Department of radiology, Hatyai Hospital, Songkhla, Thailand.
Address correspondence to P.O. (email: pinyaporn.one@gmail.com)

Received 25 March 2024; revised 3 September 2024; accepted 5 December 2024
doi:10.46475/asean-jr.v25i3.902

Abstract

Background: Neck ultrasonography (US) is an important tool for the surveillance of patients with differentiated thyroid cancer (DTC) after initial treatment.

Objective: To evaluate sonographic findings associated with recurrent disease at the thyroid bed in patients with DTC.

Materials and Methods: This was a retrospective cohort study. We reviewed the data of 26 patients with DTC who underwent thyroidectomy and had thyroid bed lesions detected by neck US between January 2013 and December 2023. Sonographic findings of recurrent and non-recurrent lesions were compared.

Results: A total of 26 thyroid bed lesions in 26 patients were identified, including 17 recurrent and nine non-recurrent lesions. The median size was 1.0 centimeter. Sonographic findings of recurrent versus non-recurrent lesions were hypoechoic in 58.8% versus 55.6%, wider-than-tall in 64.7% versus 100%, smooth margin in 82.4% versus 66.7%, and no calcification in 70.6% versus 88.9%. There was no significant difference in each sonographic finding and combination of sonographic findings between recurrent and non-recurrent lesions. All 13 available laboratory patients with recurrent lesions had elevated serum Tg and/or TgAb levels.

Conclusion: The sonographic findings alone could not be used to distinguish recurrent lesions from the non-recurrent ones at the thyroid bed in patients with DTC. Clinical and laboratory results should be correlated to determine the need for further investigations.

Keywords: Recurrent disease, Sonographic findings, Thyroid bed, Thyroid cancer.

Introduction

Differentiated thyroid cancer (DTC) comprises more than 90% of all thyroid cancers [1, 2]. The overall prognosis is good with a 10-year overall survival rate for middle-aged adults (about 80-95%) [3, 4]. The initial treatment of DTC includes surgery, postoperative radioiodine treatment (RAI) if indicated, and thyroid stimulating hormone (TSH) suppression. A major goal of long-term follow-ups for DTC is accurate surveillance for possible disease recurrence in patients with the disease-free status. Follow-up tools for DTC are serum thyroglobulin (Tg) measurement, neck ultrasonography (US), and other imaging techniques as needed [1, 2, 5, 6].

Neck recurrence is found in up to 20% of patients with DTC [3, 7, 8]. Although serum Tg monitoring plays an excellent role in raising suspicion of recurrent disease, it lacks specificity in the presence of remaining thyroid gland tissue and may have falsely low values in the presence of Tg antibodies (TgAb) [1, 5, 6, 9]. Neck US is an important and highly sensitive tool for evaluating neck recurrence [5, 6, 8, 10]. It provides anatomical details of the neck and has the ability to detect small-volume tumors [9]. The 2015 American Thyroid Association (ATA) guidelines recommended that neck US should be performed at 6-12 months after surgery and then periodically, depending on the patient's risk of recurrence and serum Tg level [1].

Thyroid bed lesions detected by neck US can be benign conditions such as a benign thyroid tissue remnant, postoperative fibrosis, suture granuloma, or a reactive lymph node; however, some of these lesions are malignancies [11-14]. There was conflicting data in the literature regarding sonographic findings associated with thyroid bed recurrence. Several studies proposed different sonographic findings of thyroid bed recurrence, including hypoechogenicity [11, 14-16], taller-than-wide [12, 13, 15, 17], irregular margin [12, 13, 15-17], microcalcification [12, 13, 15, 18], and increased vascularization [14, 15]. However, one study reported no statistical differences in sonographic findings between recurrent and non-recurrent lesions at the thyroid bed [11]. Thus, we aimed to identify sonographic findings associated with recurrent disease at the thyroid bed in patients with DTC.

Materials and methods

Study design

This was a retrospective cohort study conducted at a tertiary care center. The study protocol was approved by the institutional review board of our hospital.

Patients

We used the ultrasonographic reporting database from our institution to identify patients with DTC aged 18 years and older who underwent thyroidectomy and had thyroid bed lesions between January 2013 and December 2023. Medical records and sonographic images of eligible patients were retrospectively reviewed. Patient data including sex, age, type of surgical procedure, type of DTC, history of RAI treatment, serum Tg and TgAb levels within 1 year from the time of neck US, and sonographic findings of thyroid bed lesions were recorded. Thyroid bed lesions were categorized into recurrent and non-recurrent lesions. Patients were considered to have recurrent lesions if surgical pathology or fine needle aspiration (FNA) cytology (if absent surgical pathology) were malignancy. The criteria for non-recurrent lesions were: (1) Surgical pathology or FNA cytology (if absent surgical pathology) was benign, or (2) In case of absent surgical pathology and FNA cytology, patients were considered to have non-recurrent lesions if iodine-131 total body scan (I-131 TBS) showed no abnormal uptake, low serum Tg levels

(< 1 ng/mL with TSH-stimulation [1]), and negative serum TgAb levels. We excluded thyroid bed lesions that were inconclusive to categorize into groups.

Neck ultrasonography

Neck US was performed with Toshiba Aplio 500 or Canon Aplio a550 using a 14-Megahertz linear transducer. Sonographic images of each thyroid bed lesion were reviewed independently for size, composition, echogenicity, shape, margin, and echogenic foci by two radiologists blinded to the diagnosis. In case of disagreement, the final result was decided by consensus.

The size of thyroid bed lesions was recorded in the longest diameter. Echogenicity was characterized relative to thyroid tissue, except for very hypoechoic in which the strap muscles were used for comparison. A taller-than-wide shape was evaluated in the transverse plane. An irregular margin was referred to as a spiculated edge. Microcalcifications were defined as punctate echogenic foci without acoustic shadowing equal to or less than 1 millimeter (mm) in diameter. Macrocalcifications were defined as coarse echogenic foci with acoustic shadowing larger than 1 mm. Peripheral calcifications were defined as calcifications that lie along all or part of the margin [19, 20].

Statistical analysis

The data analysis was performed using the Statistical Package for Social Sciences software version 21. Continuous data were presented as the median and interquartile range (IQR) or the mean and standard deviation. Categorical data were presented as numbers and percentages. We compared the size of thyroid bed lesions between the two groups using the Mann-Whitney U test. We compared other sonographic findings between the two groups using the Fisher exact test. A p-value < 0.05 was considered statistically significant.

Results

Of 26 patients with DTC, there were 23 with papillary thyroid cancer (88.5%), two with follicular thyroid cancer (7.7%), and one with poorly differentiated thyroid cancer (3.8%). Twenty-four patients were females (92.3%) and two were males (7.7%) with a mean age of 47 ± 15.7 years. Twenty-four patients underwent total thyroidectomy (92.3%) and the remaining two patients underwent left and right lobectomy. Postoperative RAI was performed in 23 patients (88.5%).

Serum Tg and/or TgAb levels were available in 22 out of 26 patients. All 13 patients with recurrent lesions had elevated serum Tg (> 0.2 ng/mL without TSH-stimulation or > 1 ng/mL with TSH-stimulation [1]) and/or TgAb levels. Among nine patients with non-recurrent lesions, three had elevated serum Tg and/or TgAb levels.

A total of 26 thyroid bed lesions were identified, including 17 recurrent and nine non-recurrent lesions. The median size was 1.0 centimeter (cm) with an IQR of 0.7 to 1.4 cm. Seventeen recurrent lesions were diagnosed by surgical pathology (n=8) and FNA cytology (n=9). Nine non-recurrent lesions were diagnosed by surgical pathology (n=1), FNA cytology (n=3), and I-131 TBS with serum Tg and TgAb levels (n=5).

Sonographic findings of recurrent and non-recurrent lesions at the thyroid bed were demonstrated in Table 1. Sonographic findings of recurrent lesions were solid or completely solid in 100%, hypoechoic in 58.8% (Figure 1), wider-than-tall in 64.7%, a smooth margin in 82.4%, and no calcification in 70.6%. Microcalcifications were seen in 11.8%. The median size of recurrent lesions was 1.1 cm with an IQR of 1.0 to 1.5 cm. Sonographic findings of non-recurrent lesions were solid or completely solid in 100%, hypoechoic in 55.6% (Figure 2), wider-than-tall in 100%, smooth margin in 66.7%, and no calcification in 88.9%. The median size of non-recurrent lesions was 0.6 cm with an IQR of 0.5 to 1.2 cm. There was no significant difference in each sonographic finding and combination of sonographic findings between recurrent and non-recurrent lesions (Table 1-2).

Table 1. *Sonographic findings of recurrent and non-recurrent lesions at the thyroid bed.*

Sonographic findings	Recurrent lesions (n=17) number (%)	Non-recurrent lesions (n=9) number (%)	p-value
Size (cm), median (IQR)	1.1 (1.0 - 1.5)	0.6 (0.5 - 1.2)	0.65
Composition			
Solid or almost completely solid	17 (100)	9 (100)	N/A
Echogenicity			
Anechoic	0 (0)	0 (0)	0.095
Hyperechoic	1 (5.9)	3 (33.3)	
Isoechoic	1 (5.9)	1 (11.1)	
Hypoechoic	10 (58.8)	5 (55.6)	
Very hypoechoic	5 (29.4)	0 (0)	
Shape			
Wider-than-tall	11 (64.7)	9 (100)	0.063
Taller-than-wide	6 (35.3)	0 (0)	
Margin			
Smooth	14 (82.4)	6 (66.7)	0.535
Ill-defined	1 (5.9)	2 (22.2)	
Irregular	2 (11.8)	1 (11.1)	
Echogenic foci			
None	12 (70.6)	8 (88.9)	0.851
Macrocalcifications	2 (11.8)	1 (11.1)	
Peripheral calcifications	1 (5.9)	0 (0)	
Microcalcifications	2 (11.8)	0 (0)	

cm = centimeter, IQR = interquartile range, N/A = not applicable

Table 2. *Combination of sonographic findings of recurrent and non-recurrent lesions at the thyroid bed.*

Sonographic findings	Recurrent lesions (n=17) number (%)	Non-recurrent lesions (n=9) number (%)	p-value
Hypoechoic + Taller-than-wide	6 (35.3)	0 (0)	0.063
Hypoechoic + Irregular margin	2 (11.8)	1 (11.1)	1.000
Hypoechoic + Microcalcifications	2 (11.8)	0 (0)	0.529
Taller-than-wide + Irregular margin	1 (5.9)	0 (0)	1.000
Taller-than-wide + Microcalcifications	2 (11.8)	0 (0)	0.529
Irregular margin + Microcalcifications	0 (0)	0 (0)	N/A
Hypoechoic + Taller-than-wide + Irregular margin	1 (5.9)	0 (0)	1.000
Hypoechoic + Taller-than-wide + Microcalcifications	2 (11.8)	0 (0)	0.529
Taller-than-wide + Irregular + Microcalcifications	0 (0)	0 (0)	N/A

N/A = not applicable

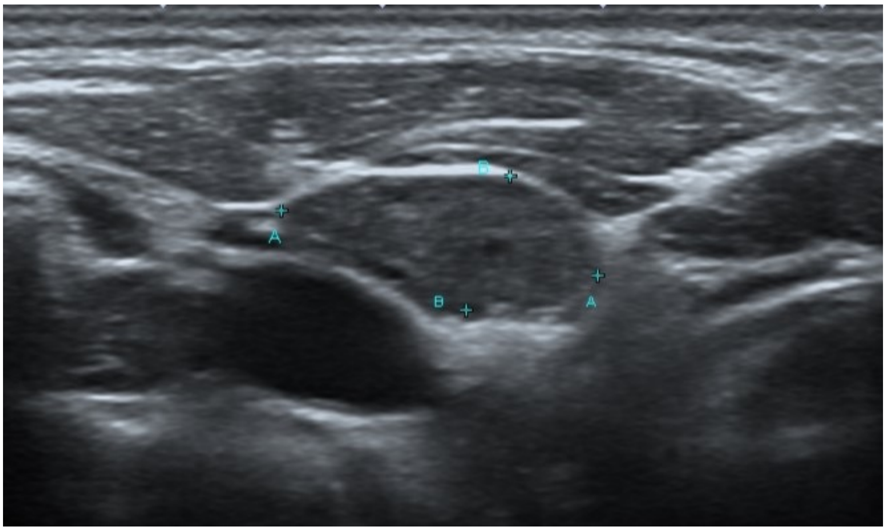

Figure 1. *Recurrent lesion at the thyroid bed in a 60-year-old woman; a transverse sonographic image showed a 1.5-cm almost solid hypoechoic wider-than-tall nodule with a smooth margin. Surgical excision revealed metastatic papillary carcinoma of a cervical lymph node.*

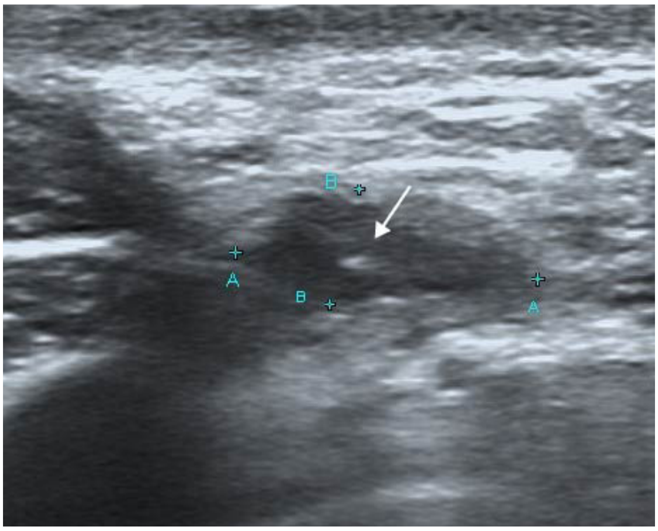

Figure 2. *Non-recurrent lesion at the thyroid bed in a 53-year-old woman; a transverse sonographic image showed a 1.0-cm solid hypoechoic wider-than-tall nodule with an irregular margin and macrocalcification (arrow). FNA cytology revealed granulomatous inflammation.*

Discussion

In our study, most recurrent lesions were solid or completely solid (100%), hypoechoic (58.8%), wider-than-tall (64.7%), smooth margin (82.4%), and no calcification (70.6%). The minority of these lesions had taller-than-wide (35.3%), irregular margins (11.8%), and microcalcifications (11.8%). However, we found no significant difference in each sonographic finding and combination of sonographic findings between recurrent and non-recurrent lesions. The reason for these results may be due to the small size of the lesions (median size of 1.0 cm), which made it hard to characterize the sonographic findings. Our findings suggested that sonographic findings alone could not be used as a means to distinguish recurrent disease from benign conditions at the thyroid bed. Similar to our study, the study by Shin et al. showed that most recurrent lesions were hypoechoic (70%). Taller-than-wide and microcalcifications were seen in only 5% and 10% of recurrent lesions, respectively. They also reported no statistical differences in sonographic findings between recurrent and non-recurrent lesions at the thyroid bed [11]. On the contrary, several studies proposed different sonographic findings of thyroid bed recurrence, including hypoechogenicity [11, 14-16], taller-than-wide [12, 13, 15, 17], irregular margin [12, 13, 15-17], microcalcification [12, 13, 15, 18], and increased vascularization [14, 15].

Of 22 available laboratory patients, all 13 patients with recurrent lesions had elevated serum Tg and/or TgAb levels. Among nine patients with non-recurrent lesions, three had elevated serum Tg and/or TgAb levels. The measurement of serum Tg is an important modality to monitor patients for recurrent disease. However, it lacks specificity in the presence of remaining thyroid gland tissue. Serum TgAb should be measured together with serum Tg because the presence of TgAb may falsely lower the serum Tg level. A rising serum Tg or TgAb level suggests recurrent disease [1, 5, 6, 9]. Therefore, elevated serum Tg or TgAb level should lead to further investigations such as neck US, diagnostic I-131 TBS, computed tomography (CT), magnetic resonance imaging, or fluorine-18 fluorodeoxyglucose positron emission tomography/ CT [1, 2, 5, 6].

Neck US is an important and highly sensitive tool for evaluating neck recurrence [5, 6, 8, 10]. According to the 2015 ATA guidelines, neck US should be performed at 6-12 months after surgery and then periodically, depending on the patient's risk of recurrence and the serum Tg level. In addition, the management of thyroid bed lesions without any other suspicious sonographic findings such as suspicious cervical lymph nodes, including low serum Tg level, may be followed up with neck US. FNA should be performed in cervical lymph nodes ≥ 0.8–1.0 cm in the smallest diameter with a cystic appearance, hyperechoic punctuations, or peripheral vascularization [1]. Our findings supported this recommendation. However, if clinical or laboratory findings suspect recurrent disease, further investigations such as FNA or diagnostic I-131 TBS should be considered to confirm the diagnosis.

The strengths of our study were a cohort design and the blinding of two radiologists who reviewed sonographic images. However, there were some limitations. First, our study had a small population, which may not be sufficient to detect a difference between the two groups. Second, many thyroid bed lesions without suspicious sonographic findings with low serum Tg levels were followed up with neck US. Therefore, those lesions were not included in our study resulting in a small number of non-recurrent lesions. Third, data on vascular flow signals within the lesions were not available. One study found that increased vascularity was associated with thyroid bed recurrence. However, another study reported that vascular flow signals were not related to thyroid bed recurrence. Fourth, all thyroid bed lesions had a solid or almost completely solid composition. Thus, we cannot compare the compositions between the two groups.

Conclusion

The sonographic findings alone could not be used to distinguish the recurrent from non-recurrent lesions at the thyroid bed in patients with DTC. If clinical or laboratory findings suspect recurrent disease, further investigations such as FNA or diagnostic I-131 TBS should be considered to confirm the diagnosis.

Acknowledgments

The authors would like express sincere gratitude to the clinical research center for advice on this research study.

Conflicts of Interest and Source of Funding: None to declare.

References

1. Haugen BR, Alexander EK, Bible KC, Doherty GM, Mandel SJ, Nikiforov YE, et al. 2015 American Thyroid Association management guidelines for adult patients with thyroid nodules and differentiated thyroid cancer: the American Thyroid Association guidelines task force on thyroid nodules and differentiated thyroid cancer. Thyroid 2016;26:1-133. doi: 10.1089/thy.2015.0020.

2. Cabanillas ME, McFadden DG, Durante C. Thyroid cancer. Lancet 2016; 388:2783–95. doi: 10.1016/S0140-6736(16)30172-6.

3. Schlumberger MJ. Papillary and follicular thyroid carcinoma. N Engl J Med 1998;338:297-306. doi: 10.1056/NEJM199801293380506.

4. Mettler FA, Guiberteau MJ. Essentials of nuclear medicine and molecular imaging. 7th ed. Philadelphia: Elsevier; 2019.

5. Santhanam P, Ladenson PW. Surveillance for differentiated thyroid cancer recurrence. Endocrinol Metab Clin North Am 2019;48:239–52. doi: 10.1016/j.ecl.2018.11.008.

6. Schlumberger M, Leboulleux S. Current practice in patients with differentiated thyroid cancer. Nat Rev Endocrinol 2021;17:176–88. doi: 10.1038/s41574-020-00448-z.

7. Mazzaferri EL. An overview of the management of papillary and follicular thyroid carcinoma. Thyroid 1999;9:421-7. doi: 10.1089/thy.1999.9.421.

8. Frasoldati A, Pesenti M, Gallo M, Caroggio A, Salvo D, Valcavi R. Diagnosis of neck recurrences in patients with differentiated thyroid carcinoma. Cancer 2003;97:90–6. doi: 10.1002/cncr.11031.

9. Johnson NA, Tublin ME. Postoperative surveillance of differentiated thyroid carcinoma: rationale, techniques, and controversies. Radiology 2008;249:429-44. doi: 10.1148/radiol.2492071313.

10. Rondeau G, Fish S, Hann LE, Fagin JA, Tuttle RM. Ultrasonographically detected small thyroid bed nodules identified after total thyroidectomy for differentiated thyroid cancer seldom show clinically significant structural progression. Thyroid 2011;21:845–53. doi: 10.1089/thy.2011.0011.

11. Shin JH, Han BK, Ko EY, Kang SS. Sonographic findings in the surgical bed after thyroidectomy: comparison of recurrent tumors and nonrecurrent lesions. J Ultrasound Med 2007;26:1359–66. doi: 10.7863/jum.2007.26.10.1359.

12. Lee JH, Lee HK, Lee DH, Choi CG, Gong G, Shong YK, et al. Ultrasonographic findings of a newly detected nodule on the thyroid bed in postoperative patients for thyroid carcinoma: correlation with the results of ultrasonography-guided fine-needle aspiration biopsy. Clin Imaging 2007;31:109-13. doi: 10.1016/j.clinimag.2006.11.001.

13. Ko MS, Lee JH, Shong YK, Gong GY, Baek JH. Normal and abnormal sonographic findings at the thyroidectomy sites in postoperative patients with thyroid malignancy. AJR Am J Roentgenol 2010;194:1596–609. doi: 10.2214/AJR.09.2513.

14. Kamaya A, Gross M, Akatsu H, Jeffrey RB. Recurrence in the thyroidectomy bed: sonographic findings. AJR Am J Roentgenol 2011;196:66–70. doi: 10.2214/AJR.10.4474.

15. Leenhardt L, Erdogan MF, Hegedus L, Mandel SJ, Paschke R, Rago T, et al. 2013 European Thyroid Association guidelines for cervical ultrasound scan and ultrasound-guided techniques in the postoperative management of patients with thyroid cancer. Eur Thyroid J 2013;2:147–59. doi: 10.1159/000354537.

16. Choudhary C, Wartofsky L, Tefera E, Burman KD. Evaluation of thyroid bed nodules on ultrasonography after total thyroidectomy: risk for loco-regional recurrence of thyroid cancer. Eur Thyroid J 2015;4:106–14. doi: 10.1159/000431317.

17. Hahn SY, Shin JH, Han BK, Ko EY, Kang SS, Chung JH, et al. Predictive factors related to the recurrence at US-guided fine needle aspiration in postoperative patients with differentiated thyroid cancer. Clin Endocrinol (Oxf) 2011;74:270-5. doi: 10.1111/j.1365-2265.2010.03915.x.

18. Frates MC, Parziale MP, Alexander EK, Barletta JA, Benson CB. Role of sonographic characteristics of thyroid bed lesions identified following thyroidectomy in the diagnosis or exclusion of recurrent cancer. Radiology 2021;299:374-80. doi: 10.1148/radiol.2021201596.

19. Kwak JY, Han KH, Yoon JH, Moon HJ, Son EJ, Park SH, et al. Thyroid imaging reporting and data system for US features of nodules: a step in establishing better stratification of cancer risk. Radiology 2011;260:892-9. doi: 10.1148/radiol.11110206.

20. Tessler FN, Middleton WD, Grant EG, Hoang JK, Berland LL, Teefey SA, et al. ACR Thyroid Imaging, Reporting and Data System (TI-RADS): white paper of the ACR TI-RADS committee. J Am Coll Radiol 2017;14:587-95. doi: 10.1016/j.jacr.2017.01.046.

THE ASEAN JOURNAL OF RADIOLOGY
ISSN 2672-9393

Original Article

CT clot characteristics and success of endovascular thrombectomy in acute anterior circulation ischemic stroke

Naphon Assawagumtorn, M.D.
Krittanon Lertutsahakul, M.D.
Ketsuda Jakchairoongruang, M.D.
From Department of Radiology, Faculty of Medicine, Chulalongkorn University, King Chulalongkorn Memorial Hospital, The Thai Red Cross Society, Bangkok, Thailand.
Address correspondence to K.J. (email: ketsuda.ja@chula.ac.th)

Received 20 April 2023; revised 30 August 2024; accepted 22 November 2024
doi:10.46475/asean-jr.v25i3.718

Abstract

Background: CT and CT angiography (CTA) have been informative for acute occlusive thrombus. Conflicting results of the thrombus characteristics and endovascular thrombectomy (EVT) revascularization outcome have been debated.

Objective: We aimed to evaluate CT clot characteristics and EVT outcomes in acute ischemic stroke patients.

Materials and Methods: Unenhanced CT and multiphase CTA brain of 59 acute anterior-circulation ischemic stroke patients undergoing EVT from November 2019 to June 2021 were reviewed. The following clot characteristics were assessed: the most proximal clot location, clot length, clot burden score (CBS), distance from the terminal ICA to the most proximal part of the clot (DT), clot heterogeneity, mean clot attenuation, relative mean clot attenuation to contralateral artery, and clot perviousness. The standard deviation (SD) of the measured clot attenuation represented clot heterogeneity. At least mTICI 2b on post-thrombectomy cerebral angiography was considered successful revascularization. Descriptive and analytic statistical analyses were obtained with $p<0.05$ considered significant.

Results: Fifty two of 59 cases (88.1%) had successful thrombectomy. DT was significantly shorter in the successful group (8.5±9.1 mm) versus the unsuccessful group (16.4±13.2 mm) with p=0.046; however, association between DT and revascularization outcomes did not reach statistical significance (OR=0.94; 95%CI=0.87-1.00; p=0.061). Clot heterogeneity and other characteristics showed no differences between two groups or associations with outcomes.

Conclusion: Among the clot features on unenhanced CT and multi-phase CTA brain in our study group, distance of the clot from terminal ICA (DT) was significantly shorter in the successful EVT group. Further assessment of clot characteristics and EVT outcome in larger numbers of cases should be sought for a potential predictor of success.

Keywords: Acute ischemic stroke, Clot characteristics, Endovascular thrombectomy.

Introduction

Acute ischemic stroke is one of the leading causes of the disabilities across the world. An endovascular treatment has become more recognized and well-established for its benefits in this decade and included in the standard treatment of patients [1]. Identification of imaging biomarkers that predict the endovascular treatment outcome would be beneficial in acute stroke management. Thrombus characteristics on CT and CT angiography (CTA) have been studied for their association with the outcome of acute ischemic stroke, but there are conflicting results [2-7]. Using multi-phase CTA proves more advantageous than over single-phase CTA in evaluation of large vessel occlusion and collateral assessment in acute ischemic stroke. It improves the vessel occlusion detection rate, yearning higher interrater reliability, improves the measurement of clot length, and also assesses clot perviousness [8, 9]. This study aimed to assess whether the clot characteristics on unenhanced CT and multi-phase CTA brain are associated with the mechanical thrombectomy outcome in patients with acute anterior circulation ischemic stroke.

Materials and methods

Patients

This retrospective study was approved by the Institutional Review Board, and the requirement for informed consent was waived. We included all acute anterior circulation ischemic stroke patients who underwent endovascular thrombectomy at King Chulalongkorn Memorial Hospital from November 2019 to June 2021. The exclusion criteria were the following: 1) less than 18 years of age; 2) clot location occupying the petrous to clinoid segment of the internal carotid artery (ICA); 3) clot with an adjacent calcified plaque; 4) spontaneous resolution or failed endovascular thrombectomy due to markedly tortuous vessels; 5) an undetermined proximal or distal end of the clot; and 6) poor image quality.

Imaging protocol

All patients underwent a CT scan using the 256-slice CT scanner, Revolution™ CT (GE Healthcare, USA) with the following parameters: tube voltage 120 kV, automatically adjusted tube current ranging from 350-600 mA and rotation time of 0.5 second.

All acute ischemic stroke patients were continuously investigated following hospital protocols, including CT brain and multiphase CT angiography (CTA) of the brain and neck, before endovascular thrombectomy. The non-contrast CT brain covered the entire brain and was reconstructed in 1.25-mm thickness in the axial plane and multiplanar reconstruction in 5-mm thickness. Bolus contrast media injection was done using 65 mL of iohexol (350 mgI/mL). The CTA of brain and neck was done using the bolus tracking technique with 8-second intervals in 3 phases: arterial, first delayed, and second delayed. The arterial and second delayed phases covered from the vertex to the aortic arch, and the first delayed phase covered the entire brain. The CTA brain study was reconstructed in an 8-mm maximal intensity projection (MIP) image in axial view for all three phases and with additional sagittal and coronal views for the arterial phase.

Data collection and analysis

The demographic data of the patients were reviewed from the electronic medical records and included the following information: age, sex, underlying disease, the presence of the anti-platelet and the anti-coagulation treatment, the intravenous thrombolytic treatment, The National Institutes of Health Stroke Scale (NIHSS), stroke etiology according to TOAST classification, the hematocrit level, and time of onset or time of last seen normal in the case of an unclear onset. The patients with incomplete evaluation of stroke etiology were counted as strokes with undetermined sources.

The clot characteristics on CT and CTA studies were independently assessed by a radiologist with one year of experience in neuroradiology and a neuroradiologist with eight years of experiences. The two radiologists went through image analyses for five random cases altogether per the following protocols (Figure 1).

Location and length: The location and length were primarily considered on the source image and the MIP image of the multi-phase CTA study, respectively. The most proximal part of the clot was collected as the location of the clot. In unclear circumstances, non-contrast CT and cerebral angiography studies were used to aid in determining the location. A consensus was reached in the selection of the clot location for further analysis in case of dissimilar results. Multi-planar reconstruction in the plane parallel to the arterial course was done to measure the clot length. For clots extending into more than one arterial branch, the longest length in one branch was determined as the clot length.

Clot burden score (CBS): The CBS is a scoring system used to define the extension of an anterior-circulation clot, scaling from 0 to 10 [6]. A score of 2 was subtracted if thrombus was found in each of the supraclinoid ICAs, the proximal, and the distal half of the M1 segment of the MCA. A score of 1 was subtracted if thrombus was found in each of the infraclinoid ICA, ACA, and each M2 branch.

Attenuation and heterogeneity: Three regions of interest (ROIs), each with an area of about 2 mm^2, were placed within the proximal, middle, and distal portions of the clot on an axial 1.25-mm-thickness non-contrast CT study. The average attenuation and standard deviation of these three ROIs were considered the absolute attenuation and the clot heterogeneity, respectively. The other three ROIs were placed within the contralateral artery, symmetrically. The ratio of the average attenuation of the clot to average attenuation of the contralateral artery was the relative attenuation. In the case of a short clot, one or two ROIs were considered appropriate.

Perviousness: Three ROIs were placed within the clots on the source image of the three phases of the CTA study with the same location of ROIs placed on non-contrast CT. Clot perviousness was considered the maximal average attenuation of the clot among the three phases of CTA subtracted by the absolute attenuation of the clot.

Distance from terminal ICA (DT): This distance was considered on MIP images of the CTA study, measuring from the terminal ICA to the most proximal part of the clot. If the clot location was proximal to the terminal ICA, the distance was considered 0.

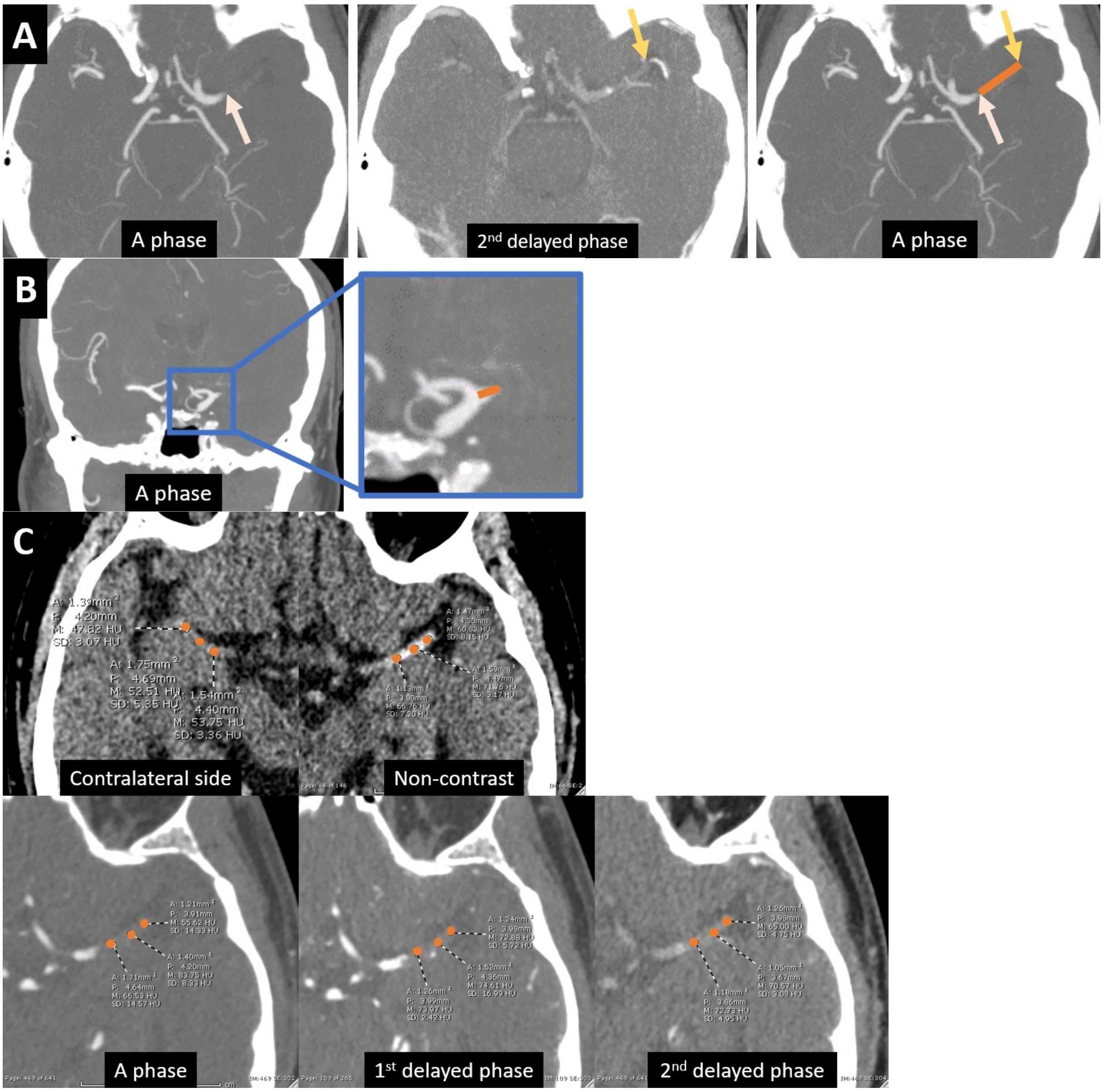

Figure 1. *Imaging analysis and ROI placement; (A, B) The clot length (orange line on Figure A), the location (pale orange arrow on Figure A) and DT (orange line on Figure B) were considered on the CTA MIP image. (C) Attenuation and heterogeneity of the clot acquiring from the three ROIs (orange dots) placed along the clot on all phases as well as the contralateral side on the non-contrast image.*

The degree of revascularization was assessed from the digital subtraction cerebral angiography study and graded by a neurointerventionist with five years of experiences using modified thrombolysis in the cerebral infarction (mTICI) score with the grade of at least mTICI 2b considered as successful revascularization [10]. The following additional information regarding the operation was collected: the puncture time, the reperfusion time, the method of thrombectomy (aspiration or stent retriever), the number of attempts, and immediate complications.

Statistical analysis

The baseline characteristics and thrombectomy data were calculated using frequency and percentage or the mean and standard deviation. In the case of categorical data, the Pearson Chi-Square Fisher's Exact tests were used. For numerical data, the student-t test was used. The logistic regression analysis was used to test the association between CT characteristics and success of the thrombectomy. The interobserver reliability was calculated using kappa statistics for categorical data and intraclass correlation for numerical data. A p-value less than 0.05 was considered statistically significantly different. Based on the precision of the 95%CI around the prevalence, the estimated sample size should be 120. All statistical analyses were performed using SPSS statistical software version 22.

Results

We collected 90 cases of acute anterior-circulation ischemic stroke undergoing endovascular thrombectomy during the mentioned period. We excluded 16 cases of clot locations occupying the petrous to the clinoid segment of ICA, 3 cases of spontaneous resolution, 1 case of failed treatment due to tortuous vessels, 6 cases of an undetermined exact clot location, and 5 cases of inadequate image quality. Finally, we reviewed 59 patients, consisting of 52 successful cases (88.1%), and 7 unsuccessful cases (11.9%).

Baseline data

The mean age and range were 65 years (range 25-89 years) in the successful group and 61 years (range 31-85 years) in the unsuccessful group. In both groups, there was a slight predominance of females, which was 63.5% in the successful group and 57.1% in the unsuccessful group. There was no significant difference in the underlying diseases, ongoing medications, intravenous thrombolytics, the hematocrit level, and NIHSS between two groups. Nonetheless, we found a significantly shorter period from last-seen-normal to puncture time in the successful group (6.8±4.6 hours versus 13±7.7 hours, p=0.003). The most common stroke etiology was a cardioembolic cause for both groups. There was one case of a methamphetamine-related cause. The data was summarized in Table 1.

Table 1. *Baseline data in successful and unsuccessful groups (age shown in mean (range); onset-to-puncture period and NIHSS shown in mean (SD); other parameters shown in n (percentage)).*

	Successful group (n=52)	Unsuccessful group (n=7)	P value
Age (year)	65 (25-89)	61 (31-85)	0.518
Sex (male/total)	19/52 (36.5%)	3/7 (42.9%)	1.000
Underlying disease			
Diabetes	10/52 (19.2%)	3/7 (42.9%)	0.173
Hypertension	20/52 (38.5%)	2/7 (28.6%)	0.702
Dyslipidemia	17/52 (32.7%)	2/7 (28.6%)	1.000
Previous ischemic stroke	9/52 (17.3%)	1/7 (14.3%)	1.000
Ischemic heart disease	8/52 (15.4%)	1/7 (14.3%)	1.000
Atrial fibrillation	22/52 (42.3%)	3/7 (42.9%)	1.000
Ongoing anti-platelet therapy	8/52 (15.4%)	0	0.578
Ongoing anticoagulant therapy	18/52 (34.6%)	2/7 (28.6%)	1.000
Intravenous thrombolytics	27/52 (51.9%)	2/7 (33.3%)	0.670
Last seen normal – puncture (hour)	6.8 (4.6)	13.0 (7.7)	0.003
Hematocrit	37.5 (5.5)	37.8 (6.2)	0.900
NIHSS	17.4 (4.8)	14.7 (3.5)	0.184
TOAST classification			
Cardioembolism	32/52 (61.5%)	4/7 (57.1%)	
Large vessel disease	3/52 (5.8%)	2/7 (28.6%)	
Indetermined source	17/52 (32.7%)	0	
Others	0	1/7 (14.3%)	

Thrombectomy-related data

The successful group consisted of 45 cases of mTICI 2b and 7 cases of mTICI 3, as shown in Table 2. The unsuccessful group consisted of 1 case of mTICI 0, 2 cases of mTICI 1, and 4 cases of mTICI 2a. There were 37 cases with first-pass success (62.7%).

The number of patients treated with aspiration-only, stent retriever-only, and combined methods were 47 cases, 6 cases, and 6 cases, respectively (p=0.438). Forty six of 53 patients (86.7%) were treated with aspiration thrombectomy using a 6F catheter, while 6 patients (11.3%) using a 5F catheter, and 1 patient (1.8%) using a 6.5F catheter. Patients underwent stent-retriever thrombectomy using various sizes of stents including 3x20 mm, 4x15 mm, 4x20 mm, 4x40 mm, 6x40 mm. The 4x20 mm stent was predominantly used (8/12 patients, 66.7%). The mean and SD of the number of attempts of the successful and unsuccessful groups were 1.5±1.0 times and 2.3±1.0 times, respectively (p=0.052). The mean procedure duration was 28.4 minutes in the successful group and 40.6 minutes in the unsuccessful group (p=0.488). There were 5 cases and 2 cases where immediate complications were developed in both groups, respectively (p=0.190). These complications were distal embolization and dissection.

Table 2. *Thrombectomy-related data (operating time shown in mean (SD); other parameters shown in n (percentage)).*

	Successful result (n=52)	Unsuccessful result (n=7)	P value
mTICI score			
0	-	1/7 (14.3%)	
1	-	2/7 (28.6%)	
2a	-	4/7 (57.1%)	
2b	45/52 (86.5%)	-	
3	7/52 (13.5%)	-	
First-pass success	37/52 (71.2%)	-	
Method			0.438
Aspiration only	42/52 (80.8%)	5/7 (71.4%)	
Stent retriever only	5/52 (9.6%)	1/7 (14.3%)	
Combined	5/52 (9.6%)	1/7 (14.3%)	
Operating time (minute)	28.4 (15.3)	40.6 (43.3)	0.488
Complication	5/52 (9.6%)	2/7 (28.6%)	0.190

CT clot characteristics and association with outcomes

There was no significant difference in the clot location between the successful and unsuccessful groups (p=0.066). The most common location was M1 segment of the MCA in the successful group (34/52 patients, 65.4%) and M2 segment of the MCA in the unsuccessful group (4/7 patients, 57.1%). There were 8 cases and 1 case of a supraclinoid ICA-located clot in the successful and unsuccessful groups, respectively. There was no clot location in A1 or A2 segments of the ACA. The mean and SD of the CBS and clot length in the successful group were 3.2±1.7 and 13.7±7.0 mm, slightly higher than those of the unsuccessful group (2.3±2.2 and 10.0±6.4 mm). The mean DT of the unsuccessful group was 16.4 mm, which was significantly longer than the mean of 8.5 mm in the successful group (p=0.046).

However, there was no statistically significant association between the DT and the successful outcome (p=0.061). The absolute attenuation (56.1±8.9 HUs versus 56.3±10.7 HUs), relative attenuation (1.3±0.3 versus 1.4±0.4), heterogeneity (5.5±1.0 HUs versus 5.9±1.5 HUs), and perviousness (9.8±12.8 HUs versus 8.1±15.5 HUs) between the two groups showed no statistically significant difference. There was no significant association between the clot location, parameters, and successful outcomes. Table 3 summarizes overall clot characteristics between the successful and unsuccessful groups and Table 4 shows the binary logistic regression of the CT clot characteristics and the successful outcome.

Table 3. *CT clot characteristics and success of thrombectomy (location data shown in n (percentage); other parameters shown in mean (SD)).*

	Successful result (n=52)	Unsuccessful result (n=7)	P value
Location			0.066
Supraclinoid ICA	8/52 (15.4%)	1/7 (14.3%)	
M1 MCA	34/52 (65.4%)	2/7 (28.6%)	
proximal M1	17/52 (32.7%)	0	
distal M1	17/52 (32.7%)	2/7 (28.6%)	
M2 MCA	10/52 (19.2%)	4/7 (57.1%)	
Clot burden score	3.2 (1.7)	2.3 (2.2)	0.197
Length (mm)	13.7 (7.0)	10.0 (6.4)	0.190
Distance from terminal ICA (mm)	8.5 (9.1)	16.4 (13.2)	0.046
Absolute attenuation (HU)	56.1 (8.9)	56.3 (10.7)	0.967
Heterogeneity (HU)	5.5 (1.0)	5.9 (1.5)	0.451
Relative attenuation	1.3 (0.3)	1.4 (0.4)	0.405
Perviousness (HU)	9.8 (12.8)	8.1 (15.5)	0.755

Table 4. *Binary logistic regression analysis between CT clot characteristics and success of thrombectomy.*

	OR	95% CI	P-value
Location			
Supraclinoid ICA	1 (reference)		
M1 MCA	2.13	0.17-26.44	0.558
M2 MCA	0.31	0.03-3.38	0.338
Clot burden score	1.43	0.82-2.48	0.204
Length	1.11	0.95-1.29	0.199
Distance from terminal ICA	0.94	0.87-1.00	0.061
Absolute attenuation	1.00	0.91-1.09	0.966
Heterogeneity	0.71	0.34-1.46	0.349
Relative attenuation	0.34	0.03-4.23	0.401
Perviousness	1.01	0.95-1.08	0.750

Furthermore, we determined if the patients had the hyperdense vessel sign which was considered positive when the relative attenuation was ≥1.16 [4]. There were 41 positive cases (78.8%) in the successful group and 5 positive cases (71.4%) in the unsuccessful group (p=0.643). The ratio of clot attenuation and the hematocrit level of each patient was calculated. The mean and SD of this ratio was 1.5±0.3 in the successful group and 1.5±0.4 in the unsuccessful group (p=0.897).

There was no significant association between the CT clot characteristics and the immediate complication.

Interobserver reliability
We achieved an excellent agreement in location determination with the Kappa coefficient of 0.93. The Kappa coefficients of each segment involvement of the supraclinoid ICA, proximal M1 segment, distal M1 segment, M2 segment, A1 segment, and A2 segment were 1.00, 0.90, 0.78, 0.56, 0.81, and 1.00, respectively. The intra-class correlation coefficient (ICC) for CBS was 0.93. The ICCs for the clot length and DT were 0.94, and 0.95, respectively. The ICCs for the attenuation ranged from 0.54 to 0.83. The ICC for the heterogeneity was 0.46.

Discussion

According to the TOAST classification, there were 36 cases (61.0%) of the cardioembolic cause, 5 cases (8.5%) of large vessel atherosclerosis, 17 cases (28.8%) of an undetermined cause and 1 case of the methamphetamine-related cause. Roessler et al showed 44% of their cases having the cardioembolic cause, followed by 24.8% of undetermined etiology and 21.6% of large vessel atherosclerosis [11]. However, Boodt et al showed 49.8% of undetermined etiology as the most common type, followed by 33% of cardioembolism and 13% of large vessel atherosclerosis [12]. Although compared with cardioembolism, large artery atherosclerosis was generally more prevalent in the Asian population [13], our study showed a low proportion of the large vessel atherosclerosis. This might be because we included only thrombectomy cases and unintentionally excluded the majority of this type of stroke.

Our study consisted was of 59 cases of acute anterior circulation ischemic stroke patients undergoing endovascular thrombectomy with 52 successful cases (88.1%). Other studies showed similar success rates with 84.6% from the Byun study [3] and 86.0% from the MR CLEAN registry [4].

Most of our cases underwent aspiration thrombectomy as the primary method upon the preference of the interventionists with 47 cases (79.7%) undergoing the aspiration-only method. Although many previous studies used the stent retriever method as a primary method with an overall success rate of 86.0-89.2% [4,5], our study showed a success rate comparable to theirs. Moreover, Mokin et al showed no significant difference in the thrombectomy outcome between aspiration first group (93.8%) and stent retriever first group (91.6%) [5]. Schartz et al. meta-regression analysis study revealed a significant association between the increasing aspiration catheter internal diameter and the first pass effect, and between the internal diameter and the final recanalization. Our cases were treated with aspiration thrombectomy, and nearly uniform catheter size (6F catheter, 86.7%) was used in the combined methods. The influence of the aspiration catheter diameter was not exhibited in our study [14].

Despite the existence of many studies, there have been differing results on whether CT clot characteristics could predict reperfusion after endovascular thrombectomy. Extensive studies about the clot composition have been conducted giving the enlightenment of the wide range of various clot components and their proportions as well as their clinical relevance [15-18]. Some studies showed a significant association between the hyperdense artery sign and the RBC content of the clot [17, 19]. Gunning et al found that the clot with more RBC content had lower friction coefficient [20]. Furthermore, there were some studies showing a higher success rate in the patients with a higher-density clot [5, 21]. However, several studies with larger numbers of patients showed no association between the clot density and the successful outcome [2, 4, 22, 23]. In our study, there was no significant association between the clot attenuation and the successful thrombectomy. We weighed the clot attenuation with the contralateral artery attenuation and the hematocrit level as well as categorized patients with the hyperdense vessel sign. Still, we found no association of these corrected/modified attenuation parameters and the outcome. Therefore, our study supported the result of the majority.

The clot compositions are typically a mixture of fibrin, platelets, white blood cells and red blood cells (RBC) resulting in clot heterogeneity. Increased RBC content is proposed associated with vulnerability to treatment with intravenous thrombolysis or mechanical thrombectomy. While an increased fibrin or platelet content is supposed to be associated with resistance to treatment. The platelet-rich areas contain dense fibrin, von Willebrand factor (vWF), abundant leukocytes and extracellular DNA, which are potentially responsible for resistance to thrombolysis and thrombectomy [24, 25]. Liu et al found that more spatial heterogeneity of the clot on the histology was associated with less first-pass success, which was assumed to be due to the higher fragility [26]. To the best of our knowledge, there is no published study demonstrating the association between the radiologic clot heterogeneity and the outcome of thrombectomy. We gathered the average of the SD of the attenuation of the clot which we believed would represent the heterogeneity of the clot composition. Our results showed no significant difference in the SD between two groups. The important drawback was that the SD value of the clot was highly spatially variable, and we did not place more than three ROIs on the clot regardless of the clot length. The long-length clots went through under-sampling. This could be the main source of the relatively low interobserver reliability among all CT parameters. Hence, further studies should give insights on this issue with an entire clot length analysis, and the correlation between radiologic heterogeneity and histologic heterogeneity should be sought out.

There has been conflicting data regarding the clot perviousness and the thrombectomy outcome. Mokin et al dichotomized the patients and found that the high perviousness group had been associated with higher rates of first-pass success in the aspiration first group but not in the stent retriever first group [22]. In addition, Benson's study showed that higher perviousness had been associated with higher RBC density and lower fibrin density, which could provide the possible explanation of higher first-pass success in the more pervious clot [27]. In contrast, Patel et al showed a positive correlation between the perviousness and the percent of fibrin/platelet aggregates [16]. They also showed a negative correlation between the perviousness and the first-pass success, but there was no statistical significance ($p=0.055$). Our results showed no significant association between perviousness and the successful outcome as well as Dutra et al results [4]. We believe that this inconclusive result might be associated with the number of factors contributing to the measured clot perviousness, not only because of the proportion of the clot composition but also its distribution and density as well as the hemodynamic status of the patient, the imaging protocol, and measurement methods.

Aside from the clot composition, clot location, clot length and DT have also been studied for a decade. We demonstrated significant differences between the DT of the two groups (p=0.046), but no significant association with the thrombectomy outcome (p=0.061). A few studies showed that DT could potentially predict the thrombectomy outcome in the case of M1 occlusion since they found that shorter DT was associated with more success rate [28, 29]. However, Dutra et al found no association between the DT and the thrombectomy outcomes regardless of the location [4].

Sujijantara et al conducted a meta-analysis of the impact of the clot location after thrombectomy and found no difference in recanalization success by the clot location [7]. However, there was a large study showing a significant association between proximal and distal M1 locations and successful reperfusion [4]. In our study, there were 2 unsuccessful cases (5.6%) among all 36 cases of M1-located clots, while there were 4 unsuccessful cases (28.6%) among 14 cases of M2-located clots. This result might be concordantly related to the shorter DT in the successful group. Despite the apparently different proportions, our result demonstrated no significant association between the location and the successful outcome. Further studies with a greater number of cases would help clarify this inconclusive association among the location, DT, and the thrombectomy outcome.

According to our result, the clot length showed no association with the successful outcome. A few studies also found no association between the clot length and the thrombectomy outcome whether using a stent retriever or an aspiration method [4, 30, 31]. Guenego et al found the association between the angulated or the bifurcated clot shape in M1 segment detected by T2*WI MRI and a poorer thrombectomy outcome [32]. Further studies of the CT clot shape might find a significant association.

Mokin et al performed a subgroup analysis of the SWIFT PRIME study and classified acute ischemic stroke patients into three groups, according to CBS from single phase CTA. They found indifferent high rates of reperfusion in all three groups using the stent retrieve method (86.2%-100%) [5]. Other studies including ours shared the same result [4]. In addition, we acquired CBS from the multiphase CTA, which could dissolve their limitation of clot extension overestimation to some degree.

Knowledge about the clot composition and its association with imaging findings are supposed to influence the treatment outcome. Our study showed unenhanced CT and multi-phase CTA brain were reliable non-invasive imaging methods and should be used for assessment of the occlusive thrombus in acute ischemic stroke. A shorter distance of the clot from the terminal ICA was found in successful thrombectomy patients than unsuccessful patients in our study.

We noticed a few limitations in our study. First, there was a small and inadequate number of patients, particularly the unsuccessful patients. Therefore, there would be insufficient statistical power and a statistically nonsignificant result. Second, this study was conducted in a single tertiary care center, inevitably resulting in the selection bias. Third, all the ROIs were placed manually on all phases of images without co-registration software. However, the majority of the interobserver reliability was satisfactory. Lastly, the numerical data from the ROI did not represent the whole clot length. This might mainly influence the clot with heterogeneous composition along its length. The novel imaging techniques and availability of the co-registration software will also provide more reliable results. In addition, further studies with greater numbers of cases are needed to confirm our results.

Conclusion

Our study found the distance of the clot from the terminal ICA was shorter in the successful thrombectomy cases. There was no association between other CT clot characteristics on non-contrast CT and multi-phase CTA and the endovascular thrombectomy outcome in acute anterior circulation ischemic stroke.

References

1. Powers WJ, Derdeyn CP, Biller J, Coffey CS, Hoh BL, Jauch EC, et al. 2015 American Heart Association/American Stroke Association focused update of the 2013 guidelines for the early management of patients with acute ischemic stroke regarding endovascular treatment: a guideline for healthcare professionals from the American Heart Association/American Stroke Association. Stroke 2015;46:3020-35. doi: 10.1161/STR.0000000000000074.

2. Borst J, Berkhemer OA, Santos EMM, Yoo AJ, den Blanken M, Roos Y, et al. Value of Thrombus CT characteristics inpatients with acute ischemic stroke. AJNR Am J Neuroradiol 2017;38:1758-64. doi: 10.3174/ajnr.A5331.

3. Byun JS, Nicholson P, Hilditch CA, Chun On Tsang A, Mendes Pereira V, Krings T, et al. Thrombus perviousness is not associated with first-pass revascularization using stent retrievers. Interv neuroradiol 2019;25:285-90. doi: 10.1177/1591019918825444.

4. Dutra BG, Tolhuisen ML, Alves HCBR, Treurniet KM, Kappelhof M, Yoo AJ, et al. Thrombus imaging characteristics and outcomes in acute ischemic stroke patients undergoing endovascular treatment. Stroke 2019;50:2057-64. doi: 10.1161/STROKEAHA.118.024247.

5. Mokin M, Levy EI, Siddiqui AH, Goyal M, Nogueira RG, Yavagal DR, et al. Association of clot burden score with radiographic and clinical outcomes following solitaire stent retriever thrombectomy: analysis of the SWIFT PRIME trial. J Neurointerv Surg 2017;9:929-32. doi: 10.1136/neurintsurg-2016-012631.

6. Puetz V, Dzialowski I, Hill MD, Subramaniam S, Sylaja PN, Krol A, et al. Intracranial thrombus extent predicts clinical outcome, final infarct size and hemorrhagic transformation in ischemic stroke: the clot burden score. Int J Stroke 2008;3:230-6. doi: 10.1111/j.1747-4949.2008.00221.x.

7. Sujijantarat N, Koo AB, Elsamadicy AA, Hebert RM, Cord BJ, Navaratnam D, et al. Impact of clot location on outcomes after mechanical thrombectomy for anterior circulation acute ischemic stroke: a meta-analysis. Neurosurgery 2020;87(Suppl1).

8. Dundamadappa S, Iyer K, Agrawal A, Choi DJ. Multiphase CT angiography: a useful technique in acute stroke imaging-collaterals and beyond. AJNR Am J Neuroradiol 2021;42:221-7. doi: 10.3174/ajnr.A6889.

9. Santos EMM, d'Esterre CD, Treurniet KM, Niessen WJ, Najm M, Goyal M, et al. Added value of multiphase CTA imaging for thrombus perviousness assessment. Neuroradiology 2018;60:71-9. doi: 10.1007/s00234-017-1907-y.

10. Zaidat OO, Yoo AJ, Khatri P, Tomsick TA, von Kummer R, Saver JL, et al. Recommendations on angiographic revascularization grading standards for acute ischemic stroke: a consensus statement. Stroke 2013;44:2650-63. doi: 10.1161/STROKEAHA.113.001972.

11. Roessler FC, Kalms N, Jann F, Kemmling A, Ribbat-Idel J, Stellmacher F, et al. First approach to distinguish between cardiac and arteriosclerotic emboli of individual stroke patients applying the histological THROMBEX-classification rule. Sci Rep 2021;11:8433. doi: 10.1038/s41598-021-87584-2.

12. Boodt N, Compagne KCJ, Dutra BG, Samuels N, Tolhuisen ML, Alves HCBR, et al. Stroke etiology and thrombus computed tomography characteristics in patients with acute ischemic Stroke: A MR CLEAN Registry Substudy. Stroke 2020;51):1727-35. doi: 10.1161/STROKEAHA.119.027749.

13. Kim BJ, Kim JS. Ischemic stroke subtype classification: an asian viewpoint. J Stroke 2014;16:8-17. doi: 10.5853/jos.2014.16.1.8.

14. Schartz D, Ellens N, Kohli GS, Rahmani R, Akkipeddi SMK, Colby GP, et al. Impact of aspiration catheter size on clinical outcomes in aspiration thrombectomy. J Neurointerv Surg 2023;15:e111-e6. doi: 10.1136/jnis-2022-019246.

15. Staessens S, De Meyer SF. Thrombus heterogeneity in ischemic stroke. Platelets 2021;32:331-9. doi: 10.1080/09537104.2020.1748586.

16. Patel TR, Fricano S, Waqas M, Tso M, Dmytriw AA, Mokin M, et al. Increased perviousness on CT for acute ischemic stroke is associated with fibrin/platelet-rich clots. AJNR Am J Neuroradiol 2021;42:57-64. doi: 10.3174/ajnr.A6866.

17. Brinjikji W, Duffy S, Burrows A, Hacke W, Liebeskind D, Majoie C, et al. Correlation of imaging and histopathology of thrombi in acute ischemic stroke with etiology and outcome: a systematic review. J Neurointerv Surg 2017;9:529-34. doi: 10.1136/neurintsurg-2016-012391.

18. Jolugbo P, Ariëns RAS. Thrombus composition and efficacy of thrombolysis and thrombectomy in acute ischemic stroke. Stroke 2021;52:1131-42. doi: 10.1161/STROKEAHA.120.032810.

19. Liebeskind DS, Sanossian N, Yong WH, Starkman S, Tsang MP, Moya AL, et al. CT and MRI early vessel signs reflect clot composition in acute stroke. Stroke 2011;42:1237-43. doi: 10.1161/STROKEAHA.110.605576.

20. Gunning GM, McArdle K, Mirza M, Duffy S, Gilvarry M, Brouwer PA. Clot friction variation with fibrin content; implications for resistance to thrombectomy. J Neurointerv Surg 2018;10:34-8. doi: 10.1136/neurintsurg-2016-012721.

21. Froehler MT, Tateshima S, Duckwiler G, Jahan R, Gonzalez N, Vinuela F, et al. The hyperdense vessel sign on CT predicts successful recanalization with the Merci device in acute ischemic stroke. J Neurointerv Surg 2013;5:289-93. doi: 10.1136/neurintsurg-2012-010313.

22. Mokin M, Waqas M, Fifi J, De Leacy R, Fiorella D, Levy EI, et al. Clot perviousness is associated with first pass success of aspiration thrombectomy in the COMPASS trial. J Neurointerv Surg 2021;13:509-14. doi: 10.1136/neurintsurg-2020-016434.

23. Yilmaz U, Roth C, Reith W, Papanagiotou P. Thrombus attenuation does not predict angiographic results of mechanical thrombectomy with stent retrievers. AJNR Am J Neuroradiol 2013;34:2184-6. doi: 10.3174/ajnr.A3565.

24. Brouwer PA, Brinjikji W, De Meyer SF. Clot pathophysiology: Why Is It clinically important? Neuroimaging Clin N Am 2018;28:611-23. doi: 10.1016/j.nic.2018.06.005.

25. Dumitriu LaGrange D, Reymond P, Brina O, Zboray R, Neels A, Wanke I, et al. Spatial heterogeneity of occlusive thrombus in acute ischemic stroke: A systematic review. J Neuroradiol 2023;50:352-60. doi: 10.1016/j.neurad.2023.01.004.

26. Liu Y, Brinjikji W, Abbasi M, Dai D, Arturo Larco JL, Madhani SI, et al. Quantification of clot spatial heterogeneity and its impact on thrombectomy. J Neurointerv Surg 2022;14:1248-52. doi: 10.1136/neurintsurg-2021-018183.

27. Benson JC, Fitzgerald ST, Kadirvel R, Johnson C, Dai D, Karen D, et al. Clot permeability and histopathology: is a clot's perviousness on CT imaging correlated with its histologic composition? J Neurointerv Surg 2020;12:38-42. doi: 10.1136/neurintsurg-2019-014979.

28. Pavabvash S, Taleb S, Majidi S, Qureshi AI. Correlation of acute M1 middle cerebral artery thrombus location with endovascular treatment success and clinical outcome. J Vasc Interv Neurol 2017;9:17-22.

29. Sengeze N, Giray S. Distance to thrombus in endovascular treatment of middle cerebral artery M1 occlusion predicts recanalization success and clinical outcome. Arch Iran Med 2021;24:113-7. doi: 10.34172/aim.2021.17.

30. Seker F, Pfaff J, Wolf M, Schönenberger S, Nagel S, Herweh C, et al. Impact of thrombus length on recanalization and clinical outcome following mechanical thrombectomy in acute ischemic stroke. J Neurointerv Surg 2017;9:937-9. doi: 10.1136/neurintsurg-2016-012591.

31. Yoo AJ, Khatri P, Mocco J, Zaidat OO, Gupta R, Frei D, et al. Impact of thrombus length on outcomes after intra-arterial aspiration thrombectomy in the THERAPY trial. Stroke 2017;48:1895-900. doi: 10.1161/STROKEAHA.116.016253.

32. Guenego A, Fahed R, Sussman ES, Leipzig M, Albers GW, Martin BW, et al. Impact of clot shape on successful M1 endovascular reperfusion. Front Neurol 2021;12:642877. doi: 10.3389/fneur.2021.642877.

Original Article

Reliability and radiologists' concordance of artificial intelligence (AI)-calculated Alberta Stroke Program Early CT Score (ASPECTS)

Warissara Kiththiworaphongkich, M.D.
Nuttamon Khamwongsa, B.Sc.
Pranruethai Chaimongkol, B.Sc.
From Department of Radiology, Phayao Hospital, Phayao, Thailand.
Address correspondence to W.K. (email: bow_wk@hotmail.com)

Received 19 March 2024; revised 10 December 2024; accepted 10 December 2024
doi:10.46475/asean-jr.v25i3.901

Abstract

Background: ASPECTS was developed for the semi-quantitative assessment of early ischemic changes (EIC) on non-contrast computed tomography (NCCT) in acute ischemic stroke (AIS). Artificial intelligence (AI)-based automated tools for the ASPECT scoring system were developed to automate the diagnosis and improve the agreement with radiologists of AIS. The performance of the automated software compared to physicians should be tested before the software is further used in clinical practice as a tool for clinicians.

Objective: To evaluate the agreement with radiologists of an AI-based automated post-processing software for detecting EIC and calculating ASPECTS on NCCT images in AIS patients using a radiologist's assessment as a reference.

Materials and Methods: NCCT of AIS patients were retrospectively reviewed (Stroke Fast Track Service July 2022 - December 2023). The complete set of clinical data and imaging data from both baseline and follow-up were analyzed by a radiologist as a reference. Two additional observers provided individual ASPECTS from the baseline NCCT only (observer 1 was a radiologist who independently reviewed only the baseline NCCT with stroke window setting. Observer 2 was a radiologist on service which was from the pool of 20 radiologists onsite and online). Recon&GO Inline ASPECTS software (Somaris X, VA40A, Siemens Healthineers AG, Erlangen, Germany) was applied. Both ASPECT score analysis and ASPECTS region analysis were evaluated. Positive percent agreement (PPA) and negative percent agreement (NPA) were calculated. Interobserver agreement was assessed using the Cohen's kappa coefficient and the intraclass correlation coefficient (ICC).

Results: 111 patients with a mean age of 67.8 years (±11.9), 56 (50.5%) females, a mean National Institute of Health Stroke Scale (NIHSS) score of 14.2 (±8.8), and a mean time to baseline NCCT of 123.9 minutes (±58.7) were included. For dichotomized ASPECTS, the automated software showed lower PPA (14.6% vs. 27.1%) but higher NPA (100.0% vs. 93.7%) than observer 2. For the region-based analysis, both the automated software and observer 2 differed in terms of regional contribution. The automated software showed low PPA but rather high NPA with perfect (100%) NPA in lentiform nucleus and M2. The automated software showed higher agreement with the reference and two observers in deep/central regions than cortical regions. For total ASPECTS, the automated software showed a moderate agreement of total ASPECTS with the reference and observer 1 (ICC = 0.545 and 0.545). Observer 2 showed a poor agreement of total ASPECTS with the reference, observer 1, and the automated software (ICC = 0.349, 0.422, and 0.301, respectively).

Conclusion: For total ASPECT score, the agreement of the tested AI software is lower compared to observer 1 obtained by a radiologist using the stroke window on NCCT, but better compared to a pool of radiologists on service with a time limit of 30 minutes to interpret the ASPECT score. When analyzing the ASPECTS regions, there are different advantages for the assessment of the deep regions and the cortical regions. The tested AI software shows higher agreement in deep/central regions than cortical regions. From the result, the tested AI software retains its potential for use in emergency situations, particularly for radiologists with limited experience and limited time to report.

Keywords: Acute ischemic stroke, Alberta Stroke Program Early CT Score, Artificial intelligence, Computed tomography.

Introduction

Ischemic stroke is one of the acute cerebrovascular diseases that is the leading cause of death and severe disabilities worldwide and places an enormous burden on global and national healthcare systems [1, 2]. An acute ischemic stroke (AIS) that is not appropriately interpreted and treated carries a high risk of mortality and disability. Management of an ischemic stroke should be prompt so that appropriate treatment can be initiated and the patient has the best chance of survival. Time is of the essence: the faster the diagnosis is made and the appropriate treatment is initiated, the better the outcome for the patient [3].

In Thailand, the National Health Security Office (NHSO) has supported the free treatment of patients with AIS with thrombolytics since 2008 [4]. Subsequently, the above-mentioned treatment services were expanded into a "Stroke Fast Track" as a stroke service network in all areas of Thailand. This service network aims to ensure that the time from the onset of the patient's neurological symptoms to intravenous thrombolytic treatment is as fast as possible within 270 minutes (4.5 hours) [4]. Recently, the treatment of AIS has developed rapidly due to a highly effective endovascular therapy [5-11]. Endovascular therapy with mechanical thrombectomy (MT) is the current standard of care for patients with AIS and large vessel occlusions (LVO) [12, 13]. Nowadays, the time window for treatment of AIS is generally 6 hours after the onset of the patient's neurological symptoms.

The diagnosis of AIS is based on clinical examination and neuroimaging techniques. Neuroimaging techniques (including CT and MRI) have become an integral approach for the detection and characterization of AIS and the prediction of prognosis. The severity and extent of an ischemic stroke lesion could be used as one of the parameters for the selection of patients for MT [14]. Non-contrast computed tomography (NCCT) of the brain is the most widely used method for assessing the early signs of ischemic brain change in stroke patients. The Alberta Stroke Program Early CT Score (ASPECTS) is a tool for semi-quantitative assessment of early ischemic changes (EIC) on NCCT of patients with AIS in the anterior circulation [15, 16]. Since 2000, the ASPECTS has been widely used to detect the extent of EIC, assess the impact of treatment, and predict the prognosis [17]. The guidelines for early management of AIS recommend the use of the ASPECTS to identify patients suitable for MT. A score of ≥ 6 is an important cut-off value and one of the criteria that qualify patients for MT [13] and thrombolytic treatment. Nevertheless, the early brain imaging changes, including loss of the normal gray-white matter interface and effacement of the cortical sulci, can be subtle and make it particularly difficult for clinicians to recognize them and determine the optimal management in an emergency scenario. ASPECT scoring requires a high level of expertise to detect subtle changes in the NCCT in the early phase of brain ischemia [18]. Expertise is not available in every center where stroke patients are presented.

Recently, artificial intelligence (AI) technology has greatly impacted the field of stroke image analysis by automating diagnosis and improving the diagnostic accuracy of AIS [19]. Many tools for stroke image analysis have been developed to reduce the time needed to detect abnormalities and to provide more accurate results [20]. Several studies reported the use of AI-based automated software versus radiologists for the diagnosis of AIS on CT or MR imaging, such as detection of subtle changes in attenuation on NCCT [21], the automatic ASPECTS scoring system for the AIS area on CT and MRI [22, 23], detection of the hyperdense sign of the middle cerebral artery (MCA) on CT [24] and the automatic quantification of cerebral edema on CT [25]. Recon&GO Inline ASPECTS software, the AI-based automated post-processing ASPECTS software in this study was developed by Siemens. Several studies reported on the use of automated ASPECTS software compared to radiologists. Any automated software may lead to different diagnostic outcomes. However, no study has investigated this software.

The AI-based automated post-processing ASPECTS software has been used in Phayao Hospital since July 2022. However, the performance of the AI-based automated post-processing software should be tested with physicians before this software is further used in clinical practice as a tool for clinicians. Therefore, this study was designed to evaluate the agreement with radiologists of the AI-based automated post-processing software for detecting EIC and calculating the ASPECTS on the NCCT in AIS patients (including patients in the stroke fast track service), using a radiologist's assessment as a reference. Imaging data from the baseline and the follow-up were evaluated as a reference.

Materials and methods

Study participants

Data from consecutive patients who were presented to the stroke fast track service in Phayao Hospital between July 2022 and December 2023 and underwent multimodality brain CT for suspected AIS and met the inclusion criteria were retrospectively identified using the Radiologic Information System and the Picture Archiving and Communication System. The inclusion criteria were: (1) the patient was ≥18 years old, (2) the baseline multimodal NCCT was performed within 270 minutes (4.5 hours) of symptom onset or last seen normal, and (3) the AIS was located in the middle cerebral artery (MCA) territory. Exclusion criteria were: (1) patients with intracranial hemorrhage or other diagnoses explaining the symptoms, such as tumor, infection, ischemic stroke within the anterior cerebral artery (ACA) or posterior circulation, and (2) patients with a previous brain surgery or bilateral old large territorial infarction, and (3) no follow-up CT or CTA performed within 7 days of the baseline NCCT. The detailed flowchart of the patient selection process is shown in Figure 1.

Imaging data and evaluation by radiologists

All patients in this study received the same CT scan protocol, including NCCT scans of the brain on a 32-row detector/192-slice multidetector CT scanner (SOMATOM go.All, Siemens Healthineers AG, Forchheim, Germany). The NCCT scans were acquired in the helical mode with the following parameters: 0.7 mm slice collimation, spiral pitch factor of 0.55, tube voltage of 120 kV, and image matrix 512 x 512. The images were reconstructed in 1 mm overlapping sections. Axial images were reconstructed with a slice thickness of 1 mm and 5 mm. Coronal and sagittal multiplanar reconstructions were performed with a slice thickness of 3 mm.

For the manual ASPECTS assessment, a radiologist (with 9 years of experience) independently reviewed only the baseline NCCT with stroke window setting (window level of 35 Hounsfield units (HU) and width of 30 HU [26]) to create the

ASPECT score, hereafter referred to as observer 1. For this assessment, the reader was only aware of the sidedness of neurological deficit and did not have access to the follow-up NCCT.

In addition, each baseline NCCT was regularly assessed by a pool of twenty radiologists on service (two radiologists at Phayao Hospital and eighteen teleradiologists) who were prospectively assigned to read NCCT in the stroke fast-track procedure (hereafter referred to as observer 2). Their results were recorded for analysis, which corresponded to the actual situation.

Eight weeks later, the same radiologist (observer 1) independently performed an ASPECTS assessment using the completed set of available baselines NCCT, follow-up NCCT and/or CTA, and digital subtraction angiography (DSA) as the reference. The reader was blinded to the result of the automated software evaluation. Meeting criteria 1 + 2 or 2 +3 or 1 + 2 + 3 was defined as EIC on baseline NCCT: (1) presence of hypodensity and/or loss of gray-white differentiation, (2) ischemic changeable on follow-up NCCT, (3) Any individual region of hypodensity occupying ≥20% of that region. Existing hyperdense MCA signs were also additionally recorded. The reader was informed of the sidedness of neurological deficit and clinical data.

Automated calculation of ASPECTS

For comparison, the Recon&GO Inline ASPECTS software (Somaris X, VA40A, Siemens Healthineers AG, Erlangen, Germany), was used to analyze the NCCT for EIC in acute stroke in the MCA territory as well as the automatically calculated ASPECTS. The data sets of the post-processed axial NCCT reconstruction of the brain with a slice thickness of 5 mm, a matrix size of 512 x 512 and a smooth kernel reconstruction are prerequisites for the evaluation.

An artificial intelligence (AI) recognizes the patient's landmarks and anatomy. A probabilistic atlas was automatically created to outline the ASPECTS regions (caudate nucleus (C), internal capsule (IC), insula (INS), lentiform nucleus (LN), and 6 regions in the vascular territory of the MCA (M1–M6)). This brain atlas consists of ten volumes of interest for each hemisphere, representing ten ASPECTS regions. The regions from the atlas are resized and both rigidly and non-rigidly registered to the current dataset. Registration may be incorrect for unusual brain anatomies, such as young patients, large ventricles, old infarcts, open skulls, midline shifts or tumors.

After automatically fitting the atlas to an NCCT of the brain, each voxel is assigned a probability of belonging to a particular ASPECTS region. The average Hounsfield unit (HU) values of the brain tissue voxels of each region are calculated. Voxels that are either too dark or too bright are excluded from the calculation. Cerebrospinal fluid, old infarcts, bones, and calcifications as well as voxels that are either too dark (below 10 HU) or too bright (above 55 HU) are excluded. For regions M1 to M6, the average HU value is mainly based on gray matter. The relative difference in average HU between the single ASPECTS region in the affected hemisphere and the contralateral hemisphere is calculated and presented as a percentage HU difference. The affected cerebral hemisphere is automatically selected by the software. Based on a predefined threshold for the relative HU difference, each ASPECTS region in the affected hemisphere is classified as affected (ischemic changes detected by the software) or unaffected. The affected regions are marked (X). Any calculation result marked with an X indicates a region with lower HU values compared to the other hemisphere. Bold text indicates regions that are visible in the layer. In regions M1 to M6, the white matter may be affected in regions marked with WM. The number of affected regions is used to calculate ASPECTS (without the regions marked with WM). If a region is marked, the ASPECT score is reduced. Below the affected hemisphere, the automated ASPECTS provides a score from 0 (most severe) to 10 (least severe) (Figure 2).

Statistical analysis

All statistical analyses were performed with SPSS (version 26.0.0; IBM, Armonk, NY, USA). Continuous variables are presented as mean ± standard deviation (SD), while categorical data were presented as frequencies (percentages). The performance of the automated ASPECTS and the individual observers (1 and 2) compared to the reference was taken into account: (1) positive percent agreement

(PPA) and negative percent agreement (NPA) for each individual ASPECTS region on the correct side and dichotomized ASPECTS (≥6 and <6), (2) interobserver agreement for each individual ASPECTS region and dichotomized ASPECTS (≥6 and <6) were assessed using the Cohen's kappa coefficient. For the Cohen's kappa coefficient, values < 0 indicate poor agreement, values between 0.00 and 0.20 indicate slight agreement, values between 0.21 and 0.40 indicate fair agreement, values between 0.41 and 0.60 indicate moderate agreement, values between 0.61 and 0.80 indicate substantial agreement, and values between 0.81 and 1.00 indicate almost perfect agreement [27], (3) interobserver agreement for total ASPECTS was assessed using the intraclass correlation coefficient (ICC). For the ICC, values < 0.5 indicate poor agreement, values between 0.5 and < 0.75 indicate moderate agreement, values between 0.75 and < 0.9 indicate good agreement, and values between 0.9 and 1.0 indicate excellent agreement [28].

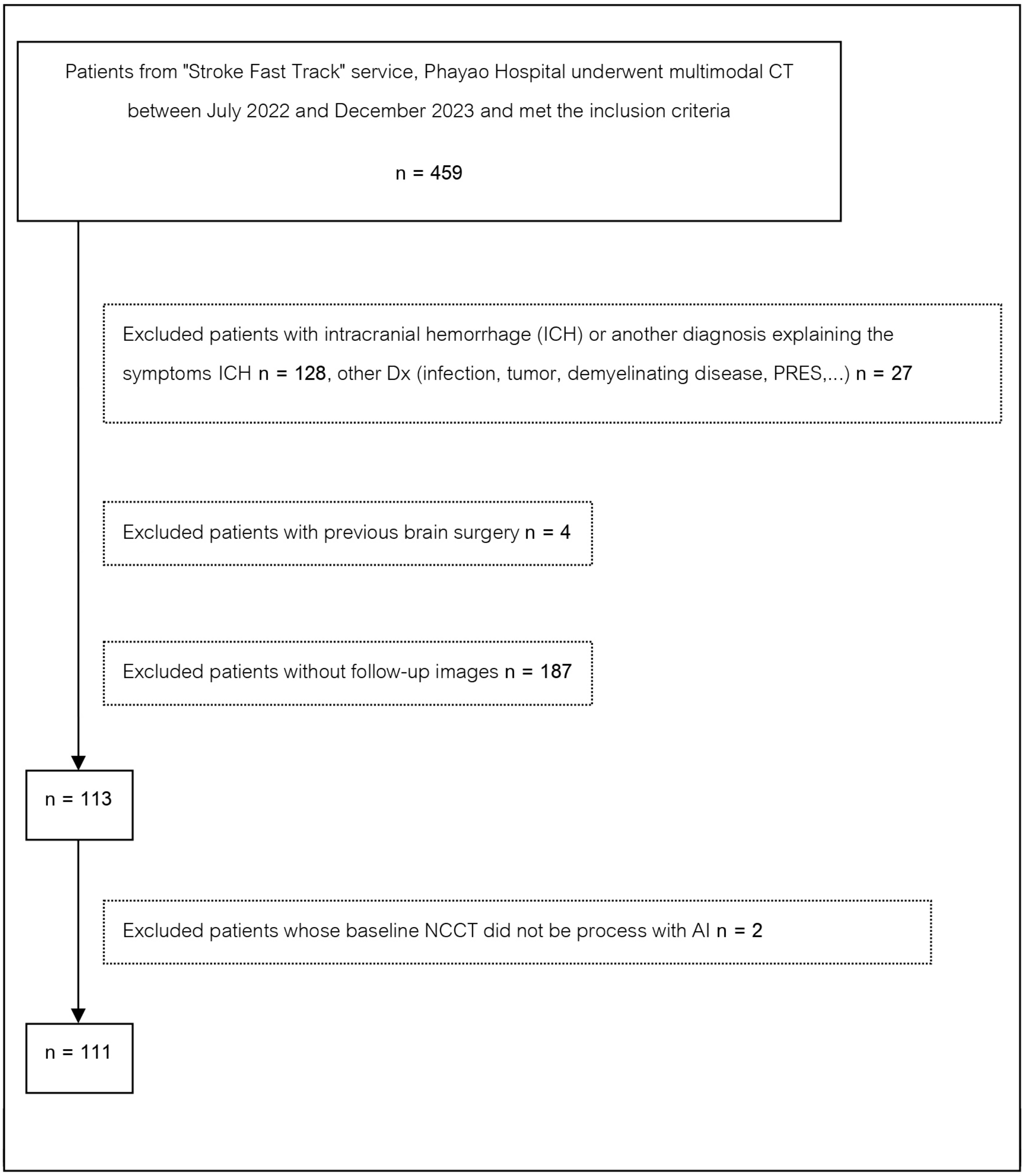

Figure 1. *Flowchart of patients included in the study.*

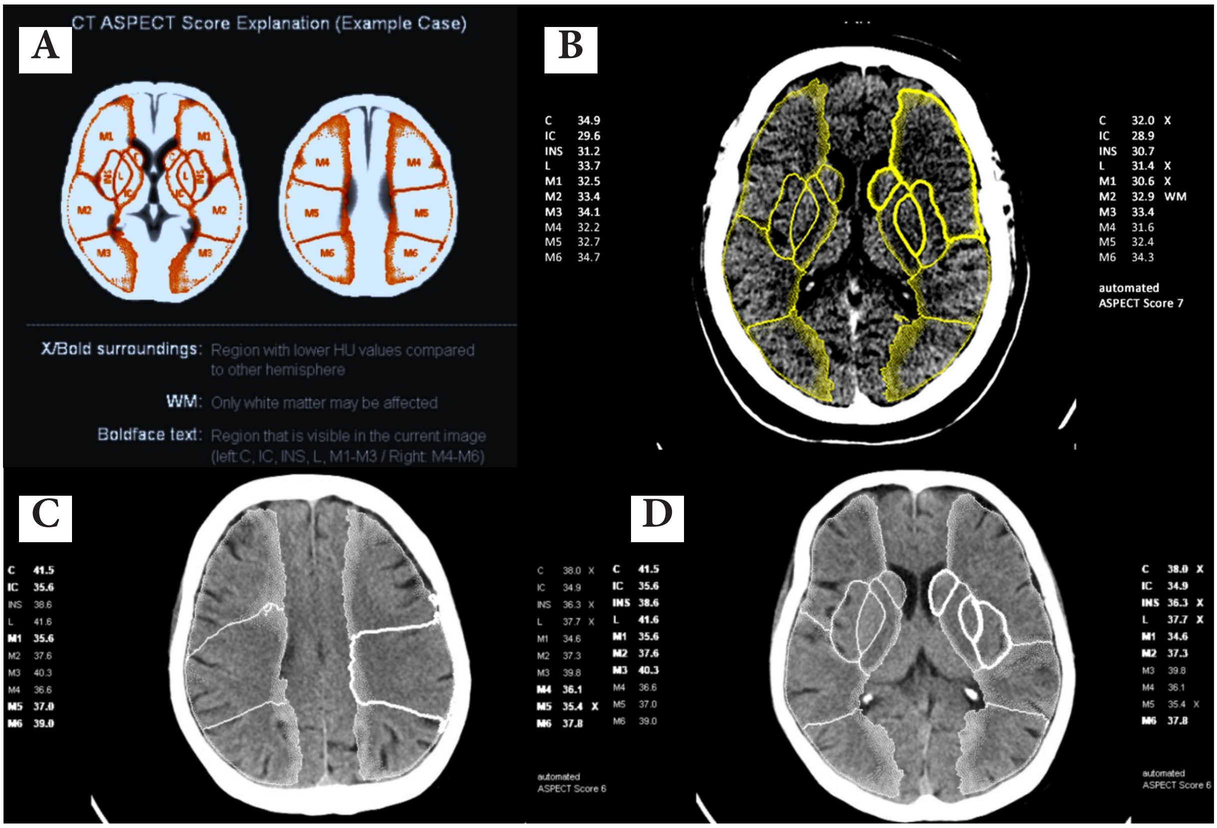

Figure 2. *(A) Example of CT-ASPECT score explanation in the automated software, showing the outlines of ten ASPECTS regions as an overlay on the axial NCCT images based on a quantitative topographic comparison of the left and right hemispheres. (B) Example of axial NCCT images with automatically computed EIC regions calculated with automatic software; the affected hemisphere is automatically selected by the software on the left side. The three affected regions are marked with X. Bold text indicates regions that are visible in the slice image (both hemispheres). Regions marked with WM, white matter, may be affected (are not used to calculate the ASPECTS). The automatically calculated ASPECTS (below the affected hemisphere) was 7. (C and D) Axial NCCT images of the same patient show areas with automatically calculated EIC, visualized within an overlaid white line using automated software. Bold text indicates regions visible in the different slices (both hemispheres). The automatically calculated ASPECTS was 6 in the left cerebral hemisphere. ASPECT scores were based on standard NCCT in the Picture Archiving and Communication System.*

To calculate the ASPECTS, 1 point is subtracted from 10 for each detection of an EIC for each of the 10 defined middle cerebral artery (MCA) vascular territories. C = caudate, IC = internal capsule, INS = insula, L = lentiform nucleus, M1 = frontal operculum, M2 = anterior temporal lobe, M3 = posterior temporal lobe, M4 = anterior MCA, M5 = lateral MCA, M6 = posterior MCA.

Results

General information

Finally, 111 patients were identified retrospectively. Their mean age was 67.8 years (±11.9 years), and 56 (50.5%) were female. The mean NIHSS (National Institute of Health Stroke Scale) score at the presentation was 14.2 (±8.8). Baseline NCCT was performed on average 123.9 minutes after the symptom onset or last seen normal. The clinical characteristics are summarized in Table 1.

Table 1. *Clinical characteristics of the study population.*

Characteristics	N (%) or Mean ± standard deviation
No. of patients	111
Age (years)	67.8 (±11.9)
Gender	
Male	55 (49.5)
Female	56 (50.5)
National Institute of Health Stroke Scale (NIHSS) score at presentation	14.2 (±8.8)
Time from symptom onset to baseline NCCT (minutes)	123.9 (±58.7)
Side of neurological symptoms	
Right	62 (55.9)
Left	49 (44.1)

ASPECTS region analysis

The affected cerebral hemisphere in the automated software, observer 1 and observer 2 matched the reference in 53%, 97%, and 57% of the patients, respectively. Nine of the 52 misclassifications in the automated software involved a unilateral cerebral hemisphere and sixteen involved a bilateral cerebral hemisphere. These patients had an unusual brain anatomy; thus, the registration could be incorrect, such as asymmetric ventricle sizes, old infarcts, and asymmetric brain atrophy. Examples of NCCT scans are shown in Figure 3. The remaining scans (27) were classified as normal. Three of the 3 misclassifications in observer1 were classified as normal. Two of the 48 misclassifications in observer 2 were clinically reported on the wrong side of the neurologic symptom at the time of presentation. The remaining scans (46) were classified as normal.

For all ASPECTS regions, observer 1 (radiologist with stroke window setting) showed higher positive percent agreement (PPA) than observer 2 (radiologists on service) and the automated software. However, the performance was slightly lower in the internal capsule, M3, and M6 regions. In the lentiform nucleus and M3, the automated software showed a tendency towards higher PPA and NPA than observer 2. In the caudate, the automated software showed a tendency towards higher PPA, but lower NPA than observer 2. In the internal capsule, M2, M4, and M5, the automated software showed a tendency towards lower PPA, but higher NPA than observer 2. In the insula and M6, the automated software showed a tendency towards lower PPA and NPA than observer 2. In M1, the automated software showed a tendency towards lower PPA but similar NPA compared to observer 2. In the internal capsule, M3 and M6, the automated software and two observers showed a tendency towards low PPA but high NPA. The regions with the lowest PPA of observer 1, observer 2, and the automated software were the internal capsule (61%), M3 (11.8%), and the internal capsule (10.2%), respectively. The full results are shown in Table 2.

For the agreement per region, observer 1 showed the highest agreement with the reference at M1 (0.94; almost perfect agreement) and the lowest agreement at M3 (0.07; slight agreement). The automated software showed the highest agreement with the reference at caudate (0.50; moderate agreement) and the lowest agreement at M1 (0.05; slight agreement). Observer 2 showed the highest agreement with the reference at M1 (0.35; fair agreement) and the lowest agreement at M3 (0.09; slight agreement). The highest agreement between the automated software and observer 1 was at caudate (0.59; moderate agreement) and the lowest agreement was at M4 (0.06; slight agreement). The highest agreement between the automated software and observer 2 was at lentiform nucleus (0.28; fair agreement) and the lowest agreement was at M6 (-0.02; poor agreement). The highest agreement between observer 1 and observer 2 was at M2 (0.40; fair agreement) and the lowest agreement was at M3 (0.11; slight agreement). The automated software showed a tendency towards higher agreement with the reference and two observers in deep/central regions than cortical regions (slight agreement to moderate agreement in deep/central regions and poor agreement to fair agreement in cortical regions). The regions showed the highest level of overall interobserver agreement were caudate and lentiform nucleus (fair agreement to almost perfect agreement). The region showed the lowest level of overall interobserver agreement was M3 (slight agreement to fair agreement). The complete results are shown in Table 3.

Table 2. *Diagnostic performance of the two observers and automated software for each individual ASPECTS region; the positive percent agreement (PPA) and negative percent agreement (NPA).*

Regions	Positive percent agreement (PPA) % (95% CI)	Negative percent agreement (NPA) % (95% CI)
Deep/Central regions		
Caudate (C)		
observer 1	81.1 (68.6-89.4%)	100.0 (93.8-100.0%)
observer 2	26.4 (16.4-39.6%)	96.6 (88.3-99.1%)
automated software	69.8 (56.5-80.4%)	79.3 (67.2-87.8%)
Internal Capsule (IC)		
observer 1	61.0 (48.3-72.4%)	96.2 (87.0-98.9%)
observer 2	16.9 (9.5-28.5%)	96.2 (87.0-98.9%)
automated software	10.2 (4.7-20.5%)	98.1 (89.9-99.7%)
Insula (INS)		
observer 1	94.4 (86.4-97.8%)	82.5 (68.1-91.3%)
observer 2	40.8 (30.2-52.5%)	97.5 (87.1-99.6%)
automated software	36.6 (26.4-48.2%)	92.5 (80.1-97.4%)
Lentiform nucleus (L)		
observer 1	89.7 (80.2-94.9%)	95.3 (84.5-98.7%)
observer 2	32.4 (22.4-44.2%)	95.3 (84.5-98.7%)
automated software	42.6 (31.6-54.5%)	100.0 (91.8-100.0%)

Cortical regions		
M1		
observer 1	95.5 (84.9-98.7%)	98.5 (92.0-99.7%)
observer 2	40.9 (27.7-55.6%)	91.0 (81.8-95.8%)
automated software	13.6 (6.4-23.8%)	91.0 (81.8-95.8%)
M2		
observer 1	84.9 (73.0-92.2%)	93.1 (83.6-97.3%)
observer 2	39.6 (27.6-53.1%)	91.4 (81.4-96.3%)
automated software	13.2 (6.5-24.8%)	100.0 (93.8-100.0%)
M3		
observer 1	70.6 (46.9-86.7%)	96.8 (91.0-98.9%)
observer 2	11.8 (3.3-34.3%)	94.7 (88.2-97.7%)
automated software	29.4 (13.3-53.1%)	96.8 (91.0-98.9%)
M4		
observer 1	89.5 (78.9-95.1%)	87.0 (75.6-93.6%)
observer 2	35.1 (24.0-48.1%)	85.2 (73.4-92.3%)
automated software	19.3 (11.1-31.3%)	90.7 (80.1-96.0%)
M5		
observer 1	89.2 (79.4-94.7%)	91.3 (79.7-96.6%)
observer 2	33.8 (23.5-46.0%)	87.0 (74.3-93.9%)
automated software	20.0 (12.1-31.3%)	97.8 (88.7-99.6%)
M6		
observer 1	63.0 (44.2-78.5%)	95.2 (88.4-98.1%)
observer 2	22.2 (10.6-40.8%)	92.9 (85.3-96.7%)
automated software	14.8 (5.92-32.5%)	91.7 (83.8-96.0%)

Table 3. *Agreement comparison of each individual ASPECTS region between observer 1, observer 2, automated software and reference.*

Regions	Cohen's kappa (95% CI)					
	Software vs. Reference	Software vs. Observer 1	Software vs. Observer 2	Observer 1 vs. Reference	Observer 2 vs. Reference	Observer 1 vs. Observer 2
Deep/Central regions						
Caudate (C)	0.50 (0.33-0.65)	0.59 (0.44-0.74)	0.23 (0.09-0.38)	0.82 (0.71-0.92)	0.24 (0.10-0.37)	0.34 (0.18-0.49)
Internal Capsule (IC)	0.08 (0.00-0.16)	0.18 (0.04-0.32)	0.14 (-0.11-0.40)	0.56 (0.42-0.70)	0.12 (0.02-0.23)	0.33 (0.16-0.50)
Insula (INS)	0.24 (0.11-0.36)	0.18 (0.06-0.30)	0.15 (-0.05-0.34)	0.78 (0.66-0.90)	0.31 (0.19-0.44)	0.25 (0.13-0.37)
Lentiform nucleus (L)	0.34 (0.24-0.49)	0.43 (0.30-0.56)	0.28 (0.08-0.48)	0.83 (0.73-0.94)	0.23 (0.11-0.35)	0.21 (0.08-0.35)
Cortical regions						
M1	0.05 (-.0.08-0.19)	0.10 (-0.04-0.25)	0.09 (-0.10-0.29)	0.94 (0.88-1.00)	0.35 (0.18-0.52)	0.36 (0.19-0.53)
M2	0.14 (0.04-0.23)	0.16 (0.05-0.27)	0.16 (-0.02-0.35)	0.78 (0.67-0.90)	0.32 (0.16-0.47)	0.40 (0.25-0.56)
M3	0.34 (0.08-0.59)	0.38 (0.11-0.64)	0.07 (-0.17-0.32)	0.07 (-0.07-0.09)	0.09 (-0.12-0.29)	0.11 (-0.11-0.33)
M4	0.10 (-0.02-0.23)	0.06 (-0.07-0.18)	0.22 (0.02-0.42)	0.77 (0.65-0.89)	0.20 (0.04-0.36)	0.26 (0.11-0.41)
M5	0.15 (0.06-0.25)	0.21 (0.10-0.31)	0.08 (-0.10-0,27)	0.80 (0.68-0.91)	0.19 (0.05-0.33)	0.22 (0.07-0.36)
M6	0.08 (-0.10-0.26)	0.07 (-0.13-0.26)	-0.02 (-0.19-0.16)	0.63 (0.45-0.80)	0.19 (-0.01-0.38)	0.12 (-0.09-0.33)

ASPECT score analysis
In the score analysis, the mean (±SD) and range of ASPECTS scores of the reference, observer 1, observer 2, and automated software were 5.37 (±3.0) and 0-10, 5.79 (±2.7) and 0-10, 8.14 (±2.8) and 0-10, and 8.36 (±1.7) and 2-10, respectively.

For dichotomized ASPECTS (≥6 and <6), the misclassifications (false high ASPECTS; underestimation) for observer 1, observer 2, and the automated software were eight out of 70, thirty-five out of 94, and forty-one out of 104, respectively. The misclassifications (false low ASPECTS; overestimation) for observer 1, observer 2, and the automated software were one out of 41, four out of 17, and 0 out of 7, respectively.

The PPA and NPA of the observer 1 were 83.3% and 98.4%, respectively. The PPA and NPA of the observer 2 were 27.1% and 93.7% respectively. The PPA and NPA of the automated software were 14.6% and 100.0% respectively. Observer 1 showed higher PPA than observer 2 and the automated software. However, observer 1 showed a tendency towards lower NPA than the automated software. The automated software also showed a tendency towards lower PPA but higher NPA than observer 2. The complete results are shown in Table 4.

For dichotomized ASPECTS (≥6 and <6), the agreement between the reference and observer 1 was 0.83, indicating almost perfect agreement. Levels of agreement between the reference and the automated software as well as observer 1 and the automated software were both 0.16, indicating slight agreement. Levels of the agreement between observer 2 and the reference, observer 1 and the automated software were 0.23, 0.21, and 0.27, indicating fair agreement. The complete results are shown in Table 5.

The agreement of the overall ASPECTS between the reference and observer 1 was greater than 0.90, indicating excellent agreement. The agreement of the overall ASPECTS between the reference and the automated software as well as observer 1 and the automated software were between 0.5 and 0.75 (ICC 0.545), indicating moderate agreement. The agreements of the overall ASPECTS between observer 2 and the reference, observer 1 and the automated software were all below 0.5, indicating poor agreement. The complete results are shown in Table 6.

Table 4. *Diagnostic performance of the two observers and automated software for dichotomized ASPECTS; the positive percent agreement (PPA) and negative percent agreement (NPA).*

Dichotomized ASPECTS ≥6 and <6	Positive percent agreement (PPA) % (95% CI)	Negative percent agreement (NPA) % (95% CI)
observer 1	83.3 (69.8-92.5%)	98.4 (91.5-99.9%)
observer 2	27.1 (15.3-41.9%)	93.7 (84.5-98.2%)
automated software	14.6 (6.1-27.8%)	100.0 (94.3-100.0%)

Table 5. *Agreement comparison of dichotomized ASPECTS between observer 1, observer 2, automated software and reference.*

	Cohen's kappa (95% CI)					
	Software vs. Reference	Software vs. Observer 1	Software vs. Observer 2	Observer 1 vs. Reference	Observer 2 vs. Reference	Observer 1 vs. Observer 2
Dichotomized ASPECTS ≥6 and <6	0.16 (0.05-0.27)	0.16 (0.03-0.29)	0.27 (0.02-0.52)	0.83 (0.73-0.94)	0.23 (0.07-0.37)	0.21 (0.04-0.38)

Table 6. *Agreement of total ASPECTS between observer 1, observer 2, automated software and reference.*

	With reference ICC (95% CI)	With observer 1 ICC (95% CI)	With observer 2 ICC (95% CI)	With automated software ICC (95% CI)
Observer 1	0.932 (0.902-0.953)		0.422 (0.256-0.564)	0.545 (0.399-0.664)
Observer 2	0.349 (0.174-0.503)	0.422 (0.256-0.564)		0.301 (0.121-0.462)
Automated software	0.545 (0.399-0.664)	0.545 (0.399-0.664)	0.301 (0.121-0.462)	

ICC, Intraclass correlation coefficient

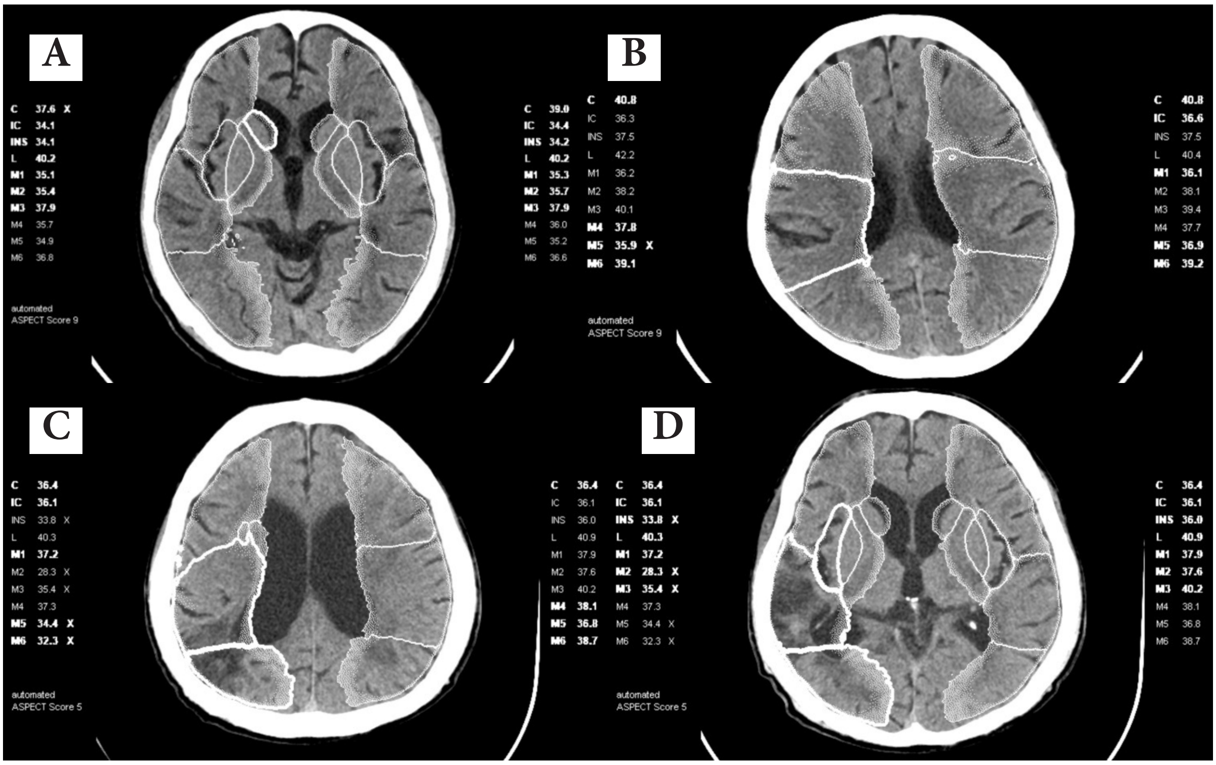

Figure 3. *Example of NCCT scans with unusual brain anatomy leading to misclassification of the affected hemisphere.*

(A) Asymmetric size of bilateral lateral ventricles - the right lateral ventricle was slightly larger than the left lateral ventricle, leading to a false positive result in the right caudate. The final reference for EIC was the left insula (ASPECTS = 9).

(B) Asymmetric gyral atrophy - prominent right frontoparietal sulci, leading to a false positive result at the right M5. The final reference for EIC was at the left insula, left lentiform nucleus, left M4 and left M5 (ASPECTS = 6).

(C and D) Old infarcts in the same patient - chronological change of late subacute infarcts in the right parieto-occipital lobe, leading to false positive findings in M2, M3, M5 and M6 of the right cerebral hemisphere. Prominent sulci of the right insula, leading to a false positive result in the right insula. The final reference for EIC was the left internal capsule (ASPECTS = 9).

Discussion

This study evaluated the performance of the automated ASPECTS software for the detection of EIC on the NCCT of the brain. This study showed moderate agreement between the automated software and the reference for total ASPECTS and slight agreement between the automated software and the reference for dichotomized ASPECTS (≥6 and <6). The agreement was similar to the agreement between the automated software and an individual reader (the observer 1).

The automated ASPECTS software has several advantages. The software can exclude voxels that are either too dark or too bright from the calculation before evaluating the mean density of the ASPECTS regions. Excluding these voxels, such as bone, calcifications, CSF or old brain infarcts, improves the accuracy of brain parenchymal density measurements. Automated software can automatically create the lines that divide the MCA territory into ten regions of interest based on quantitative topography as an overlay on each axial image of the NCCT. These lines for the boundary of each ASPECTS region appear when scrolling the NCCT, even if the window settings are changed. Originally, the ASPECTS was calculated within two predefined slices through the level of the basal ganglia and level of the supra-ganglionic structures [15], while several automated software programs now integrate the whole brain scan. These highlighted lines as an overlay on the NCCT could help in the visual evaluation of the NCCT to detect and quantify EIC. The drawback is the discrepancy in the assessment of the affected hemisphere in patients with an unusual brain anatomy is too large to affect the calculation of the average HU in each ASPECTS region, or the HU is not dark enough to be excluded before calculating the average HU. Two studies using other automated software have shown that brain atrophy and atypical brains affect the segmentation accuracy of each ASPECTS region [29, 30]. In this study, the latter cannot be corrected manually, which leads to an incorrect assessment of the ASPECTS.

Of note, the underestimation of dichotomized ASPECTS by the automated software totaled forty-one of 104, thirty-five of 94 by observer 2 (radiologists on service), and eight of 70 by observer 1 (radiologist with stroke window setting).

The underestimation of ASPECTS was probably caused by the limited calculation of the average HU in each ASPECTS region. Probable causes included changes so subtle or areas so small that they could not affect the calculation of the average HU, and the assessment of cortical regions based mainly on gray matter. On the other hand, the automated software found no overestimation compared to the two observers (one out of 41 by observer 1 and four out of 17 by observer 2). Therefore, if the automated ASPECTS are less than 6, an NCCT should be reviewed. If the NCCT shows no unusual brain anatomy, the findings could be true positives.

The relatively poor positive percent agreement (PPA) for dichotomized ASPECTS and poor agreement for total ASPECTS of observer 2 in this study could be partly explained by a pool of multiple radiologists, as almost all radiologists were teleradiologists. The teleradiologists received the clinical information from clinicians. The interpretation of NCCT by individual radiologists in the diagnosis of AIS might be affected by various practical conditions and limitations. The possible causes included: 1) analyzing the imaging information took time (the report production time for the stroke fast-track at Phayao Hospital was within 30 minutes of examination of the NCCT), 2) not all radiologists were trained to analyze and interpret the ASPECTS, resulting in varying levels of imaging expertise, 3) quantitative measurements of acute infarction on the NCCT were difficult in a routine clinical practice because the signs of infarction were more subtle and human judgment was highly variable. 4) there were some cases where teleradiologists were told the wrong side of the neurological symptoms on presentation, leading to incorrect classifications. The correct NCCT interpretation of a patient with an AIS prior to thrombolysis or MT therefore requires training and experience. Nevertheless, their results were recorded for analysis, which corresponded to the actual situation.

The underestimation of dichotomized ASPECTS by observer 2 with a total of thirty-five out of 94 was compared to eight out of 70 by observer 1. Eight patients received the wrong side of neurological symptoms at the time of presentation. Two out of eight were classified the wrong affected cerebral hemisphere on the NCCT and the remaining six were classified as normal. Four of these eight patients were underestimated. One of the two patients with underestimation missed the hyperdense clot in the proximal middle cerebral artery (MCA). In addition, observer 2 missed the hyperdense MCA sign on the NCCT in a total of twenty-five out of 58 patients. The hyperdense MCA signs were also recorded in the reference. The automated software in this study cannot evaluate this sign. The hyperdense vessel sign (HDVS) on the NCCT is an early marker for AIS caused by occlusion of the intracranial artery. HDVS is most commonly reported in the MCA region, as the MCA territory is usually the brain region most affected by an ischemic stroke [31]. Several studies concluded that HDVS has a high specificity and a high sensitivity for detecting LVO on the NCCT in AIS patients [32-35] with an NIHSS of more than 10 and suspected MCA occlusion (M1 segment) [33]. The density of the pathologic MCA should be more than 43 HU and 1.2 times higher than the contralateral MCA [35]. Due to its early visibility and before the appearance of pathological ischemic changes of the parenchyma, it represents a diagnostic aid in time-critical acute strokes. Automating the process of detecting MCA or intracranial HDVS signs in emergency imaging could speed up the identification of positive cases, especially in centers without regular access to CTA or MRI. This could shorten the time to execute acute treatment such as systemic thrombolysis or MT. Takahashi et al. published a study in 2013 on automated software to detect the HDVS sign on CT [24]. Considering the ongoing improvement of this automated software in the future, the detection of hyperdense MCA signs using HU is needed to improve diagnostic accuracy. However, the correct side of neurological symptoms at the time of presentation from the physician is very important for diagnostic imaging in patients with acute stroke, especially in AIS which shows rather subtle changes in density on the initial NCCT.

In this study, the performance was analyzed for each ASPECTS region. When analyzing the ASPECTS regions, the automated software and observer 2 showed greater differences in PPA than in negative percent agreement (NPA) for the detection of EIC in both cortical and deep regions. The automated software and the observer 2 showed low PPA but high NPA for the detection of EIC in all ASPECTS regions. However, the automated software and the observer 2 did not perform higher PPA than the observer 1 in detecting EIC in all ASPECTS regions.

For the internal capsule (IC), M3, and M6, two observers and the automated software showed lower PPA than the other regions, especially for IC. The remaining regions evaluated by observer 1 showed high PPA and NPA. The automated software showed a tendency towards higher agreement with the reference and the two observers in deep/central regions than cortical regions. The regions showed the highest level of overall interobserver agreement was caudate and lentiform nucleus (gray matter). The regions showed the lowest level of overall interobserver agreement was M3 and M6 (white matter). IC is a white matter and has a small volume and an indistinct boundary, which makes it difficult for humans to recognize the hypodensity and makes the outline of the ASPECTS region inappropriate for the automated software. M3 and M6, as well as the other cortical regions, are limited for EIC detection in the NCCT due to their subtle hypodensity [36]. It is difficult for automated software to precisely outline cortical regions. Furthermore, the average HU value in automated software is mainly based on gray matter. In regions M1 to M6, white matter may be affected in the regions labeled WM, but this is not taken into account in the automated ASPECTS calculation, resulting in an underestimation. In caudate, the automated software showed significantly higher PPA but lower NPA compared to observer 2. From these results, it appeared that the automated software had the highest PPA in caudate, while the overall NPA was good. The fluctuations in the results of the automated software and of observer 2 could be due to an inconsistent definition of the region boundaries [37, 38]. The automated software applied a standardized atlas method to outline ASPECTS regions based on a quantitative topographic comparison of the left and right cerebral hemisphere. Brain atrophy and an unusual brain anatomy also affected segmentation accuracy [29, 30], not only the ASPECTS calculation. Previous studies with other automated ASPECTS software showed variability in the characteristics of the regions scored [36-38]. Even if the automated segmentation of the ASPECTS region was not very precise, the high performance of observer 1 could improve the diagnostic accuracy in this situation. A combination of automated overlay of ASPECTS regions on NCCT images and stroke window settings is recommended for EIC detection. They show that the automated software overlays the boundaries of the regions in real time to detect subtle hypodensity in the same axial NCCT. However, future studies are needed to investigate the ASPECTS segmentation accuracy of the automated software.

Another problem in the evaluation of automated software is the choice of reference standard. The reference standard has a direct impact on the accuracy of the ASPECTS assessment. The reference standard used to assess the accuracy and reliability of automated ASPECTS software has varied in previous studies [38-49]. Conclusions may vary based on the reference standard used. Due to the subtle changes in the AIS, using the expert consensus score from the baseline NCCT as the reference standard may lead to an overestimation of the ASPECTS score [45-47]. Due to the time delay between the baseline NCCT examination and reperfusion, the ASPECTS, which was determined using follow-up images as a reference standard, may be underestimated [37, 48, 49]. To define the most accurate reference standard for the ASPECTS, it is advisable to use the baseline of the NCCT and the follow-up images [38, 39, 41-45]. This is consistent with this study, in which all available NCCT baseline examinations, NCCT follow-up examinations and/or CTA and digital subtraction angiography (DSA) were used for assessment. However, both the reference and the blinded ASPECTS assessment analysis (the observer 1) were performed by the same reader at different time points. To minimize a possible mutual influence of the two analysis runs, a long interval (eight weeks) was chosen between the blinded ASPECTS assessment analysis (observer 1) and the reference so that the reader could no longer remember the original measurement. In addition, sensitivity and specificity implied that the new test was compared to the truth or gold standard. Even though the concisely available reference was established, the reference in this study was not definitely proven the gold standard. Instead, the term of PPA, NPA and agreement were used.

There are only a few studies in which the automated software from Siemens Healthineers has been tested. The first study was published by Goebel J et al. comparing the performance of syngo.via Frontier ASPECTS Prototype V1.2.0 with the e-ASPECTS software [50]. The authors found high agreement in ASPECTS grading between two board-certified radiologists, i.e. consensus reading of NCCT images by experts, and e-ASPECTS. However, it showed only low to moderate agreement to Frontier- ASPECTS by Siemens. The second study was published by Hoelter P et al. evaluating three fully automated software applications for ASPECTS (Syngo.via Frontier ASPECT Score Prototype V2, Brainomix e-ASPECTS® and RAPID ASPECTS) in AIS patients [51]. The authors found a high correlation between the expert and three software programs. The highest correlation was between the expert and Brainomix (r = 0.871 (0.818, 0.909), $p < 0.001$), followed by the correlation between the expert and Frontier V2 (r = 0.801 (0.719, 0.859), $p < 0.001$) and between the expert and RAPID (r = 0.777 (0.568, 0.871), $p < 0.001$). There was a high correlation between the software tools (Frontier V2 and Brainomix: r = 0.830 (0.760, 0.880), $p < 0.001$; Frontier V2 and RAPID: r = 0.847 (0.693, 0.913), $p < 0.001$; Brainomix and RAPID: r = 0.835 (0.512, 0.923), $p < 0.001$). The third study was published by Wolff L et al. who evaluated the syngo.via Frontier ASPECTS Prototype V2.0.1 [42]. The authors found that the performance of the automated ASPECTS was comparable to that of experts and could assist readers in the detection of EIC. The automated ASPECTS post-processing software in this study was developed based on Syngo via Frontier ASPECTS Prototype for commercial use. Despite the fact that there are many studies on the use of the automated ASPECTS software, each automated software may lead to different diagnostic results, but no study investigated the Recon&GO Inline ASPECTS software. Further studies are needed to compare the performance of this commercial version of the software with that of other software.

Some studies that used automated software to analyze the ASPECTS score level showed similar results. Temmen SE, et al. found that the performance of the automated software as Canon medical system base version 1.3 for LVO detection was lower than that of the radiologist in 100 patients [44]. Sawicki M, et al. found that the performance of e-CTA (a part of e-STROKE, version 10.1p3, Brainomix Ltd.) was acceptable for the detection of proximal LVOs in 108 patients, while it did not seem to be accurate enough for distal LVOs compared to the neuroradiologist [41].

Studies have used other automated software for ASPECTS analysis at the regional level that come to similar results. Austein F, et al. found moderate agreement between two automated software packages and expert consensus for overall ASPECTS in 52 patients and no significant difference in the overall performance. However, the software packages differed in terms of regional contribution. Package

A was more sensitive in cortical areas than the other methods but at the expense of specificity. Expert consensus and software package B had higher sensitivity but lower specificity for deep brain structures. The variability of results at the region level may be due to inconsistent definitions of region boundaries, especially for IC and M4-6 [37]. Chen Z, et al, evaluated two automated ASPECTS software (The RAPID (iSchemaView, software version 5.0) and NBC (NeuBrainCARE software version 1.0)) compared to radiologists in 276 patients. The authors found greater differences in sensitivity than in specificity and accuracy. NBC showed higher specificity and lower sensitivity, while RAPID showed lower specificity and higher sensitivity for detecting EIC in deep regions. NBC showed lower specificity and higher sensitivity, while RAPID showed higher specificity and lower sensitivity for the detection of EIC in cortical regions. NBC and RAPID did not perform better than experienced radiologists in detecting EIC in cortical regions [38]. Future studies are needed to investigate the ASPECTS segmentation accuracy of the automated software. In addition, further studies are needed to evaluate the time dependence of the ASPECTS analysis at the regional level.

There are several limitations to this study. First, it was a retrospective study collected from the Radiologic Information System and the Picture Archiving and Communication System. Second, the study group was rather small. Third, this study used imaging data from a single center to test only one vendor-specific AI software. Fourth, this study used the assessment of a single reader as a reference and individual observer. Fifth, the time interval between the baseline NCCT and the follow-up images varied within a week. Sixth, there were different times for interpreting the ASPECTS between the two observers in which observer 2 limited the time to 30 minutes, while the observer 1 did not limit the time for interpreting the NCCT.

Conclusion

This study aimed to evaluate the agreement with radiologists of an AI-based automated post-processing software for the detection of EIC and the calculation of ASPECTS on NCCT images in AIS patients. The study results showed that the tested AI software had lower agreement for the total ASPECTS than the radiologist-determined observer 1 when using the stroke window on the NCCT, but better than a pool of radiologists on service. For dichotomized ASPECTS (≥6 and <6), the tested AI software showed perfect (100%) NPA. When analyzing the ASPECTS regions, there were different advantages for scoring the deep regions and the cortical regions. The tested AI software showed low PPA but rather high NPA with perfect (100%) NPA in lentiforn nucleus and M2. The tested AI software also showed higher agreement with the reference and two observers in deep/central regions than cortical regions. From the results, the tested AI software retained its potential for use in emergency situations, particularly for radiologists with limited experience and limited time to report. The high NPA of automated software on dichotomized ASPECTS can help provide immediate results. The future utility of the automated ASPECTS software can be used in conjunction with an experienced reader or radiologist on service to validate the final score and identify artifacts or technical issues that may lead to an over- or underestimation of the actual ASPECT score. Due to the high performance of the observer 1, an experienced reader or radiologist could use the automatically highlighted marker as an overlay on NCCT images from the automated software along with the stroke window setting during the interpretation of fast-track NCCT scans to improve the accuracy of EIC detection and ASPECTS calculation.

Funding: The author states that this work did not receive any financial support.

Institutional Review Board Statement: The study protocol was approved by the research ethics committee of Phayao Hospital (COA number 257). The informed consent was waived because of the retrospective study design.

Conflicts of Interest: The authors declare no conflict of interest.

References

1. Soun JE, Chow DS, Nagamine M, Takhtawala RS, Filippi CG, Yu W, et al. Artificial intelligence and acute stroke Imaging. AJNR Am J Neuroradiol 2021;42:2-11. doi: 10.3174/ajnr.A6883.

2. Boehme AK, Esenwa C, Elkind MS. Stroke risk factors, genetics, and prevention. Circ Res 2017;120:472-95. doi: 10.1161/CIRCRESAHA.116.308398.

3. Emberson J, Lees KR, Lyden P, Blackwell L, Albers G, Bluhmki E, et al. Effect of treatment delay, age, and stroke severity on the effects of intravenous thrombolysis with alteplase for acute ischaemic stroke: a meta-analysis of individual patient data from randomised trials. Lancet 2014;384:1929-35. doi: 10.1016/S0140-6736(14)60584-5.

4. Tiamkao S. [13 years - learning and development of Stroke Fast Track in Thailand]. J Health Syst Res 2023;17:191-99. Thai.

5. Berkhemer OA, Fransen PS, Beumer D, van den Berg LA, Lingsma HF, Yoo AJ, et al. A randomized trial of intraarterial treatment for acute ischemic stroke. N Engl J Med 2015;372:11-20. doi: 10.1056/NEJMoa1411587.

6. Campbell BC, Mitchell PJ, Kleinig TJ, Dewey HM, Churilov L, Yassi N, et al. Endovascular therapy for ischemic stroke with perfusion-imaging selection. N Engl J Med 2015;372:1009-18. doi: 10.1056/NEJMoa1414792.

7. Albers GW, Marks MP, Kemp S, Christensen S, Tsai JP, Ortega-Gutierrez S, et al. Thrombectomy for stroke at 6 to 16 hours with selection by perfusion imaging. N Engl J Med 2018;378:708–18. doi: 10.1056/NEJMoa1713973.

8. Saver JL, Goyal M, Bonafe A, Diener HC, Levy EI, Pereira VM, et al. Stent-retriever thrombectomy after intravenous t-PA vs. t-PA alone in stroke. N Engl J Med 2015;372:2285-95. doi: 10.1056/NEJMoa1415061.

9. Goyal M, Demchuk AM, Menon BK, Eesa M, Rempel JL, Thornton J, et al. Randomized assessment of rapid endovascular treatment of ischemic stroke. N Engl J Med 2015;372:1019-30. doi: 10.1056/NEJMoa1414905.

10. Jovin TG, Chamorro A, Cobo E, de Miquel MA, Molina CA, Rovira A, et al. Thrombectomy within 8 hours after symptom onset in ischemic stroke. N Engl J Med 2015;372:2296-306. doi: 10.1056/NEJMoa1503780.

11. Nogueira RG, Jadhav AP, Haussen DC, Bonafe A, Budzik RF, Bhuva P, et al. Thrombectomy 6 to 24 hours after stroke with a mismatch between deficit and Infarct. N Engl J Med 2018;378:11-21. doi: 10.1056/NEJMoa1706442.

12. Turc G, Bhogal P, Fischer U, Khatri P, Lobotesis K, Mazighi M, et al. European Stroke Organisation (ESO) - European Society for Minimally Invasive Neurological Therapy (ESMINT) guidelines on mechanical thrombectomy in acute ischemic stroke. J Neurointerv Surg 2023;15:e8. doi: 10.1136/neurintsurg-2018-014569.

13. Powers WJ, Rabinstein AA, Ackerson T, Adeoye OM, Bambakidis NC, Becker K, et al. Guidelines for the early management of patients with acute ischemic stroke: 2019 update to the 2018 guidelines for the early management of acute ischemic stroke: a guideline for healthcare professionals from the American Heart Association/American Stroke Association. Stroke 2019;50:e344-e418. doi: 10.1161/STR.0000000000000211.

14. Venema E, Mulder MJHL, Roozenbeek B, Broderick JP, Yeatts SD, Khatri P, et al. Selection of patients for intra-arterial treatment for acute ischaemic stroke: development and validation of a clinical decision tool in two randomized trials. BMJ 2017;357:j1710. doi: 10.1136/bmj.j1710.

15. Barber PA, Demchuk AM, Zhang J, Buchan AM. Validity and reliability of a quantitative computed tomography score in predicting outcome of hyperacute stroke before thrombolytic therapy. ASPECTS Study Group. Alberta Stroke Programmed Early CT Score. Lancet 2000;355:1670-4. doi: 10.1016/s0140-6736(00)02237-6.

16. Pexman JH, Barber PA, Hill MD, Sevick RJ, Demchuk AM, Hudon ME, et al. Use of the Alberta Stroke Program Early CT Score (ASPECTS) for assessing CT scans in patients with acute stroke. AJNR Am J Neuroradiol 2001;22:1534-42.

17. Prakkamakul S, Yoo AJ. ASPECTS CT in acute ischemia: review of current data. Top Magn Reson Imaging 2017;26:103-12. doi: 10.1097/RMR.0000000000000122.

18. Herweh C, Ringleb PA, Rauch G, Gerry S, Behrens L, Möhlenbruch M, et al. Performance of e-ASPECTS software in comparison to that of stroke physicians on assessing CT scans of acute ischemic stroke patients. Int J Stroke 2016;11:438-45. doi: 10.1177/1747493016632244.

19. Lee EJ, Kim YH, Kim N, Kang DW. Deep into the brain: artificial intelligence in stroke imaging. J Stroke 2017;19:277-85. doi: 10.5853/jos.2017.02054.

20. Mokli Y, Pfaff J, Dos Santos DP, Herweh C, Nagel S. Computer-aided imaging analysis in acute ischemic stroke – background and clinical applications. Neurol Res Pract 2019;1:23. doi: 10.1186/s42466-019-0028-y.

21. Tang FH, Ng DK, Chow DH. An image feature approach for computer-aided detection of ischemic stroke. Comput Biol Med 2011;41:529-36. doi: 10.1016/j.compbiomed.2011.05.001.

22. Chen L, Bentley P, Rueckert D. Fully Automatic Acute Ischemic Lesion Segmentation in DWI Using Convolutional Neural Networks. NeuroImage Clin 2017;15:633–43. doi: 10.1016/j.nicl.2017.06.016.

23. Kuang H, Najm M, Chakraborty D, Maraj N, Sohn SI, Goyal M, et al. Automated ASPECTS on noncontrast CT scans in patients with acute ischemic stroke using machine learning. AJNR Am J Neuroradiol 2019;40:33-8. doi: 10.3174/ajnr.A5889.

24. Takahashi N, Lee Y, Tsai DY, Matsuyama E, Kinoshita T, Ishii K. An automated detection method for the MCA dot sign of acute stroke in unenhanced CT. Radiol Phys Technol 2014;7:79-88. doi: 10.1007/s12194-013-0234-1.

25. Chen Y, Dhar R, Heitsch L, Ford A, Fernandez-Cadenas I, Carrera C, et al. Automated quantification of cerebral edema following hemispheric Infarction: Application of a machine-learning algorithm to evaluate CSF shifts on serial head CTs. NeuroImage Clin 2016;12:673–80. doi: 10.1016/j.nicl.2016.09.018.

26. Mainali S, Wahba M, Elijovich L. Detection of early ischemic changes in noncontrast CT head improved with "Stroke Windows". ISRN Neurosci 2014; 2014:654980. doi: 10.1155/2014/654980.

27. Landis JR, Koch GG. The measurement of Observer agreement for categorical data. Biomentrics 1977; 33:159-74.

28. Koo TK, Li MY. A guideline of selecting and reporting intraclass correlation coefficients for reliability research. J Chiropr Med 2016;15:155-63. doi: 10.1016/j.jcm.2016.02.012.

29. Shieh Y, Chang CH, Shieh M, Lee TH, Chang YJ, Wong HF, et al. Computer-aided diagnosis of hyperacute stroke with thrombolysis decision support using a contralateral comparative method of CT image analysis. J Digit Imaging 2014 ;27:392-406. doi: 10.1007/s10278-013-9672-x.

30. Stoel BC, Marquering HA, Staring M, Beenen LF, Slump CH, Roos YB, et al. Automated brain computed tomographic densitometry of early ischemic changes in acute stroke. J Med Imaging (Bellingham) 2015;2:014004. doi: 10.1117/1.JMI.2.1.014004.

31. Ng YS, Stein J, Ning M, Black-Schaffer RM. Comparison of clinical characteristics and functional outcomes of ischemic stroke in different vascular territories. Stroke 2007;38:2309-14. doi: 10.1161/STROKEAHA.106.475483.

32. Mair G, Boyd EV, Chappell FM, von Kummer R, Lindley RI, Sandercock P, et al. Sensitivity and specificity of the hyperdense artery sign for arterial obstruction in acute ischemic stroke. Stroke 2015;46:102-7. doi:10.1161/STROKEAHA.114.007036.

33. Lim J, Magarik JA, Froehler MT. The CT-defined hyperdense arterial sign as a marker for acute intracerebral large vessel occlusion. J Neuroimaging 2018;28: 212-6. doi: 10.1111/jon.12484.

34. Jensen-Kondering U, Riedel C, Jansen O. Hyperdense artery sign on computed tomography in acute ischemic stroke. World J Radiol 2010;2:354-7. doi: 10.4329/wjr.v2.i9.354.

35. Koo CK, Teasdale E, Muir KW. What constitutes a true hyperdense middle cerebral artery sign? Cerebrovasc Dis 2000;10:419-23. doi: 10.1159/000016101.

36. Chiang PL, Lin SY, Chen MH, Chen YS, Wang CK, Wu MC, et al. Deep learning-based automatic detection of ASPECTS in acute ischemic stroke: improving stroke assessment on CT scans. J Clin Med 2022;11:5159. doi: 10.3390/jcm11175159.

37. Austein F, Wodarg F, Jürgensen N, Huhndorf M, Meyne J, Lindner T, et al. Automated versus manual imaging assessment of early ischemic changes in acute stroke: comparison of two software packages and expert consensus. Eur Radiol 2019;29:6285-92. doi: 10.1007/s00330-019-06252-2.

38. Chen Z, Shi Z, Lu F, Li L, Li M, Wang S, et al. Validation of two automated ASPECTS software on non-contrast computed tomography scans of patients with acute ischemic stroke. Front Neurol 2023;14:1170955. doi: 10.3389/fneur.2023.1170955.

39. Neuhaus A, Seyedsaadat SM, Mihal D, Benson JC, Mark I, Kallmes DF, et al. Region-specific agreement in ASPECTS estimation between neuroradiologists and e-ASPECTS software. J Neurointerv Surg 2020;12:720-3. doi: 10.1136/neurintsurg-2019-015442.

40. Naganuma M, Tachibana A, Fuchigami T, Akahori S, Okumura S, Yi K, et al. Alberta Stroke Program Early CT Score calculation using the deep learning-based brain hemisphere comparison algorithm. J Stroke Cerebrovasc Dis 2021;30:105791. doi: 10.1016/j.jstrokecerebrovasdis.2021.105791.

41. Sawicki M, Safranow K, Wiska L, Pasek I, Gajdziel A, Gruszewski M, et al. Diagnostic value of artificial intelligence—based software in detection of large vessel occlusion in acute ischemic stroke. Appl Sci 2021;11:10017. https://doi.org/10.3390/app112110017.

42. Wolff L, Berkhemer OA, van Es ACGM, van Zwam WH, Dippel DWJ, Majoie CBLM, et al. Validation of automated Alberta Stroke Program Early CT Score (ASPECTS) software for detection of early ischemic changes on non-contrast brain CT scans. Neuroradiology 2021;63:491-8. doi: 10.1007/s00234-020-02533-6.

43. Maegerlein C, Fischer J, Mönch S, Berndt M, Wunderlich S, Seifert CL, et al. Automated calculation of the Alberta Stroke Program Early CT Score: feasibility and reliability. Radiology 2019;291:141-8. doi: 10.1148/radiol.2019181228.

44. Temmen SE, Becks MJ, Schalekamp S, van Leeuwen KG, Meijer FJA. Duration and accuracy of automated stroke CT workflow with AI-supported intracranial large vessel occlusion detection. Sci Rep 2023;13:12551. doi: 10.1038/s41598-023-39831-x.

45. Löffler MT, Sollmann N, Mönch S, Friedrich B, Zimmer C, Baum T, et al. Improved reliability of automated ASPECTS evaluation using iterative model reconstruction from head CT scans. J Neuroimaging 2021;31:341-7. doi: 10.1111/jon.12810.

46. McTaggart RA, Jovin TG, Lansberg MG, Mlynash M, Jayaraman MV, Choudhri OA, et al. Alberta stroke program early computed tomographic scoring performance in a series of patients undergoing computed tomography and MRI: reader agreement, modality agreement, and outcome prediction. Stroke 2015;46:407-12. doi: 10.1161/STROKEAHA.114.006564.

47. Kuang H, Najm M, Chakraborty D, Maraj N, Sohn SI, Goyal M, et al. Automated ASPECTS on noncontrast CT scans in patients with acute ischemic stroke using machine learning. AJNR Am J Neuroradiol 2019;40:33-8. doi: 10.3174/ajnr.A5889.

48. Nagel S, Sinha D, Day D, Reith W, Chapot R, Papanagiotou P, et al. e-ASPECTS software is non-inferior to neuroradiologists in applying the ASPECT score to computed tomography scans of acute ischemic stroke patients. Int J Stroke 2017;12:615-22. doi: 10.1177/1747493016681020.

49. Guberina N, Dietrich U, Radbruch A, Goebel J, Deuschl C, Ringelstein A, et al. Detection of early infarction signs with machine learning-based diagnosis by means of the Alberta Stroke Program Early CT score (ASPECTS) in the clinical routine. Neuroradiology 2018;60:889-901. doi: 10.1007/s00234-018-2066-5.

50. Goebel J, Stenzel E, Guberina N, Wanke I, Koehrmann M, Kleinschnitz C, et al. Automated ASPECT rating: comparison between the Frontier ASPECT Score software and the Brainomix software. Neuroradiology 2018;60:1267-72. doi: 10.1007/s00234-018-2098-x.

51. Hoelter P, Muehlen I, Goelitz P, Beuscher V, Schwab S, Doerfler A. Automated ASPECT scoring in acute ischemic stroke: comparison of three software tools. Neuroradiology 2020;62:1231-8. doi: 10.1007/s00234-020-02439-3.

Original Article

Clinical features and computed tomography (CT) findings in abdominal actinomycosis: A retrospective review

Thunsita Krailertmongkol, M.D.[(1)]
Kobkun Muangsomboon, M.D.[(1)]
Nithida Na Songkhla, M.D.[(1)]
Shanigarn Thiravit, M.D.[(1)]
Sorranart Muangsomboon, M.D.[(2)]
From [(1)]Division of Diagnostic Radiology, Department of Radiology,
[(2)]Department of Pathology, Faculty of Medicine Siriraj Hospital,
Mahidol University, Bangkok, Thailand.
Address correspondence to T.K. (email: mewthunsita@gmail.com)

Received 30 July 2024; revised 26 September 2024; accepted 12 December 2024
doi:10.46475/asean-jr.v25i3.922

Abstract

Background: Actinomycosis is a rare chronic disease that presents diagnostic challenges owing to its similarity to malignancies and other infections. An early diagnosis and an appropriate antibiotic therapy are crucial for effective treatment. Surgical intervention may be necessary to manage abscesses or remove infected tissues.

Objective: To study the characteristics observed in computed tomography (CT) scans and key symptoms presentation to aid in the diagnosis of abdominal actinomycosis. This aims to contribute to more precise decision-making in selecting appropriate and beneficial treatment approaches for patients.

Materials and Methods: A retrospective analysis of abdominopelvic actinomycosis cases (n=13) treated at Siriraj Hospital from January 2007 to June 2022 was conducted. Medical records, including clinical, pathological, microbiological, and therapeutic data, were analyzed comprehensively. The subjects underwent independent CT image interpretation by two experienced radiologists.

Results: CT findings, with abscess formation being predominant (n=8, 61.5%). Other findings included fistula tract formation (n=3, 23%), soft tissue mass mimicry (n=2, 15.3%), and presence of foreign bodies (n=4, 30.7%). The chief complaints prompting hospital visits included a palpable mass, abdominal pain, lower gastrointestinal tract bleeding, chronic diarrhea, and frequent urination.

Conclusion: Abdominal actinomycosis warrants consideration in the differential diagnosis of abdominal CT-detected masses and abscesses. Knowledge of CT features in actinomycosis infection, fistula formation, and retained foreign bodies in the lesion helps radiologists consider this infection in differential diagnosis and guides proper treatment planning.

Keywords: Abdominal actinomycosis, CT findings.

Introduction

Actinomycosis refers to a rare chronic disease caused by Actinomyces spp. Which are gram-positive filamentous non-acid fast anaerobic bacteria. These bacteria are typically part of the body's normal flora in regions such as the oral cavity, nasal cavity, intestines, and the genital tract They remain nonpathogenic [1, 2] unless infiltration into mucosal barrier and may result in a chronic infection characterized by proliferative tissue growth and abscess formation which can create a fistula tract to adjacent organs. Furthermore, there is a potential for extension into adjacent tissues, exhibiting characteristics resembling neoplastic masses or tumors, as evidenced by radiological imaging (tumor mimic) [1-3]. Additionally, hematogenous spread can lead to infections in distant areas, such as the lungs or liver. The most common etiologic organism of actinomycosis is Actinomyces israelii [1].

The primary objective was to study the characteristics observed on computed tomography (CT) scans and the key symptoms presented by patients upon hospital admission to aid in the accurate diagnosis of abdominal actinomycosis. This aim to increase awareness of this condition is essential for selecting appropriate and effective treatment strategies for patients.

Materials and methods

Patients

A retrospective analysis was performed on patients diagnosed with abdominopelvic actinomycosis who underwent surgical interventions between January 2007 to June 2022. Over this period included 13 cases that followed the research protocol and had completed the CT image and pathology result, comprising 4 males and 9 females. A thorough analysis of the medical records encompassed clinical, pathological, microbiological, and therapeutic data. This study was approved by the Siriraj Hospital board.

The inclusion criteria were as follows: 1. Patients were diagnosed with abdominal actinomycosis (abdominal organs, abdominal cavity or abdominal wall) at Siriraj Hospital 2. Patients aged ≥ 18 years.

Exclusion Criteria are 1. Patients without radiological imaging data in the PACS system at Siriraj Hospital. 2. The presence of abdominal actinomycosis was confirmed in patients without pathological or laboratory test results. 3. The time interval between the CT scan and tissue diagnosis of abdominal actinomycosis was more than 1 month.

Image interpretation

The CT images were retrospectively reviewed by two experienced body imaging radiologists. Radiological features analyzed included location, lesion size, heterogeneity of the lesion, border characteristics (smooth or irregular), enhancement pattern, abscess formation, fistula formation, or foreign body detection, extent and spread of lesions into adjacent tissues, quantification of white blood cells from blood test results, and surgical or treatment procedures undertaken to obtain the tissue specimen.

Results

The research gathered 22 patients diagnosed with abdominopelvic actinomycosis and excluded 9 patients who did not have pre-operative imaging in the PACS system. The study cohort of 13 patients with abdominopelvic actinomycosis, of which 4 were male and 9 were female (mean age, 52.3 year; range, 29-76 years.). The chief complaints initiating a visit to the hospital were palpable mass (n=3, 23.07%), flank pain (n=2, 15.38%), right upper quadrant pain (n=2, 15.38%), pelvic pain (n=2, 15.38%), lower gastrointestinal tract bleeding (n=2, 15.38%), chronic diarrhea (n=1, 7.69%) and frequent urination (n=1, 7.69%). The duration from development of symptoms to a hospital visit ranged from 1 week to 52 weeks, with an average of 11.92 ± 14.64 weeks (Table 1).

Table 1. *Demography and clinical characteristics of patients.*

	Age	Sex	Predisposing Factors	Presentation	Initial diagnosis	WBC (μL)	CT finding	Surgery/treatment	Duration of symptom (week)	Length of stays (day)
1	54	F	-	Right lower quadrant pain Palpable mass	Retroperitoneal mass (soft tissue sarcoma)	6590	- Retroperitoneal abscess and psoas muscle abscess	CT-guided percutaneous tissue biopsy Wide excision	32	6
2	76	F	Hypertension, intrahepatic duct stone	Right upper quadrant pain	Intrahepatic duct stone with left lobe atrophy	5700	- Intrahepatic duct stone with chronic cholangitis - left portal vein thrombosis	Left lateral segmentectomy	24	5
3	60	M	Diabetes Mellitus	Back pain Fever, Palpable mass	Emphysematous pyelonephritis	34960	- Emphysematous pyelonephritis with perinephric abscess involved psoas muscle, posterior pararenal space and posterior abdominal wall, multiple renal stone	Open drainage, left radical nephrec-tomy	2	36
4	29	F	Ulcerative colitis on steroid	Lower gastrointestinal bleeding, Chronic diarrhea	Ulcerative colitis	8900	- Diffuse colonic wall thickening with s ubmucosal deep ulcer	Total colectomy	52	12
5	60	F	-	Abdominal mass	TB ileum	11110	- Matted small bowel appearance at terminal ileum and IC valve	Ileocecal resection	2	10
6	58	F	Intrauterine device used	Pelvic pain, Vaginal bleeding	CA cervix	15510	- Left adnexal abscess with fistula tract to sigmoid colon	TAH with BSO with partial excision mass at cu de sac	8	7
7	75	F	Type2 Diabetes Mellitus, Hypertension	Frequent urination	Pelvic abscess	9800	- Pelvic abscess involve bladder and uterus with fistula tract to sigmoid colon	Sigmoidectomy	4	36
8	31	F	Endometriosis	Pelvic pain	Ovarian abscess	13850	Tubo-ovarian abscess	Excision	4	3
9	41	F	-	Abdominal wall mass	Abdominal wall mass	7870	Abdominal wall mass	Excision	2	2
10	48	F	Intrauterine device used	Pelvic pain	Left psoas abscess	12940	- Pelvic abscess involved psoas and iliopsoas muscle - fistula tract to p osterior abdominal wall	Percutaneous drainage	12	15
11	47	M	Congenital single left kidney	Left flank pain, Fever	Left renal mass	25300	- Multiloculated small abscess at left kidney extended involve adrenal gland, spleen, abdominal wall, pleural cavity.	Ultrasound guided biopsy	8	1
12	32	M	-	Lower gas-trointestinal bleeding	Appendiceal tumor and appendicitis	8000	Chronic appendicitis	Right hemicolectomy	1	6
13	69	M	Type2 Diabe-tes Mellitus	Right upper quadrant pain	Liver mass	10280	Liver abscess	Ultrasound guided biopsy and debridement	4	6

The result of laboratory test and pre-operative diagnosis according to blood chemistry tests, the mean numbers of WBC averaged 13,139.23/µL, which were slightly higher than normal (normal value; 4,000-10,000 /µL). An abdominal CT scan was performed on all patients, which detected either an intra-abdominal mass or abscess, and mimicking malignancy. Locations of the lesion were pelvic cavity (n =3), retroperitoneal space (n = 2), kidney (n = 2), liver (n =2), appendix (n =1), abdominal wall (n =1), colon (n = 1) and small bowel (n =1).

CT findings in the presented cases were predominantly centered on the formation of rim-enhancing abscesses, indicative of an ongoing infection and inflammatory process. Abscess formation being the most common, observed in 61.5% of cases (n=8). CT demonstrates an abnormally low attenuation area with surrounding rim enhancement, which might be an irregular, thick, or soft tissue mimic, mostly extending extensively into adjacent tissues.

Additionally, fistula tract formation was identified in 23% of the cases (n=3), underscoring the complex nature of actinomycosis-associated pathology. This presents as an abnormal connection between a complex abscess and adjacent organs or the skin, sometimes showing enhancement along the fistula tract.

Notably, only soft tissue mass presentation mimicry was noted in 15.3% of cases (n=2, in the liver and kidney), and actinomycosis infection was not included in the initial diagnosis owing to clinical features, complexity of the infection, soft tissue density mimic, and association with enhanced inflamed soft tissue. In addition, a small fistula tract may not be recognized. This was interpreted as a malignant tumor.

Furthermore, the foreign body related pattern, the presence of intrauterine device used in 2 cases (15.3%), renal stones in 1 case (7.6%) and intrahepatic duct stone in 1 case (7.6%) were notable. (Table 2). Pelvic abscesses were the most commonly observed manifestations. One notable case featured a left adnexal thick-wall abscess with a fistula tract extending to the sigmoid colon, with a noteworthy history of 30 years of intrauterine device use (Figure 1). Another case was a multiloculated irregular abscess involving the left pelvic cavity, psoas muscle, and iliopsoas with a fistula tract from the psoas muscle to the posterior abdominal wall with a history of 12 years of intrauterine device use (Figure 2).

Table 2. *The key CT findings in the study.*

CT Findings	Number of patients
Complex abscess formation	8 (61.5%)
Fistula tract	3 (23%)
Mass forming	2 (15.3%)
Intrauterine device used	2 (15.3%)
Renal stones	1 (7.6%)
Intrahepatic duct stones	1 (7.6%)

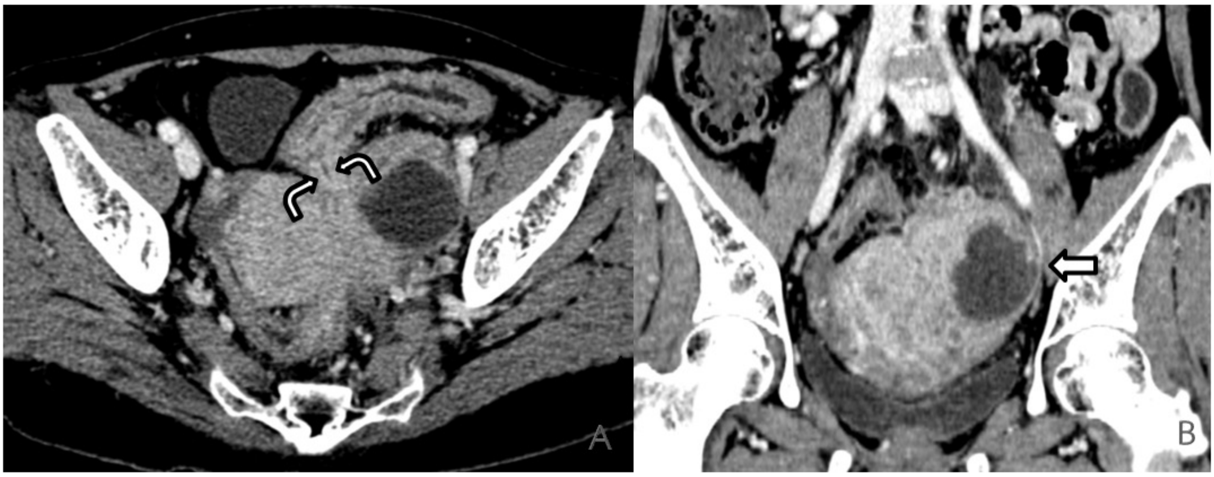

Figure 1. *A 58-year-old female presented with pelvic pain and history of 30 years of intrauterine device. CT scan portovenous phase A) axial plane and B) coronal plane demonstrated the irregular wall abscess at left adnexa (arrow) or ovarian abscess with fistulous tract (curve arrow) to sigmoid colon and bowel wall thickening.*

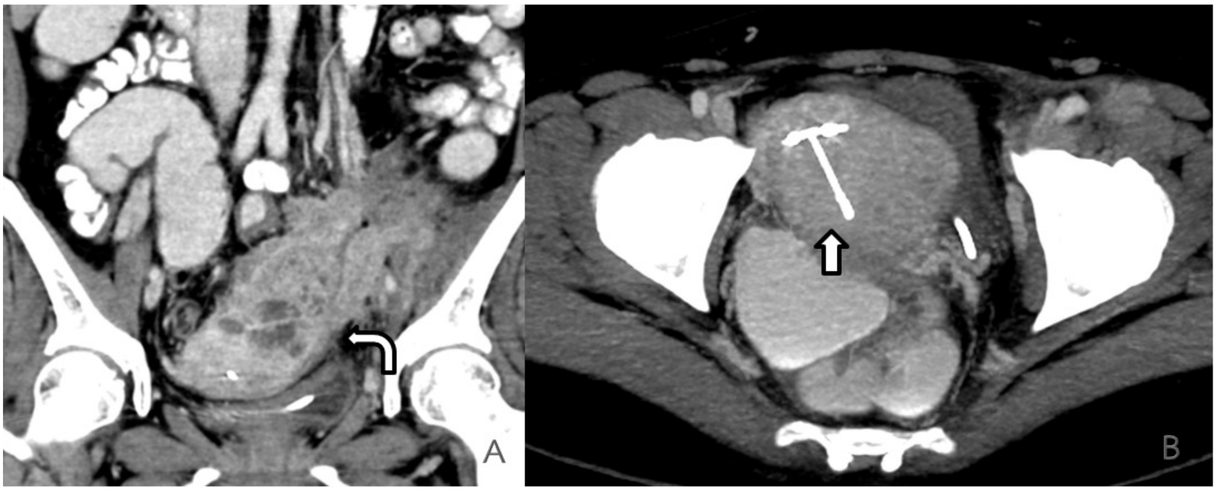

Figure 2. *A 48-year-old female presented with pelvic pain and history of 12 years of intrauterine device. CT scan portovenous phase A) coronal and B) axial plane demonstrated the irregular multiloculated abscess involved left adnexa (curve arrow), psoas muscle and iliopsoas with fistula tract from psoas muscle to posterior abdominal wall. Intrauterine device placed in the endometrial cavity (arrow).*

In two cases of renal actinomycosis, one had an underlying congenital single left kidney and presented with left flank pain and fever. Further CT showed multiple tiny rim-enhancing cystic lesions, probably representing chronic focal pyelonephritis or inflammatory pseudotumor and extended involvement of the left adrenal gland, spleen, and abdominal wall, and the differential diagnosis included renal cancer (Figure 3). Biopsies were performed to provide conclusive evidence of actinomycotic infection. Another patient presented with severe back pain, fever, and palpable mass. CT tomography revealed emphysematous pyelonephritis with perinephric abscess involving psoas muscle extension to the posterior pararenal space and posterior abdominal wall with multiple associated renal stones in the left kidney (Figure 4).

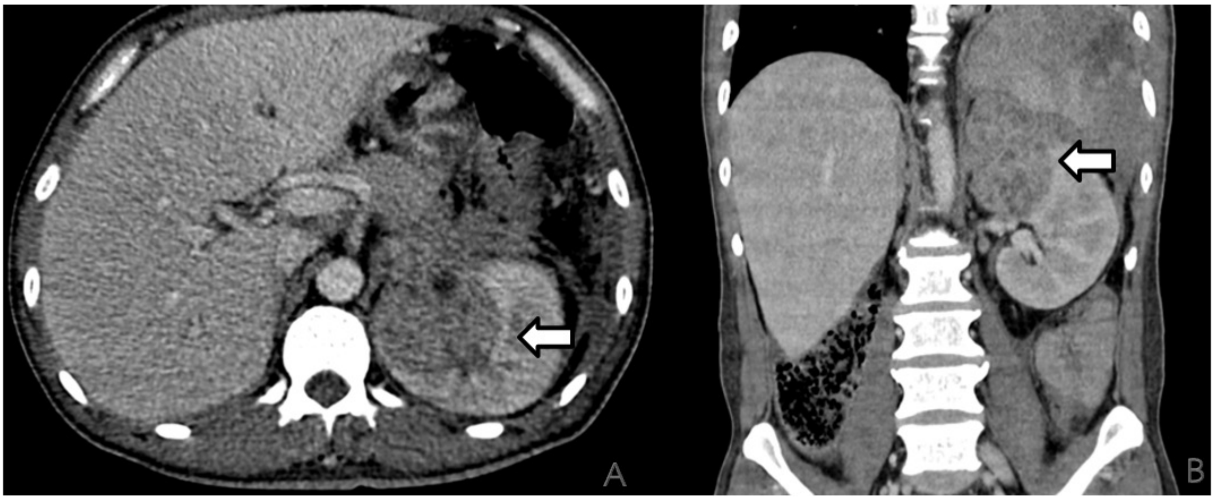

Figure 3. *A 47-year-old male with history of congenital single left kidney and presented with left flank pain. CT scan portovenous phase A) axial plane and B) coronal plane demonstrated multiple small rim-enhancing cystic lesions representing multiloculated abscess or inflammatory pseudotumor at upper pole of left kidney (arrow) involved left adrenal gland, spleen, and abdominal wall.*

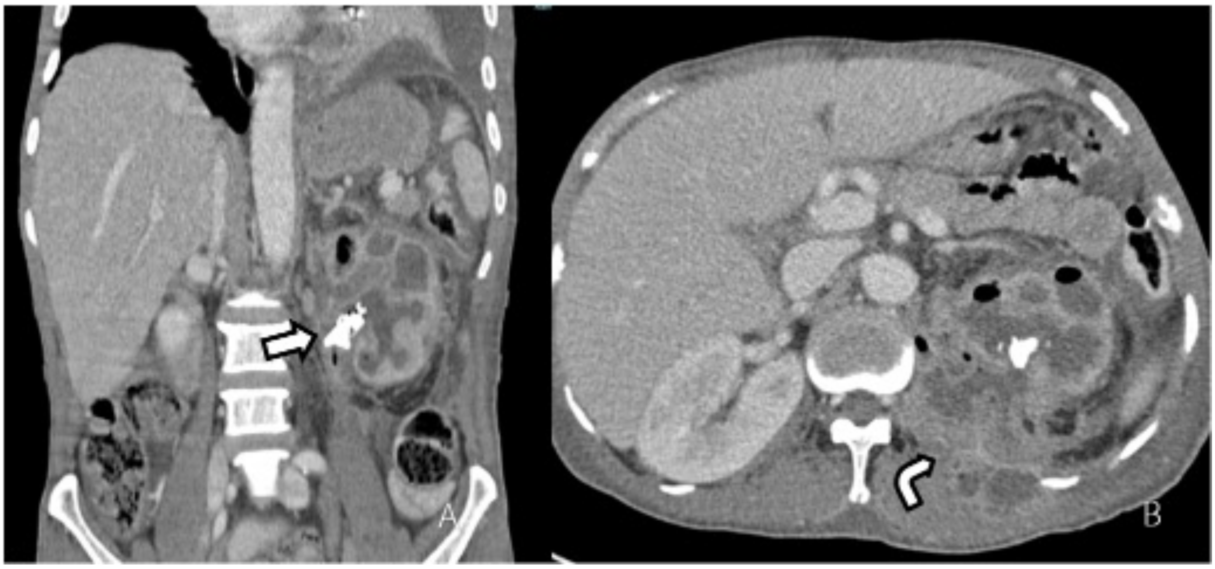

Figure 4. *A 60-year-old male known case type 2 Diabetes Mellitus presented with back pain, fever and palpable left flank mass. CT scan portovenous phase A) coronal plane and B) axial plane demonstrated multiple renal-pelvic stones (arrow) and hydronephrosis. Emphysematous pyelonephritis was noted with perinephric abscess of the left kidney involved psoas muscle and extension to posterior pararenal space and the posterior abdominal wall (curve arrow).*

In two cases were finally diagnosed with hepatic actinomycosis. One patient presented with recurrent cholangitis, and imaging demonstrated intrahepatic duct dilatation with an enhanced wall and an intrahepatic duct stone. Additionally, left portal vein thrombosis was observed, along with left lobe atrophy, which represented chronic cholangitis (Figure 5). In another case, a liver abscess initially presented as a mimic of a liver mass. Upon further investigation, biopsy was performed, and the results conclusively confirmed the presence of actinomycosis. A case of a palpable abdominal wall mass and CT demonstrated an ill-defined enhancing subcutaneous lesion at the mid-anterior abdominal wall (above the umbilicus and without umbilical involvement) with extension to the adjacent peritoneum and intra-abdominal fat reticulation.

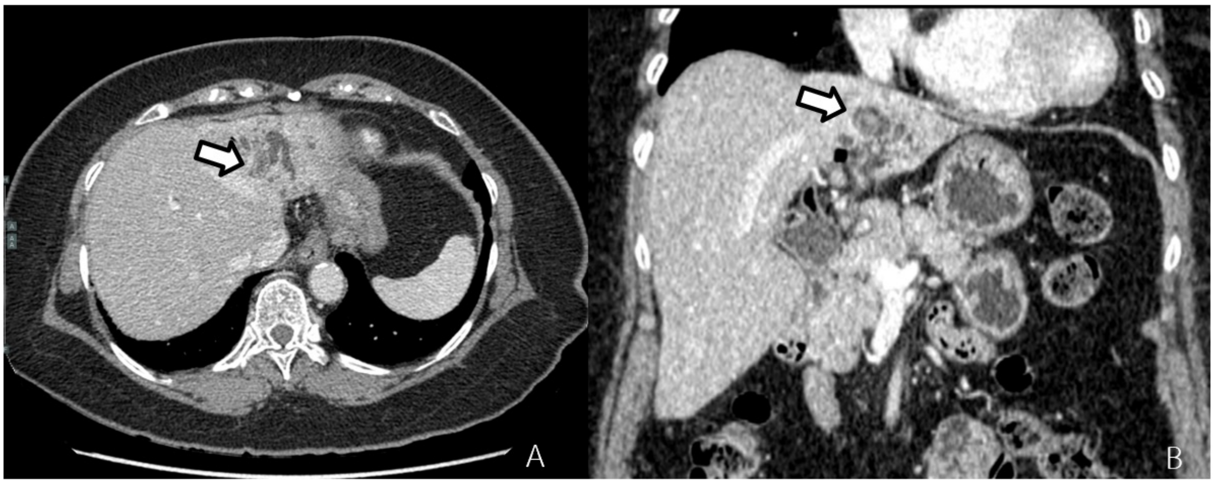

Figure 5. *A 76-year-old female with right upper quadrant pain; CT scan portovenous phase A) axial plane and B) coronal plane demonstrated chronic cholangitis at the left lobe of the liver; intrahepatic duct dilatation and intrahepatic duct stone (arrow).*

Surgical treatment and pathological characteristics, almost all the patients underwent surgical treatment (n=12, 92.3%). The diagnosis of actinomycosis was histologically confirmed in all cases. The modes of surgical treatment are summarized in Table 1. The mean hospital admission was 11.1 days (range, 1-36 days). The duration of treatment was less than 2 months in all patients (Table 1).

Discussion

Actinomycosis is a chronic suppurative bacterial infection caused by Actinomyces species. Actinomyces israelii is the organism most commonly found in humans. Actinomycosis usually manifests as abscess formation, dense fibrosis, and sinus drainage. The disease is further characterized by its tendency to spread extensively beyond the normal fascial and connective tissue planes. Disease manifestations can occur in various body regions, including the cervicofacial, thoracic, and abdominal areas. The majority of cases involve the face and neck (50-65%), followed by the chest (15-30%), and the abdominal region (approximately 20%). Pelvic involvement in the inguinal region is less common (3-5%) [3]. Infections typically progress slowly. Actinomycetes usually do not penetrate normal organ tissues, and infection results from the destruction of a normal mucosal barrier. This destruction can be attributed to accidents, surgical procedures, immunosuppression, or the introduction of foreign bodies, such as intrauterine devices or stones. A history of tissue damage, such as acute perforated appendicitis or diverticulitis, immunosuppression, or diabetes mellitus, poses a significant risk for Actinomycosis [1-3].

In cases of actinomycotic disease involving the bowel, the common CT finding is concentric wall thickening accompanied by a cystic or solid mass in the vicinity of the affected bowel segment [3]. In the large intestine, the cecum and transverse colon are frequently affected. Misdiagnosis can affect treatment decisions, potentially leading to a shift from localized surgery to more extensive procedures, including extended colon resection, which is often performed for cancer treatment [4-6].

Pelvic actinomycosis is strongly correlated with long-term intrauterine device usage [7-10]. Correlated with this study, two patients had a history of intrauterine device use of 12 and 30 years. Additionally, it can arise as an extension of abdominal actinomycosis, often stemming from latent ileocecal diseases. In such cases, the ovaries and fallopian tubes are frequently affected. Tubo-ovarian actinomycosis, a subtype of pelvic actinomycosis, tends to exhibit a more solid appearance than typical tubo-ovarian abscesses in the adnexal region. Moreover, pelvic actinomycosis has the potential to spread extensively to various adjacent structures, including the uterus, urinary bladder, rectal area, urachus, abdominal wall, and peritoneum [3]. This comprehensive involvement was also observed in this study.

Radiological imaging is integral to the diagnostic process, providing detailed insights into abnormalities and lesion boundaries. Computed Tomography (CT) scans are commonly utilized to evaluate masses or infections in the abdominal region. These scans may reveal characteristic patterns, such as solid masses with focal low-attenuation areas, more prevalent than cystic forms. Rim-enhancing lesions may also be observed, along with evidence of extension into adjacent tissues, creating potential diagnostic confusion with cancer [1-3]. Differential diagnoses include tuberculosis, Crohn's disease, and other inflammatory conditions. However, these modalities confirm the presence of masses or abscesses without distinguishing actinomycosis from malignancies, inflammatory bowel diseases, or infectious conditions, given the prevalence of solid masses with focal low-attenuation areas in this disease [1].

The review of the literature emphasizes that actinomycotic infection should be considered diagnostically in three specific clinical circumstances : (a) a series of manifestations including chronicity, extensive propagation across tissue planes, and firm to hard mass-like features, which are frequently confused with malignant disease; (b) drainage of an abscess by a sinus tract, which may spontaneously close and reform elsewhere; and (c) temporary improvement after a short course of antibiotic treatment, followed by frequent relapses [3]. Definitive diagnosis involves the identification of sulfur granules, conglomerates of filamentous bacteria, often accompanied by white blood cells, particularly neutrophils, in surgically obtained tissue samples (Figure 6). The limitation of the study is selection bias because the radiologists who re-interpreted the CT findings already knew the diagnosis of the patients, making the situation less authentic.

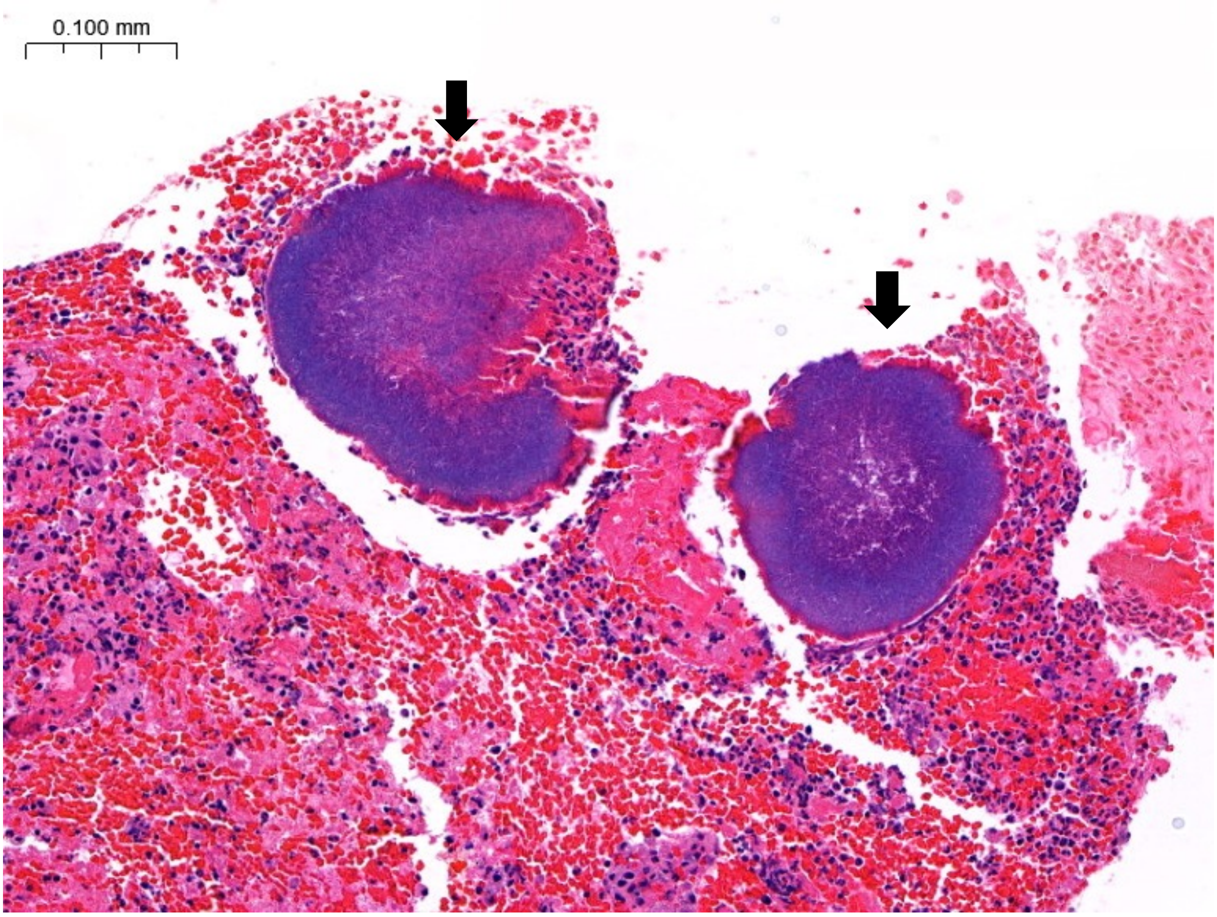

Figure 6. *The histologic section of liver biopsy showed filamentous gram positive bacterial colonies (arrow) in the inflammatory tissue background. (hematoxylin-eosin stain; H&E stain, original magnification x200).*

Conclusion

The key points of chronic clinical presentation, and CT imaging of abscess-liked lesion with an infiltrative pattern, associated with the fistula tract, retained foreign body or foreign body related history help clinicians and radiologists consider of this infection. That leads to proper management for patients. However, tissue diagnosis or pathogen identification are necessary for a definite diagnosis in case of tumor-mimic (inflammatory or pseudotumor formation) and for specific medical antibiotic treatment. CT serves as a valuable tool for monitoring the resolution or recurrence of abdominal actinomycosis. The duration of an antibiotic therapy should be tailored to each individual, optimizing the treatment plan based on the unique response of the patient.

Funding: None.

Competing interest: None.

Author contributions: All authors conceived of the presented idea, contributed to the design and implementation of the research, to the analysis of the results and to the writing of the manuscript.

References

1. Sung HY, Lee IS, Kim SI, Jung SE, Kim SW, Kim SY, et al. Clinical features of abdominal actinomycosis: a 15-year experience of a single institute. J Korean Med Sci 2011;26:932-7. doi: 10.3346/jkms.2011.26.7.932.

2. Vasilescu AM, Târcoveanu E, Lupascu C, Blaj M, Lupascu Ursulescu C, Bradea C. Abdominopelvic actinomycosis—the diagnostic and therapeutic challenge of the most misdiagnosed disease. Life (Basel) 2022;12:447. doi: 10.3390/life12030447.

3. Heo SH, Shin SS, Kim JW, Lim HS, Seon HJ, Jung SI, et al. Imaging of actinomycosis in various organs: a comprehensive review. Radiographics 2014;34:19-33.doi: 10.1148/rg.341135077.

4. Ridha A, Oguejiofor N, Al-Abayechi S, Njoku E. Intra-Abdominal actinomycosis mimicking malignant abdominal disease. Case Rep Infect Dis 2017; 2017: 1972023. doi: 10.1155/2017/1972023.

5. Bittencourt JA, Andreis EL, Lima EL, Dorn DE, Muller V. Actinomycosis simulating malignant large bowel obstruction. Braz J Infect Dis 2004;8:186-9. doi: 10.1590/s1413-86702004000200011.

6. Caplan E, Deputy M, Arul D, Wilson J. Actinomycosis of the omentum with invasion of the abdominal wall, small bowel and transverse colon mimicking malignancy. BMJ Case Reports 2019;12:bcr-2018-227728. doi: 10.1136/bcr-2018-227728.

7. Wagenlehner FM, Mohren B, Naber KG, Männl HF. Abdominal actinomycosis. Clin Microbiol Infect 2003;9:881-5. doi: 10.1046/j.1469-0691.2003.00653.x.

8. Nakahira ES, Maximiano LF, Lima FR, Ussami EY. Abdominal and pelvic actinomycosis due to longstanding intrauterine device: a slow and devastating infection. Autops Case Rep 2017;7:43-7. doi: 10.4322/acr.2017.001.

9. Stringer MD, Cameron AE. Abdominal actinomycosis: a forgotten disease? Br J Hosp Med 1987;38:125-7.

10. Yegüez JF, Martinez SA, Sands LR, Hellinger MD. Pelvic actinomycosis presenting as malignant large bowel obstruction: a case report and a review of the literature. Am Surg 2000 ;66:85-90.

Case Report

An uncommon case of blunt traumatic rupture gallbladder: A diagnostic challenge

Himraj Phukan, P.G.T.
Donboklang Lynser, M.D.
Gareth Yobel Lyngwa, M.D.
Chhunthang Daniala, M.D.
Donkupar Khongwar, M.S.
From North Eastern Indira Gandhi Regional Institute of Health and Medical Sciences, Shillong, Meghalaya, India.
Address correspondence to D.L. (e-mail: bokdlynser@gmail.com)

Received 5 July 2024; revised 16 August 2024; accepted 1 September 2024
doi:10.46475/asean-jr.v25i3.918

Abstract

Gallbladder injury secondary to blunt abdominal injuries is extremely rare and less than 2% of such cases have been reported. It is usually difficult to perform a clinical diagnosis due to absence of specific clinical symptoms. We present a case of a 31-year-old man with a history of drunk driving leading to a road traffic accident coming to our emergency department with mild pain in the periumbilical region. An accurate diagnosis was made by ultrasound (US) and computed tomography (CT). CT also revealed an injury to the adjacent hepatic segment. The patient was successfully treated with laparotomy and cholecystectomy. Here we discuss the conditions which may predispose to a gall bladder injury and the need for early radiological diagnosis before the signs of biliary peritonitis set in. Timely intervention carries a good prognosis.

Keywords: Bilio-hemoperitoneum, Blunt trauma, Cholecystectomy, Gallbladder rupture, Hepatic laceration.

Introduction

The gallbladder (GB) is a pear-shaped fibromuscular structure carefully nestled within and well protected by the surrounding structures such as ribs, the liver, the omentum and the intestine. In a collected 5,670 cases of blunt abdominal trauma, Penn has reported an incidence of 1.9% [1]. Injury to the GB most commonly occurs secondary to penetrative injuries [2]. Prompt clinical diagnosis is often challenging due to lack of specific clinical symptoms in such cases [3]. We present a case of traumatic GB laceration and associated injury to the inferior surface to the liver with an accurate preoperative diagnosis successfully managed by laparotomy and cholecystectomy.

Case summary

A 31-year-old man driving a car collided with another vehicle. He was under the influence of alcohol when brought to the emergency department of our hospital and complained of mild pain in the umbilical region and the left elbow. The patient was conscious but disoriented and drowsy. There was no history of loss of consciousness, seizure or vomiting. The clinical parameters were Glasgow Coma Scale (GCS) – 14/15. Blood Pressure (BP) - 158/103 mm Hg. Pulse – 82 bpm, normal in rhythm, volume and character. Respiratory Rate (RR) - 20/min and Saturation of Peripheral Oxygen (SpO2)- 98 % in room air. On examination, the abdomen was soft and revealed diffuse tenderness but no guarding or rigidity. There was no superficial abrasion. Bowel sounds were present. The examinations of respiratory, cardiovascular and central nervous system were unremarkable.

An Ultrasound (US) Extended Focused Assessment with Sonography in Trauma (E-FAST) revealed free fluid in the hepatorenal pouch and peri-splenic recess. The emergency team was informed and a proper ultrasound examination of the whole abdomen and pelvis was performed. The US examination revealed relatively collapsed GB lumen with echogenic contents within suggestive of hemorrhage and a focal defect near the fundus indicating perforation (Figure 1). The patient was taken for an urgent contrast-enhanced computed tomography (CECT) abdomen which confirmed the findings of US and revealed additional findings of intraparenchymal laceration of segment IV of the liver with features of the American Association for the Surgery of Trauma (AAST) grade III injury (Figure 2).

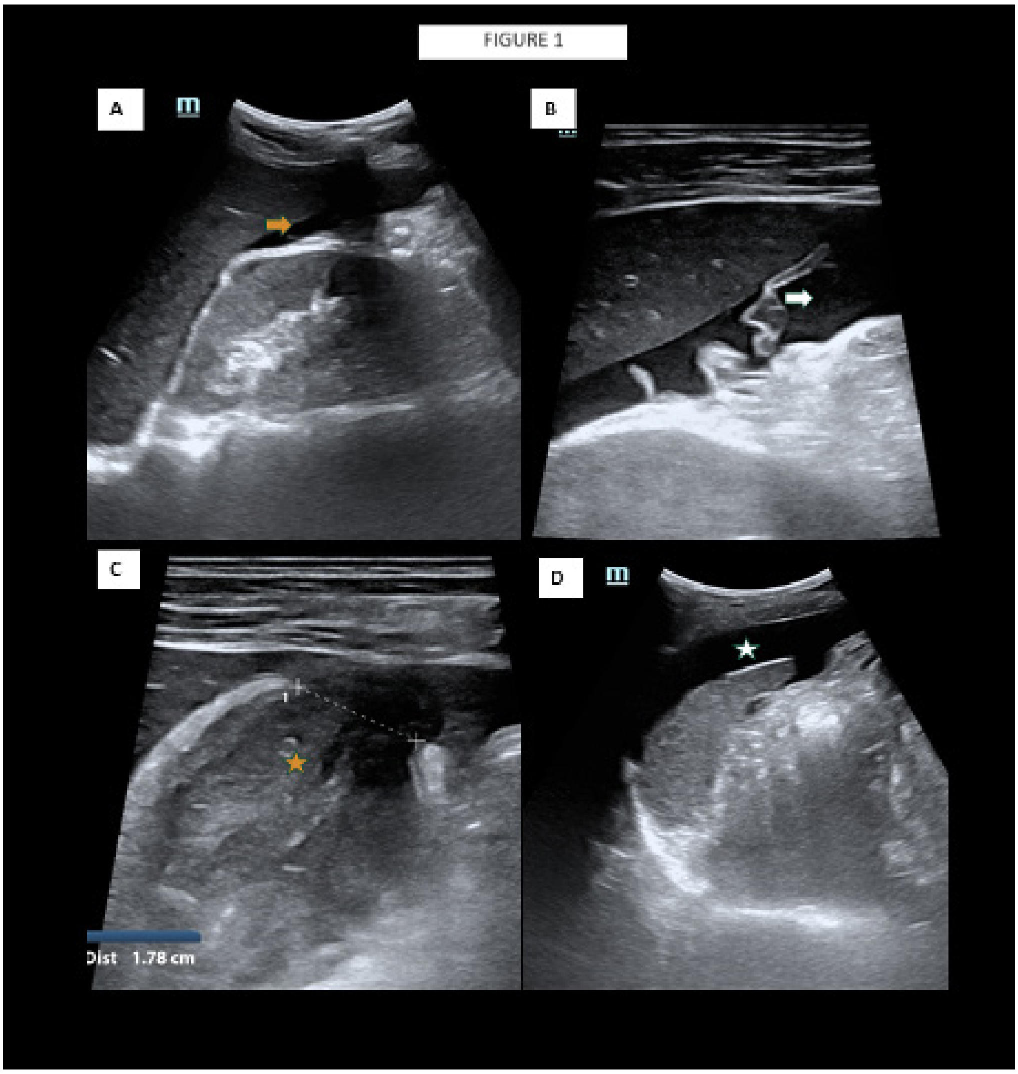

Figure 1. *Ultrasound images of the abdomen revealing A - free fluid in hepatorenal pouch (orange arrow), B - free fluid with internal echoes in the subhepatic space (white arrow), C - echogenic contents within the GB lumen suggestive of hemorrhagic fluid (orange star) and a focal transmural breach in the fundus measuring up to 1.7 cm, and D - free fluid in the perisplenic region (white star).*

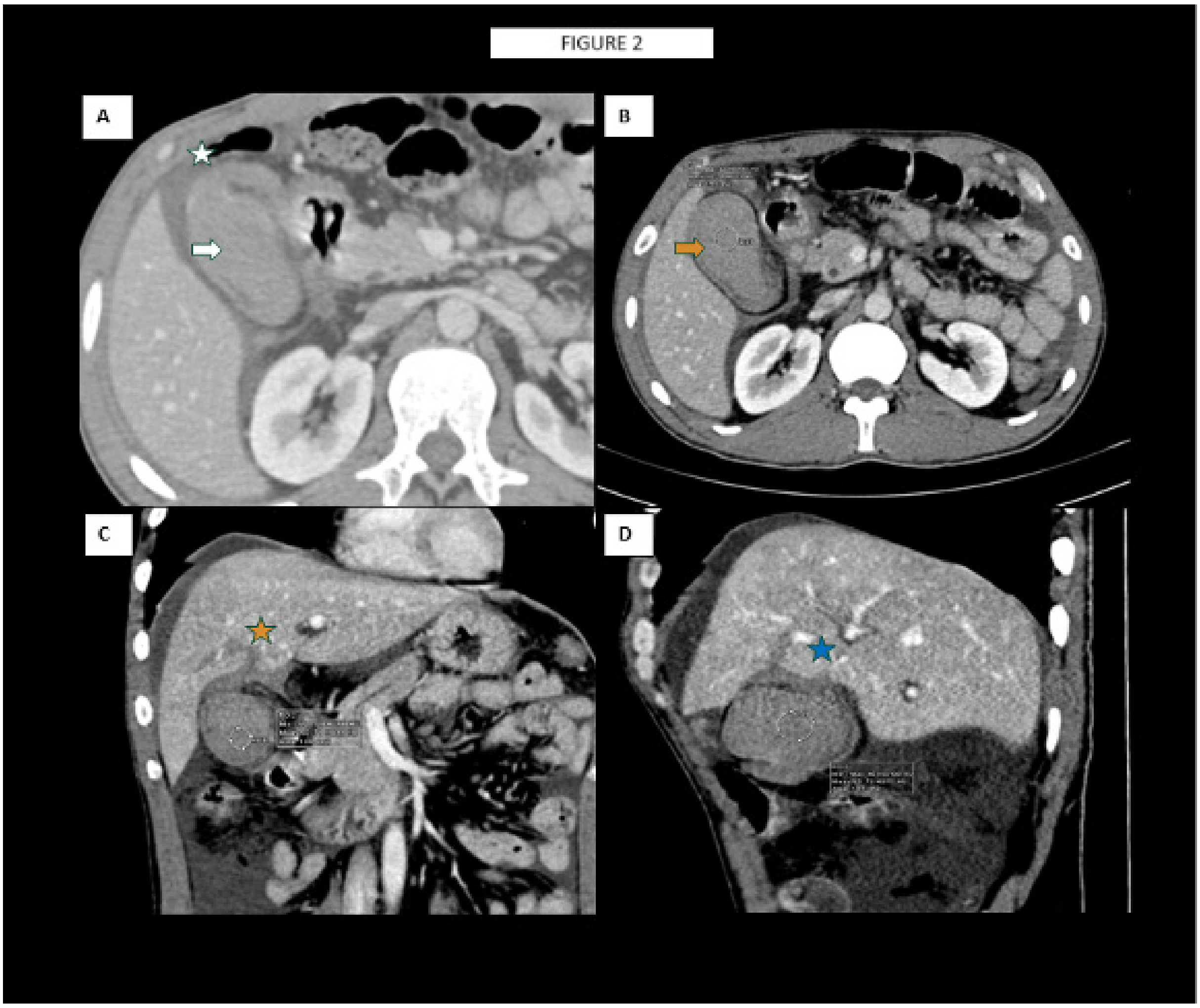

Figure 2. *Contrast enhanced CT images of the abdomen illustrating A- Axial image revealing hyperdense contents inside the GB (white arrow) with a focal defect in the fundus (white star), B- Axial image revealing hyperdense contents in the GB lumen, consistent with hemorrhagic fluid (orange arrow), C- coronal reconstruction revealing hyperdense contents within the GB lumen with serpiginous hypodense lacerations in segment IVb of liver (orange star), and D- Sagittal reconstruction of the hepatic laceration (blue star).*

The patient was admitted under surgical critical care (day 2). An US guided drain was placed by Radiology Department the next day (day 3) in the subhepatic region. Bilio-hemorrhagic fluid was draining measuring up to 1, 000 ml in 24 hrs. There was a fall in Hemoglobin levels with a rise in liver enzymes noted in the patient on day 3 as compared to day 1 which is depicted in Table 1.

Table 1. *Laboratory investigations.*

BLOOD INVESTIGATIONS	During presentation to Emergency (Day 1)	After admission (Day 3)
Hemoglobin (gm/dl)	18.8	15.4
Total Leucocyte Count (cells/microliter)	20 x 10^3	9 X 10^3
Prothrombin time/Activated partial thromboplastin time/International normalized ratio (sec)	11.3/27.1/1.01	12/31/1.2
Platelets (/ul)	310 x 10^3	250 X 10^3
Aspartate aminotransferase (IU/L)	428	993
Alanine transaminase (IU/L)	128	210
Alkaline phosphatase (IU/L)	96	243

Medical opinions were sought in view of increased hepatic enzymes. Injection thiamine, n-acetyl cysteine was given along with advice to maintain proper hydration and blood transfusion. Considering the continuous drainage from the peritoneal drainage catheter and dropping hemoglobin, the decision to perform laparotomy and cholecystectomy was made (Day 4). Per-operative findings were consistent with the imaging findings (Figure 3) and were subsequently confirmed on histopathology. The post operative course of the patient was uneventful, and he was discharged on Day 10. The patient's details were anonymized in this case report even though the patient had given his consent.

Figure 3. *Intraoperative image revealing transmural perforation of GB (white star) with bilio-hemorrhagic fluid (white arrow), and bile-stained bowels (blue arrow).*

Discussion

Blunt trauma to the gall bladder mostly occurs secondary to motor vehicle accidents, falls, blows, kicks or industrial accidents [2, 3]. Gall bladder injuries are normally classified into four types – contusion, avulsion, laceration and traumatic cholecystitis [1]. Losanoff and Kjossev have classified gall bladder injury (Table 2) into five types [4]. Our patient sustained a type 2 injury as per this classification.

Table 2. *Classification of Gall bladder injury by Losanoff and Kjossev [4].*

TYPE	INJURY OF GALL BLADDER:
1A	Contusion with intramural hematoma
1B	Contusion with perforation
2	**Rupture**
3A	Avulsion with partial detachment
3B	Avulsion with complete detachment from the liver but with attachment to the structures of the hepatoduodenal ligament (so-called “near traumatic cholecystectomy”)
3C	Torn only from the hepatoduodenal ligament
3D	Completely torn from all attachments (so-called “traumatic cholecystectomy”)
4A	Traumatic cholecystitis, secondary to haemobilia
4B	Acute acalculous cholecystitis
5	Mucosal tear with leakage of bile

One of the conditions predisposing to a gall bladder injury is distended GB lumen secondary to an empty stomach or a prolonged fasting status [5]. Thick-walled gall bladders are less prone to rupture [5]. Our patient had his last meal around 5 hours before the accident and had also consumed alcohol in the interim. Alcohol causes increased gastrin and secretin secretion which increases bile flow and elevates the pressure in biliary system by increasing the tone of Sphincter of Oddi [6]. Alcohol also relaxes the anterior abdominal wall muscles making the distended GB more prone to injury [7]. An underlying stiff cirrhotic liver also increases the risk of GB injury [8-9]. Clinical symptoms may be apparent only if biliary peritonitis has set in which can take days to weeks. Ultrasonography is usually the first imaging modality performed in a case of acute pain abdomen in many parts of the world. In cases of a gall bladder injury, the lumen often collapses and contains echogenic fluid due to hemorrhage. Rarely is the gall bladder seen abnormally distended due to hemorrhagic fluid in the lumen. A transmural disruption of the wall can also be seen when the perforation is large. Associated low level echogenic free fluid can also be detected suggestive of bilio-hemoperitoneum. CT has better accuracy to identify, hemoperitoneum, injury to liver, duodenum or other solid organs. In our case, the laceration in the adjacent liver parenchyma (AAST III) was managed conservatively.

Magnetic resonance imaging (MRI), endoscopic retrograde cholangio-pancreaticography (ERCP), biliary isotope scintigraphy and diagnostic laparoscopy are some other investigations which can be carried out and are performed very rarely only when US or CT evaluation is suboptimal in minor or low-grade injuries presenting insidiously as bile leak. Once a diagnosis of GB injury has been established, immediate cholecystectomy is the treatment of choice [10]. Simple drainage and temporary abdominal closure are performed in patients exhibiting symptoms of physiologic fatigue due to vascular injuries and are planned for a re-exploration surgery [10]. Conservative management is generally not recommended as late complications such as necrosis or perforation have been reported [11]. Delayed xanthogranulomatous changes can be seen in a traumatic GB mimicking a carcinoma and leading to a diagnostic and therapeutic dilemma [12]. We must also be aware of other etiologies that may mimic GB hemorrhage viz, milk of calcium, hyperdense sludge or vicarious excretion of intravenous contrast material [13].

Conclusion

As evident in our case, the early clinical signs of a gall bladder injury can be vague and even absent in some cases. An early imaging evaluation by US and CT is warranted whenever a gall bladder injury is suspected. Early diagnosis and intervention in a gall bladder injury carries a good prognosis. High morbidity is seen when the management is in delay or if conservative management is attempted. A multidisciplinary team consisting of emergency physicians, radiologists and surgeons, is critical for early diagnosis and optimal treatment of such cases.

References

1. Penn I. Injuries of the gallbladder. Br J Surg 1962;49:636-41. doi: 10.1002/bjs.18004921816.

2. Sharma O. Blunt gallbladder injuries: presentation of twenty-two cases with review of the literature. J Trauma 1995;39:576-80. doi: 10.1097/00005373-199509000-00029.

3. Soderstrom CA, Maekawa K, DuPriest RW Jr, Cowley RA. Gallbladder injuries resulting from blunt abdominal trauma: an experience and review. AnnSurg 1981;193:60–6. doi: 10.1097/00000658-198101000-00010.

4. Losanoff JE, Kjossev KT. Complete traumatic avulsion of the gallbladder. Injury 1999 ;30:365-8. doi: 10.1016/s0020-1383(99)00072-8.

5. Posner MC, Moore EE. Extrahepatic biliary tract injury: operative management plan. J Trauma 1985;25:833-7. doi: 10.1097/00005373-198509000-00004.

6. Spigos DG, Tan WS, Larson G, Palani C, Zaitoon MM, Capek V. Diagnosis of traumatic rupture of the gallbladder. Am J Surg 1981;141:731-5. doi: 10.1016/0002-9610(81)90089-1.

7. Smith SW, Hastings TN. Traumatic rupture of the gallbladder. Ann Surg 1954;139:517-20. doi: 10.1097/00000658-195404000-00019.

8. Su HY, Wu MC, Chuang SC. Isolated gallbladder rupture following blunt abdominal injury. Niger J Clin Pract 2016;19:301-2. doi: 10.4103/1119-3077.164352.

9. Philipoff AC, Lumsdaine W, Weber DG. Traumatic gallbladder rupture: a patient with multiple risk factors. BMJ Case Rep 2016;2016:bcr2016216811. doi: 10.1136/bcr-2016-216811.

10. Ball CG, Dixon E, Kirkpatrick AW, Sutherland FR, Laupland KB, Feliciano DV. A decade of experience with injuries to the gallbladder. J Trauma Manag Outcomes 2010 ;4:3. doi: 10.1186/1752-2897-4-3.

11. Laffey DA, Hay DJ. Isolated perforation of the gall bladder following blunt abdominal trauma. Postgrad Med J 1979;55:212-4. doi: 10.1136/pgmj.55.641.212.

12. Mohanty D, Agarwal H, Aggarwal K, Garg PK. Delayed rupture of gallbladder following blunt abdominal trauma. Maedica (Bucur) 2014;9:266-8.

13. Birn J, Jung M, Dearing M. Isolated gallbladder injury in a case of blunt abdominal trauma. J Radiol Case Rep 2012;6:25-30. doi: 10.3941/jrcr.v6i4.941.

Case Report

MR imaging appearance of long bone sarcoidosis

Debajyoti Saha, M.D.
Ryan Tai, M.D.
Ganesh Joshi, M.D.
Aidan P. McAnena
From Department of Radiology, UMass Memorial Medical Center,
University of Massachusetts Chan Medical School, North Worcester, MA, USA.
Address correspondence to D.S. (e-mail: drdsaha13@gmail.com)

Received 1 July 2024; revised 12 November 2024; accepted 12 December 2024
doi:10.46475/asean-jr.v25i3.916

Abstract

Sarcoidosis is a non-caseating granulomatous disease with common involvement of the lungs and lymph nodes. Osseous involvement is rare, with long bone involvement even rarer. One of the characteristic MRI findings that point towards osseous sarcoidosis is the presence of intra- or perilesional fat. Lesions that involve long bones usually show no cortical destruction or periosteal reaction, in contrast to small bones, which show cortical destruction or extraosseous extension. In patients with diagnosed sarcoidosis, bone biopsy could be averted in patients having characteristic findings on MRI. In patients without a diagnosis of sarcoidosis with multiple osseous lesions and aforementioned imaging findings, sarcoidosis can be provided on the differential diagnosis.

Keywords: Bone, MRI, Sarcoidosis.

Introduction

Sarcoidosis is a multi-system inflammatory disorder with non-caseous granulomas of unknown etiology in the involved organs. It has bimodal distribution with the first peak between ages 20-40 and the second peak being above 50 years and older [1]. Mediastinal lymph nodes and lungs are most commonly affected in approximately 90% of the patients with sarcoidosis [2]. Osseous sarcoidosis (OS) is not very common and involves only 1-13% of the patients with sarcoidosis. The appendicular skeleton, in particular the hands and feet, are commonly affected. The axial skeleton is involved to a lesser degree where it may resemble metastasis [3]. Knowledge of OS may not be well established in clinical practice as the reported prevalence is low. For example, Neville et al. reported OS in 1-15% of patients with sarcoidosis [4]. Similarly, James et al. [5] reported prevalence of 3-13% and Sparks et al. [6] reported around 1.5%. The low prevalence of OS may be due to underdiagnosis as patients with OS may be asymptomatic. However, in patients with diagnosed sarcoidosis, bone biopsy can be averted if there are certain imaging features pointing towards OS, which will be discussed further in the article.

Here we present two cases of OS showing contrasting features on MRI. According to authors' knowledge, there is no reported case of a patient with breast cancer with multiple long bone lesions secondary to OS and was also followed up for 4 years with MRI to establish stability and to exclude the possibility of metastases.

Case summary

Case 1

A 65-year-old man presented with shoulder pain for 6 months. The initial radiograph of the shoulder was negative. Since the symptoms were persistent and rotator cuff tear was suspected, MRI of the shoulder was ordered which demonstrated T1 hypointense and T2 hyperintense intramedullary lesions in the proximal humerus. There was a small focus of the central intrinsic T1 hyperintense signal and the corresponding low signal on fat saturated images, which was consistent with intralesional fat (Figure 1). There was minimal endosteal thinning of the cortex suggesting a benign and chronic process. Eventually a biopsy was performed to rule out malignancy. The pathology demonstrated multiple non-caseating granulomas consistent with OS. A subsequently performed CT chest demonstrated multiple enlarged calcified hilar and mediastinal lymph nodes with scattered multiple pulmonary nodules. He did not exhibit any pulmonary symptoms. He was given intra-articular steroids for his shoulder pain, which provided significant relief from his pain.

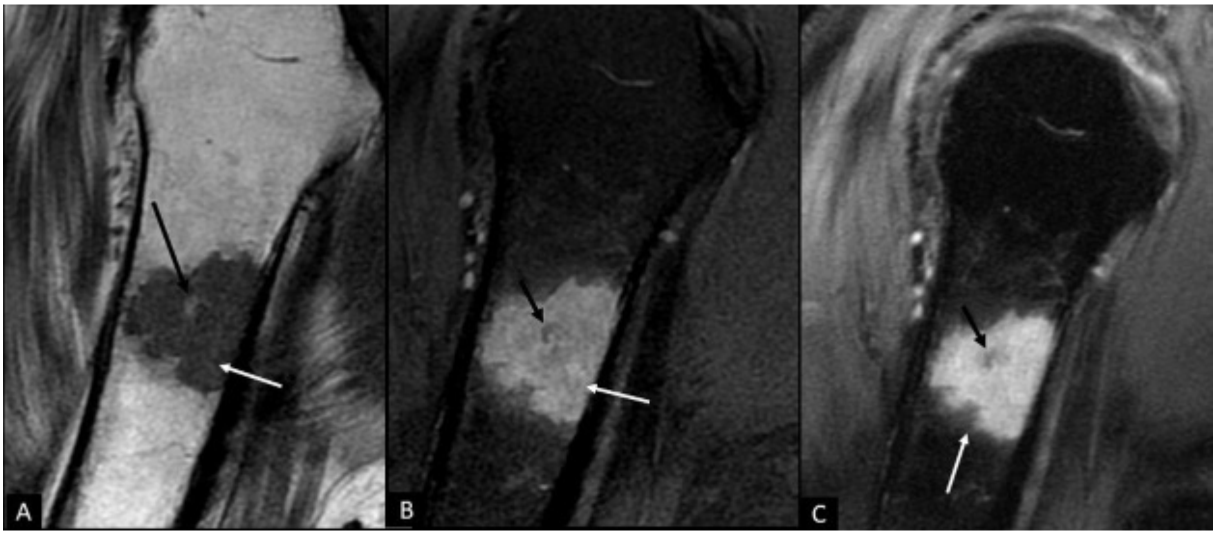

Figure 1. *Sagittal (A) T1 weighted and (B) PD fat saturated MR images of the shoulder. With the proximal humeral diaphysis, there is a well-defined intramedullary lesion, which is hypointense on the T1 weighted image and hyperintense on the PD fat saturated image (white arrow) with intrinsic T1 hyperintense signal and corresponding low signal on fat-saturated image consistent with intralesional fat (black arrow). There is no perilesional edema, cortical destruction, or extraosseous soft tissue component. (C) T1 weighted post contrast fat saturated image demonstrates diffuse enhancement (white arrow).*

Case 2

A 53-year-old woman presented with severe hip pain with radiation to the knee for 6 months. She had a history of poorly differentiated infiltrating breast cancer treated with lumpectomy followed by adjuvant chemoradiation and was under surveillance. She was also diagnosed with sarcoidosis from cervical lymph-node biopsy and was followed conservatively as she did not have any pulmonary symptoms. On the examination of the hip, there was tenderness to palpation over greater trochanter and a clinical diagnosis of trochanteric bursitis was made. Due to the recurrence of her hip pain, MRI was done, which showed T2 hyperintense lesions with an intrinsic T1 hyperintense signal and a corresponding low signal on short-tau-inversion-recovery (STIR) and fat saturated images (FS) (Figure 2). These imaging findings were in keeping with large bone OS in this patient with sarcoidosis. Of note, she also had a shoulder MRI performed four years ago, which also showed intramedullary lesions but the signal characteristics were different from the lesions in the hip. The lesions were T1 hypointense and hyperintense on PD FS images (Figure 3). However, the intrinsic T1 hyperintense signal was not seen. Due to her history of breast cancer, she was followed closely with repeated MRIs. In the follow-up, there was complete resolution of the lesions on MRI. She was offered intermittent cortisone injections of her shoulder and hip joints, which provided relief to the patient.

The summary of the MRI features of large bone OS lesions in our cases is as follows: multiple intramedullary lesions that are predominately hypointense on T1-weighted imaging and intermediate/hyperintense on T2-weighted imaging with a central intralesional fat signal and variable post-contrast enhancement.

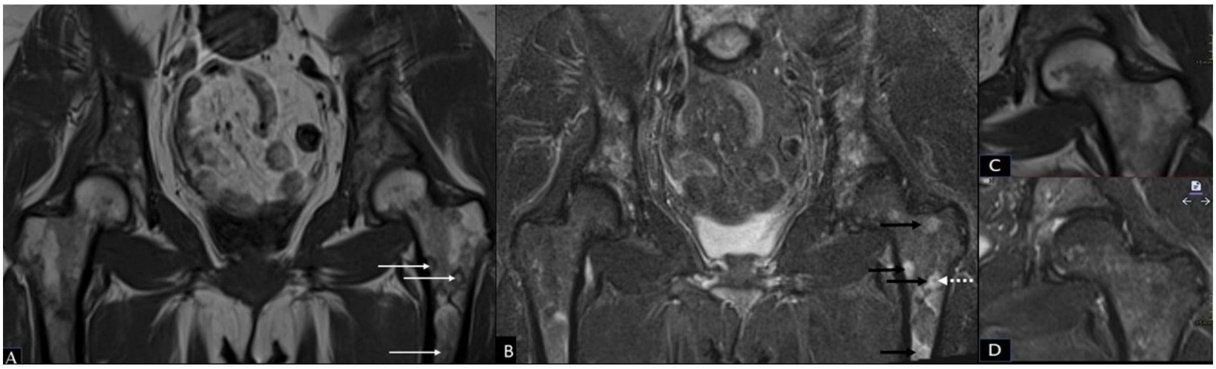

Figure 2. *Coronal T1-weighted (A) and STIR images of the pelvis (B) show extensive multifocal intramedullary lesions in the proximal femurs that demonstrate T2 hypertense signal (black arrows) with intrinsic T1 hyperintense signal (white arrows) and corresponding low signal on STIR (broken white arrow): These findings are in keeping with large bone sarcoidosis in a patient with known history of sarcoidosis. Follow-up coronal T1-weighted (C) and STIR (D) MRI images of the left hip performed 4 years later demonstrates complete resolution of the lesions.*

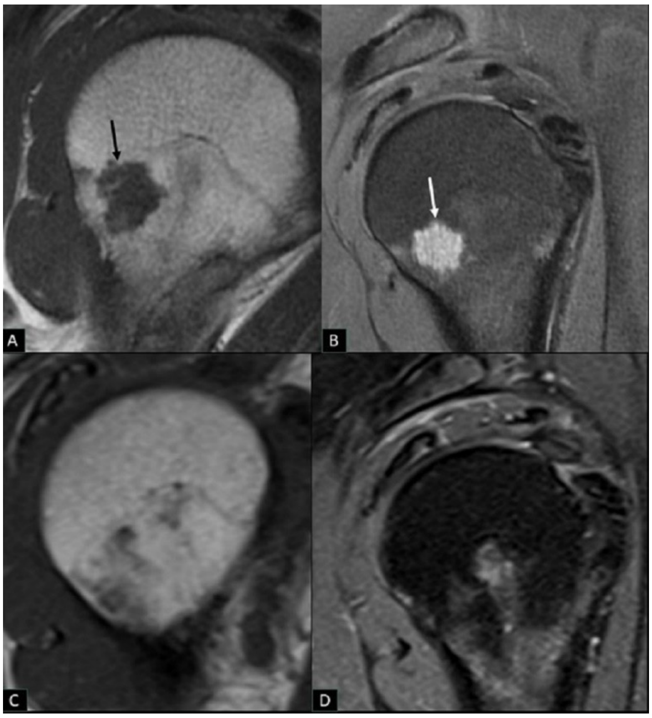

Figure 3. *Sagittal T1-weighted (A) and PD fat saturated images (B) of the shoulder demonstrates well-defined intramedullary lesion in the proximal humeral meta-diaphysis, which is hypointense on the T1 weighted image (black arrow) and hyperintense on the PD fat saturated image (white arrow). There is no perilesional edema or cortical destruction or extraosseous soft tissue component. Follow-up sagittal T1-weighted (C) and STIR (D) MRI images of the left shoulder 8 years later shows complete resolution of the lesion.*

Discussion

Sarcoidosis is a non-caseating granulomatous disease commonly involving lungs and lymph nodes with osseous involvement in 1-13% of cases [3]. OS could be the initial presentation of undiagnosed sarcoidosis, which may resemble metastasis [7]. The radiographic features of small and large bone OS are variable.

The more common small bone OS has characteristic radiographic features, which are well-described in the literature. Small bone OS may present unilaterally or bilaterally and is usually asymmetric and commonly involves the second or third fingers. The bones demonstrate a characteristic pattern of osteolysis with cystic, lacy and honey-comb like appearance; other features may include cortical destruction, extraosseous extension, soft tissue edema, and sausage finger. Deformities in the hand can occur, which is usually due to a pathological fracture or osseous remodeling [1].

The less common large bone OS is usually multifocal with 50% of the patients being asymptomatic [8]. A study by Mostard et al. demonstrated that one-third of the patients with severe sarcoidosis were found to have multifocal osseous lesions on PET/CT without lesions discernible on low-dose CT [9]. On radiographs, the lesions are often occult or lytic with no cortical destruction or periosteal reaction, similar to our patient. Some lesions may also be mixed or sclerotic [10, 11].

On MRI, large bone OS lesions usually present as multiple, well-defined or indistinct, intramedullary lesions that are hypointense on T1-weighted imaging and intermediate/hyperintense on T2-weighted imaging with variable post contrast enhancement [7]. The lesions may also spontaneously resolve, which was also in our case [3]. A study by Moore et al. [3] concluded that the presence of intralesional or perilesional fat has high specificity but low sensitivity in differentiating OS from metastasis. We postulate that the presence of intralesional fat within the OS lesions is secondary to involution with deposition of fat within the lesion in the setting of chronic inflammation. Islands of red marrow may present similarly to OS on MRI, as red marrow may also contain fat. In both cases of OS, the OS lesions are mass-like with well-defined convex margins, whereas islands of red marrow have less well-defined margins.

The presence of intralesional fat within an intramedullary lesion would strongly suggest OS in a patient with a known history of sarcoidosis. But there are other differential diagnoses to these osseous lesions. Vascular lesions such as hemangiomas may be difficult to discern from OS based on signal characteristics alone. However, hemangiomas may be distinguished from OS morphologically with its spiculated lattice-like appearance, which may be more obvious with CT. However, if the OS lesion demonstrates a T2 hyperintense signal with a T1 hypointense signal, the OS lesion would be difficult to discern from other bone marrow replacement processes such as metastases, hematogenous spread of osteomyelitis, and brown tumors. In these cases, clinical presentation is important in formulating a differential diagnosis. Histological correlation may also be needed to confirm a diagnosis.

In patients with diagnosed sarcoidosis and intramedullary bone lesions, the presence of intra- or perilesional fat would point towards OS and biopsy could be averted as was the case in our second patient. In patients with no prior diagnosis of sarcoidosis and have all the imaging findings described, sarcoidosis can be provided as a differential in the appropriate clinical context. In conclusion, the knowledge of the imaging characteristics of large bone OS lesions on MRI is important to provide an accurate differential diagnosis, and potentially avert unnecessary biopsy and concern to the patient.

References

1. Brandão Guimarães J, Nico MA, Omond AG, Silva FD, Aivazoglou LU, Carneiro BC, et al. Radiologic manifestations of musculoskeletal sarcoidosis. Curr Rheumatol Rep 2019;21:7. doi: 10.1007/s11926-019-0806-0.

2. Baughman RP, Teirstein AS, Judson MA, Rossman MD, Yeager H Jr, Bresnitz EA, et al. Clinical characteristics of patients in a case control study of sarcoidosis. Am J Respir Crit Care Med 2001;164(10 Pt 1):1885–9. doi: 10.1164/ajrccm.164.10.2104046.

3. Moore SL, Kransdorf MJ, Schweitzer ME, Murphey MD, Babb JS. Can sarcoidosis and metastatic bone lesions be reliably differentiated on routine MRI? AJR Am J Roentgenol 2012;198:1387–93. doi: 10.2214/AJR.11.7498.

4. Neville E, Carstairs LS, James DG. Sarcoidosis of bone. Q J Med 1977;46:215-27.

5. James DG, Neville E, Siltzbach LE. A worldwide review of sarcoidosis. Ann N Y Acad Sci 1976;278:321-34. doi: 10.1111/j.1749-6632.1976.tb47043.x.

6. Sparks JA, McSparron JI, Shah N, Aliabadi P, Paulson V, Fanta CH, et al. Osseous sarcoidosis: clinical characteristics, treatment, and outcomes--experience from a large, academic hospital. Semin Arthritis Rheum 2014; 44:371-9. doi: 10.1016/j.semarthrit.2014.07.003.

7. Talmi D, Smith S, Mulligan ME. Central skeletal sarcoidosis mimicking metastatic disease. Skeletal Radiol 2008;37:757–61. doi: 10.1007/s00256-008-0479-7.

8. Sparks JA, McSparron JI, Shah N, Aliabadi P, Paulson V, Fanta CH, et al. Osseous sarcoidosis: clinical characteristics, treatment, and outcomes--experience from a large, academic hospital. Semin Arthritis Rheum 2014; 44:371–9. doi: 10.1016/j.semarthrit.2014.07.003.

9. Mostard RL, Prompers L, Weijers RE, van Kroonenburgh MJ, Wijnen PA, Geusens PP, et al. F-18 FDG PET/CT for detecting bone and bone marrow involvement in sarcoidosis patients. Clin Nucl Med 2012 ;37:21–5. doi: 10.1097/RLU.0b013e3182335f9b.

10. Moore SL, Teirstein A, Golimbu C. MRI of sarcoidosis patients with musculoskeletal symptoms. AJR Am J Roentgenol 2005;185:154–9. doi: 10.2214/ajr.185.1.01850154.

11. Moore SL, Teirstein AE. Musculoskeletal sarcoidosis: spectrum of appearances at MR imaging. Radiographics 2003;23:1389–99. doi: 10.1148/rg.236025172.

THE ASEAN JOURNAL OF RADIOLOGY
ISSN 2672-9393

Review Article

Integrating machine learning into medical radiology: Principles, applications, challenges, and future directions

Wisitsak Pakdee, M.D.[1]
Sorawat Sangkaew, M.D., Ph.D.[2][3]
Richard C Wilson, M.Sc., M.Pharm.[2]
Pramot Tanutit, M.D.[1]
From [1]Department of Radiology, Faculty of Medicine, Prince of Songkla University, Songkhla, Thailand,
[2]Department of Infectious Disease, Faculty of Medicine, Imperial College London, London, UK,
[3]Department of Social Medicine, Hatyai Hospital, Songkhla, Thailand.
Address correspondence to S.S. (email: Sorawat.sa@cpird.in.th)

Received 27 September 2022; revised 14 December 2024; accepted 14 December 2024
doi:10.46475/asean-jr.v25i3.188

Abstract

Over recent decades, machine learning has been widely implemented in medical radiology. Radiologists, who are at the forefront of clinical practice, need to be aware of the benefits of machine learning to facilitate its implementation. It is crucial for them to thoroughly understand and effectively integrate machine learning into the practical realm of medical radiology.

In this review, we highlight the principles and applications of machine learning in medical radiology and provide a summary of its development in this field. Machine learning has significantly advanced diagnostic imaging, enhancing detection, segmentation, and image reconstruction, while improving workflow efficiency and radiology reporting. Current literature indicates three primary challenges in implementing machine learning: data standardization, validation of model performance, and regulatory compliance. The successful integration of machine learning in clinical practice requires robust data security protocols and clear frameworks for professional accountability. To prepare for this technological transition, radiologists must develop new competencies through enhanced educational programs and adapt their roles to focus more on clinical decision-making and multidisciplinary collaboration while leveraging machine learning as a supportive tool.

Keywords: AI, Artificial intelligence, Artificial neural network, Deep learning, Machine learning.

Introduction

Medical imaging plays an essential role in parts of patient care, from screening and diagnosing, to planning further management. The demands of medical imaging have been increasing over recent decades due to the ready availability of imaging technology and demand for higher standards of patient care [1, 2]. However, this increased demand has not been met by a proportional increase in the number of radiologists [3]. Due to time pressure, radiologists are challenged to make a decision based on integrating radiological and clinical information, and patient preferences. Furthermore, it is also difficult for radiologists to work effectively within the multidisciplinary team.

To assist radiologists in providing standard medical care despite overwhelming workloads and limited time, rigorous machine learning techniques have been developed and widely implemented in medical radiology over the last three decades (Box 1). Since the 2000s, machine learning has been increasingly applied in medical services, particularly in the field of radiology, to reduce radiologists' workload and enhance diagnostic performance. The trend of machine learning has grown exponentially since 2010, with the generation of algorithms transitioning to model-free and purely data-driven approaches, which require large datasets for training and supervision [4]. An example of a model-free and data-driven algorithm in the field of radiology is 'texture analysis' or 'radiomics,' which provides tumor segmentation and classification of tumor subtypes [4]. After 2018, AI has shifted from deep learning models to foundation models, which aim to generate new content, including text, sound, and images. While AI can now respond to complex tasks, there is a risk of AI hallucinations and biases stemming from the training data [5].

Although machine learning is a promising tool contributing to improved medical service and reducing radiologists' workload, it has been criticized in terms of how it will be integrated into routine practice. Regulatory and ethical issues have also been raised.

Comprehensively understanding and integrating machine learning into the real world of medical diagnosis is essential. Radiologists need to be prepared to adapt their roles and learn how to utilize machine learning in smart and effective ways.

Here we briefly summarise basic principles and the development of machine learning in medical radiology and highlight its applications in this field. We also discuss the current challenges and future perspectives of machine learning. Finally, we suggest how radiologists can prepare for the future integration of machine learning into workflow.

Box 1

The term 'machine learning' was first introduced in 1957 by Arthur Samuel who described algorithms for computers to solve problems by learning from existing data without explicitly predefined rules [5]. However, there were several limitations mainly caused by a lack of computational power and insufficient availability of data. Model performance was faced with overfitting and expensive computing time. Since 1980s computers were radically improved in computational capacity and widely implemented in all scientific fields; as a result, numerous machine learning techniques were adopted in scientific research. At the same time, computer-aided systems were introduced into medical radiology although they were mainly based on a set of rules defined by human knowledge [4]. After that, in the 1990s, statistical models have been mainly used for CADs to incorporate both human knowledge and statistical parameters from data [4, 6, 7]. These CADs provide the probability of the outcome of interest. However, the high dimensional data from radiological images were limited with model assumptions and data transformation. Since the 2000s, machine learning approaches, which are model-free and driven with now-available high dimensional data, therefore obtain more popularity in multiple fields with influential studies spreading from all modalities in radiology in the early 2000s [4].

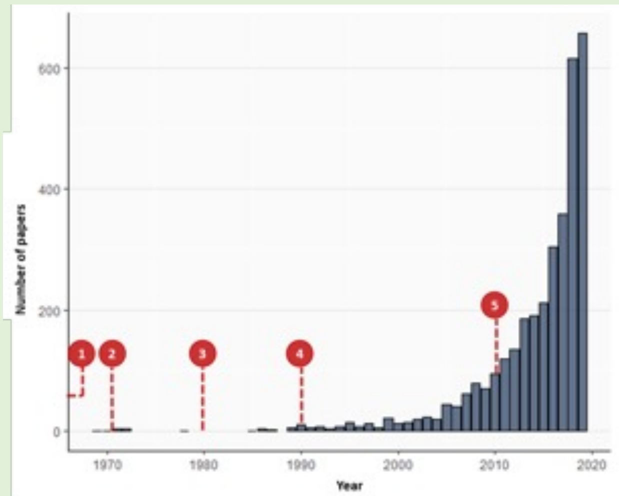

Box 1 Figure. *The bar chart shows the number of papers from a MEDLINE search each year. ① 1950 First artificial intelligence introduced; ② 1970s Computers and Radiology Information Systems implemented; ③ 1980s Rules-based CADs mainly used; ④ 1990s Statistical based CADs implemented; and ⑤ 2010 Deep learning-based CADs mainly used.*

Terminology and basic principles

Computer-aided systems

Computer-aided detection (CADe) and computer-aided diagnosis (CADx) are both computer-based systems that assist radiologists in making a decision based on information obtained from radiological images [6, 7]. While CADe recognizes suspicious patterns on images and aims to assist radiologists in identifying abnormal findings, CADx analyses medical images and eventually provides a probability that a specific disease is present [8]. Both computer-based systems comprise multiple steps, including data analytic algorithms which can be based on rules, statistics, or artificial intelligence (AI).

Artificial intelligence and machine learning

Artificial intelligence is a field of computer science that creates systems performing tasks that usually require human problem-solving skills [9]. Machine learning, which is a subfield of AI, comprises a set of techniques that allows a computer program to learn and improve its performance using existing data without being explicitly programmed. Machine learning can be categorized into three main groups based on tasks: supervised learning, unsupervised learning, and reinforcement learning [10]. About supervised learning, pre-defined, or "labeled", outcomes (e.g. BI-RADS classification in mammography) are required in data input. The labeled data is used to train computer algorithms that make predictions when applied to new data. In contrast, unsupervised learning does not need labeled data; the algorithms recognize data patterns and classify the data into subgroups based on the similarity of each data point. Lastly, reinforcement learning learns from iterative trial and error to achieve specific tasks. The algorithms receive rewards and penalties based on the action each round and then assemble all feedback as the weight of each network.

Artificial neural network and deep learning

The artificial neural network (ANN) is a subset of machine learning methods inspired by a biological neural network that transfers and processes information. The ANN comprises several interconnected artificial neurons, known as nodes or process elements, which are structured in at least three layers: input, hidden, and output layers (Figure 1). Each neuron in one layer connects to all neurons in another layer. The strength of connections between neurons is weighted based on the performance in a training process. Deep learning is a subset of the artificial neural network, which contains more than one hidden layer. Although many types of deep learning have been developed, the most commonly used and known is the convolutional neural network (CNN), in which a convolutional operation filters informative data through piles of information layers.

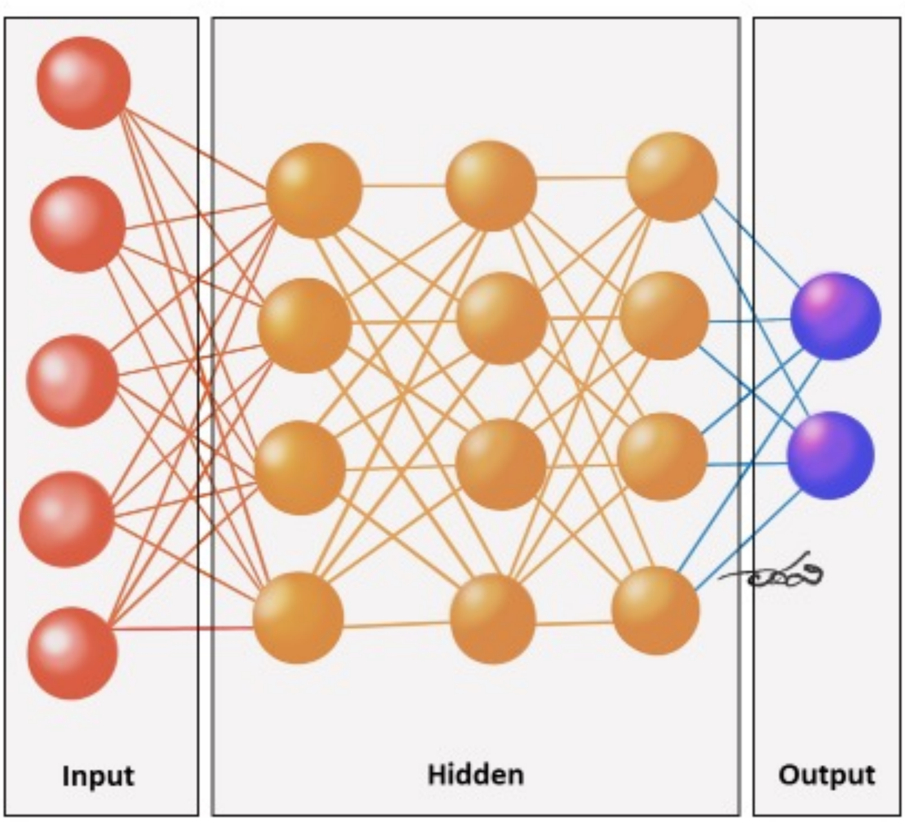

Figure 1. *Schematic presentation of an artificial neural network; a spherical shape refers to one process element, also known as a node or neuron. Nodes are structured into three main layers: input, hidden, and output layers; and each node connects to all nodes in another layer.*

Current applications of machine learning in medical radiology

The application of AI in medicine has notably increased, particularly in medical radiology, including diagnostic radiology, radiotherapy, and oncology, as well as interventional radiology. In diagnostic radiology, AI assists in disease detection, segmentation, diagnosis, and monitoring during follow-up or post-treatment. In the fields of radiotherapy and oncology, AI plays additional roles in treatment planning, outcome prediction, and advanced techniques in radiotherapy and chemotherapy for cancer [11-15]. AI also supports therapeutic radiation dose optimization in oncology and interventional radiology. In interventional radiology, AI is involved in recognizing and diagnosing diseases in medical imaging, providing intraoperative guidance, and conducting postoperative assessments, including in oncologic interventions, neurologic interventions, interventional cardiology, and robotic-supported interventional procedures [16]. AI also aids in patient registration for imaging and treatment, scheduling, appointment management, queue management, and organization during follow-up. The applications of AI in medical radiology have been described and highlighted based on radiology workflow from patient registration to radiological reports (Figure 2) [17, 18].

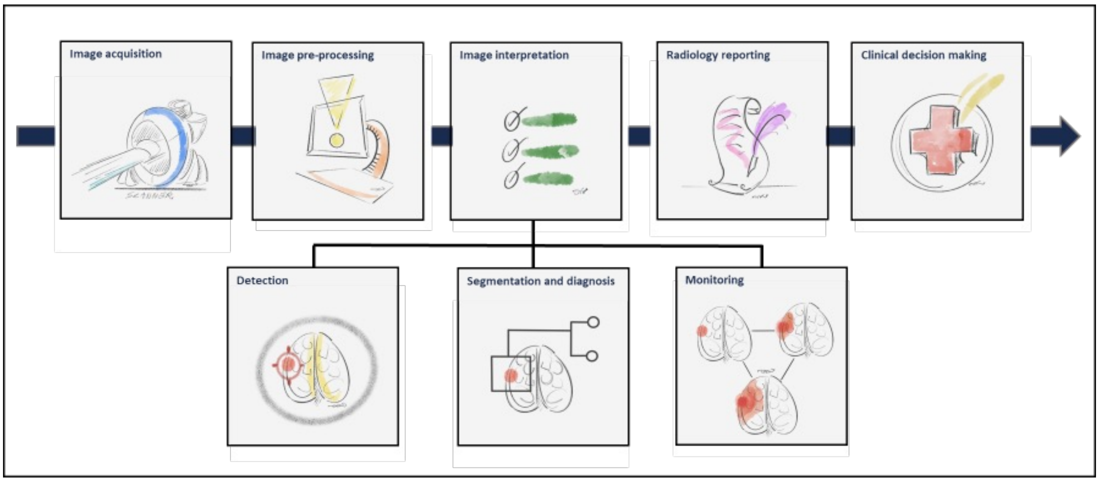

Figure 2. *Artificial intelligence implemented in radiology workflow (this figure is modified from Figure 3 in a review by Hosny et al. [17]).*

Patient schedule for radiological follow-up

Machine learning is implemented in patient-scheduling programs to reduce the number of patients who lose radiological follow-up. Machine learning has been used to determine an individual's risk of missing radiological care, following which a patient care team develops an individual solution to reduce the chance of loss of follow-up [19]. AI has been employed to analyze patient information and clinical data, as well as radiologist schedules and scanner availability. This enables the provision of optimized scheduling for patients during follow-up, thereby reducing waiting time [13, 20, 21].

Image acquisition

Deep learning has been used in image reconstruction that enhances mapping between machine sensors and images. Indeed, deep learning has outperformed conventional acquisition methods in terms of noise tolerance and artifact reduction [22]. Many studies have utilized deep learning to reduce artifacts in digital subtraction angiography (DSA), computed tomography (CT), and magnetic resonance imaging (MRI) [16, 23-31]. These studies have shown that deep learning techniques significantly improve diagnostic quality by effectively reducing artifacts and shortening image acquisition time. In the field of radio-oncology, deep learning methods are employed to reconstruct CT images from cone beam CT, resulting in noise reduction, enhanced image quality, and reduced radiation doses [32-35]. In addition, AI methods have been used to solve the problem of missing data from CT scans, in cases where a scanner cannot perform full rotations of the target objects. CNN has also been used to correct the artifact problem in CT using a combination of original and corrected image information to reduce metal artifacts [36].

Image pre-processing

Selected similarity criteria and reference images can bias the interpretation of radiological images. Deep learning allows us to achieve better motion compensation for sequential images and better handling of complex tissue deformations [17]. The multimodal ability in deep learning methods also allows for multiple quantitative measures of several imaging modalities, which thus improves the accuracy of image assessment [37]. For example, the application of multimodal imaging in oncologic evaluation has enabled the combination of various quantitative functional measurements, as seen in positron emission tomography (PET) scans and single-photon emission computed tomography (SPECT) imaging. This approach enhances the precision of tumor characterization and assessment [17, 38].

Image interpretation: detection, characterization and monitoring

Detection is a basic task used to identify a suspicious abnormality in medical images. While radiologists use cognitive skills to confirm or reject their hypotheses based on their knowledge and experiences, machine learning employs pre-defined rule-based programs or the recognition of abnormal data patterns from images. Rule-based CADe has been criticized mostly in terms of false positives which reduce radiologists' acceptability. Although machine learning-based CADe remains susceptible to false-positive results, it has demonstrated comparable predictive performance when used by radiologists. Breast cancer and lung cancer are the main fields that have been investigated with machine learning [39]. A breast cancer screening program has been implemented in the United States as a second radiologist or pre-screening process to reduce radiologists' workload and increase medical access for patients. Regarding lung cancer, machine learning has also been used to detect abnormal lymph nodes, which may be a sign of metastases. It has been demonstrated that the performance of machine learning-based CADe is comparable to that of radiologists. In addition, there is evidence demonstrating that the use of machine learning as a second radiologist provides more accurate results compared with either machine learning or radiologists alone [40-42].

Characterization refers to a task covering the segmentation and diagnosis of radiological images. While segmentation is used to identify the margins of abnormal areas in images, diagnosis is employed to estimate the probability that the specific conditions are present or absent. Probabilistic Atlas software uses machine learning algorithms to demarcate ill-defined image pixel intensity and locate abnormalities in radiological images, such as the segmentation of gliomas from a brain MRI and the estimation of prostate volume based on a prostate MRI [43, 44].

To provide examples of applying AI in detection, classification, and monitoring within musculoskeletal radiology, machine learning tools have been developed to assist radiologists in detecting fractures related to trauma on radiographs and CT scans, as well as detecting knee cartilage lesions on MRIs in osteoarthritis cases [45]. For characterization, AI assists radiologists in grading tumors such as osteosarcoma and soft tissue sarcoma on CT and MRI. AI is also used to classify post-operative instruments, such as spinal hardware or shoulder arthroplasty components. Additionally, AI monitors implant-related complications from plain radiographs and MRIs in cases of knee or hip arthroplasty loosening [45-47]. AI assists in the measurement of body composition, including skeletal muscle parameters and adipose tissue distribution, to predict survival outcomes and adverse events in cancer patients—a growing trend in contemporary oncological research [48, 49]. Figure 3 demonstrates the application of AI in segmenting skeletal muscle areas and adipose tissue from CT slices at the third lumbar vertebral level (L3) to assess sarcopenia and quantify visceral, subcutaneous, and intramuscular fat deposits in cancer patients for survival prediction. These examples illustrate the significant potential of AI applications in enhancing the accuracy and efficiency of musculoskeletal radiology. As AI continues to evolve, its integration into clinical practice will likely expand, offering further advancements in patient care.

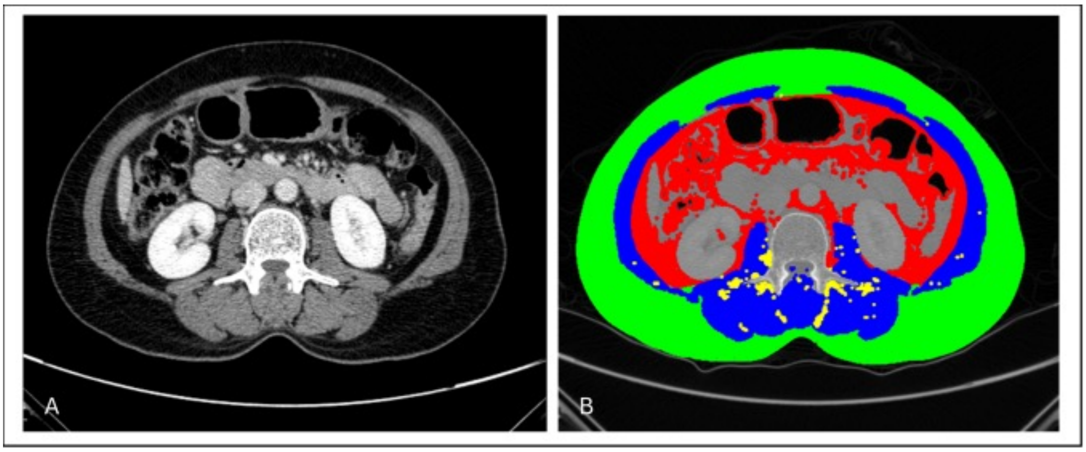

Figure 3. *Body composition analysis using CT imaging; (A) Axial CT image at the L3 vertebral level (B) Color-coded segmentation map depicting different tissue components: skeletal muscle area (blue), subcutaneous adipose tissue (green), visceral adipose tissue (red), and intramuscular adipose tissue (yellow).*

Radiology reporting

Radiology reports are a key tool for communication between radiologists and other professionals. These reports are created in various formats depending on the radiologist making the report. As such, it is a challenge to generate a standardized pattern, which is a benefit in terms of quality control and standard communication. Al could enable this task to generate uniform and standardized radiology reports. Radiological images can be transformed into natural language processing and matching with the narrative radiology reports [50]. This allows machine learning to extract radiological reports for quality improvement and future analysis. In addition, machine learning could be linked to radiologists' recommendations, thus reducing the loss of communication and follow-up [51].

The development of AI can lead to a decrease in mistakes in radiology reports. For example, errors such as reporting the wrong anatomical structures, like identifying a prostate in a female patient or a uterus and ovaries in a male patient, can be reduced. Another common issue is reporting a lesion on the wrong side; the lesion may be on one side in the findings section, but the radiologist might mention it on the other side in the impression section [52]. In some countries, such as Thailand, radiologists often type reports in English, which is not their mother tongue. This can lead to misspellings, inappropriate grammar, and irrelevant sentences and phrases within the same report. The developed AI can assist radiologists in reducing these reporting problems.

Another challenge for AI is assisting in the longitudinal reporting of lesions, especially in oncologic cases. A crucial task is comparing lesions over the follow-up period. Complex cases with multiple lesions can be time-consuming and tedious. AI can simplify this complexity by structuring and organizing the sequence of measurements and comparisons of changes in serial follow-up images over time, making the process easier [52].

Challenges of machine learning in medical radiology

Data for developing machine learning

The development of machine learning-based systems requires not only a large data set but also high-quality data. The amount of data required for the development of machine learning-based systems depends on the tasks. If the task is specific, such as a segmentation task, the required data set is relatively small compared with that needed for complex classification tasks.

Apart from data quantity, machine learning also needs high data quality to avoid inaccurate models. Radiological images used in the same machine-learning task should have low heterogeneity in data quality. The data should be produced using standardized imaging processes and imaging protocols. Data curating also requires a standardized set of criteria that is specific to a machine learning task, and data storing needs to be managed systematically, which enables future data access. Moreover, labeled data should be created according to standardized and generally accepted diagnostic criteria.

AI has been developed to enhance radiology reports by making them more concise, patient-friendly, and tailored with specific recommendations for each individual. Research has demonstrated that AI improves both the quality of reports and the efficiency of radiologists' workflows [53]. Recent advancements use the Natural Language Processing (NLP) tools and AI techniques to annotate, summarize, and extract key findings from these reports [52, 54]. Since radiology reports are often written in unstructured free text, they can be challenging to read, extract data from, and utilize effectively. Structured reports, on the other hand, are preferred because they offer standardization, completeness, and easier information retrieval. To train AI systems to convert unstructured reports into structured formats, a large dataset is necessary. The process involves meticulous preprocessing, entity recognition, manual annotation by domain experts, and data normalization. This approach not only ensures accuracy and reliability but also uses medical ontologies for standardization. By implementing validation steps such as inter-annotator agreement and expert reviews, the resulting structured data provides a solid foundation for training advanced NLP models. This methodology significantly enhances the development of AI tools that can improve the accuracy, efficiency, and overall quality of radiological diagnostics and patient care.

Model performance

Machine learning is developed based on existing data or training data without an explicit model assumption, as is the case with conventional statistics. As a result, machine learning is considerably dependent on the quality and amount of training data. If training data contains considerable random noise, the model is fitted to unnecessary information and provides poor model accuracy with new data. In addition, as a complex model that is still developing, machine learning is prone to be overfitted, in which machine learning algorithms are too fitted with the training data and perform very inaccurately with new data that models have not met before. This drastically reduces the value of the model in terms of generalisability.

There are many metrics used to evaluate the performance of AI algorithms in medical radiology. Accuracy, sensitivity, specificity, overlap-based metrics, distance metrics, and data quality are some of the well-known metrics [55]. However, there is no single, universally accepted metric for evaluating AI model performance. Given these challenges, regulatory standards, protocols, and best practices are crucial for AI implementation. Organizations should actively work to combine data science skills with the pertinent areas of drug development and safety monitoring. In Thailand, the Thailand Food and Drug Administration (TFDA) has not approved any machine learning or AI in use in the field of Radiology. The European Medicines Agency (EMA), a key agency of the European Union (EU) responsible for the scientific evaluation, supervision, and safety monitoring of medicines, has released a Reflection Paper on the use of AI in the medicinal product lifecycle. This paper aims to initiate dialogues with all stakeholders in this rapidly evolving field [56]. The EMA emphasizes high accuracy, sensitivity, and specificity for AI models used in clinical settings. Specific ranges are defined based on the use case and risk classification of the AI application. The Food and Drug Administration (FDA) of the United States has approved the use of machine learning and AI in medicine and radiology. The trend of these approvals has increased exponentially over the past decades [57]. Although AI has received approvals for use in radiology, its application in daily practice must be approached with caution. There have been reports of misinterpretations involving AI in radiologic images. Additionally, many radiologists are reluctant to use AI tools because they are concerned about the reliability of predictions, especially when the tool was tested on retrospective data but is now being used for prospective data [57].

AI has a significant potential to revolutionize radiology practice, but specific metrics are necessary to objectively measure its impact. The promises surrounding AI have been substantial, claiming to enhance technical performance, improve the detection and quantification of pathologies, streamline radiologists' workflows, and ultimately improve patient outcomes [18, 58-60].

Integration into the radiologists' workflow

AI has gradually refined the traditional roles of radiologists and integrated itself into radiology practice, becoming an integral part of every aspect of the radiologist's workflow. In scheduling, AI assists in patient list management, reducing patient waiting time and optimizing scan queues. During scanning, AI helps select optimized procedures and processes to reduce radiation doses [61]. Image quality from various imaging modalities has improved with AI, which also reduces scan times [13, 20, 21]. Radiologists benefit from AI in detecting abnormalities, interpreting images, and writing radiology reports.

In the field of radio-oncology, deep learning approaches are used to reconstruct CT images from cone beam CT, providing noise reduction, improved image quality, and reduced radiation doses [32-35]. AI also assists radio-oncologists in treatment planning and offers advanced techniques in radiotherapy and chemotherapy [11-15, 17]. Additionally, AI supports interventional radiologists in recognizing and diagnosing diseases in medical imaging, offering intraoperative guidance, and conducting postoperative assessments [16]. Furthermore, AI aids clinicians in clinical decision-making by helping patients choose treatment options based on diagnosis, outcome prediction, complication forecasting, and treatment efficacy.

AI also helps in scheduling follow-up scans, tracking disease progress by comparing previous images, predicting outcomes, and evaluating treatment responses across various modalities, including radiotherapy, chemotherapy, surgery, medication, and intervention [20].

Furthermore, AI's integration into radiology practice represents a transformative shift in medical imaging and treatment methodologies. By automating and optimizing numerous tasks, AI not only enhances the efficiency and accuracy of radiologists but also significantly improves patient outcomes. Its applications in oncological and interventional radiology demonstrate its versatility and potential to revolutionize these fields. As AI technology continues to advance, its ability to support and augment the capabilities of healthcare professionals will undoubtedly lead to more precise diagnoses, personalized treatment plans, and overall better healthcare delivery. The ongoing development and implementation of AI in radiology promise a future where medical imaging and intervention are more effective, efficient, and accessible to patients worldwide.

Regulation and ethical issues

The regulation of AI in medicine is rapidly evolving. In addition, the evaluation of AI for approval is difficult due to the nature of the machine, i.e. it is learning and developing from the existing training data. Thus, the evaluation should be performed in a timely and regular manner to remain up to date [62, 63].

Data security is another issue, as the data required for machine learning is big data taken from patients' medical records. The data resource should be legal and well-known. Patients have a right to decide how their data is to be used. To use patient data in developing machine learning systems, we must obtain informed patients.

A common question is who should take responsibility and accountability for the data used and developed in machine learning. If data belongs to model developers, and in the case of data hacking, who should have a role in data protection? In case the machine provides an incorrect result, who will take responsibility for the mistake? Program developers and designers are one of the options, but clinicians and radiologists might also be involved in this responsibility.

Future of machine learning in medical radiology

The aims of the next-generation machine learning-based systems in medical radiology have been suggested as follows: improving radiologists' performance, saving time, ensuring cost-effectiveness, and integration with the radiologists' workflow [64].

The use of machine learning will be broadened not only with cancers but also with chronic and degenerative diseases such as Alzheimer's disease [17]. In addition to their detection role, machine learning-based clinical decision support systems (CDSS) might be used in a way similar to self-driving cars. This would reduce radiologists' workloads and time spent in terms of integrating clinical information and communicating with multidisciplinary teams to improve patients' outcomes. Machine learning-based CDSS will be very helpful in primary care settings, where clinicians have less experience in medical radiology [64]. This also allows improved access to medical imaging for patients in the primary care setting with less relatively increased workloads for radiologists.

Machine learning could be implemented into the radiologists' workflow in multiple tasks which are relatively routine works. Radiologists will still play a vital role in all decision-making regarding radiology fields and patient care. They will employ a part of machine learning systems to ensure that radiological reports are judicious and transparent. This also results in legal liability, as the decisions are made by human initiation.

In terms of CDSS development, unsupervised machine learning would become more useful in routine practice due to the massive number of data inputs lacking standardized labeled data [13]. Fully anonymized patient data could be shared on a large cloud platform to develop machine learning-based models that are more generalizable [65]. In addition, machine learning could be linked together across imaging modalities to improve the accuracy of diagnosis.

Regarding steps for the implementation of machine learning in medical radiology, these have been mentioned in a previous study [42]. It should start with setting up an implementation team consisting of experts from multiple disciplines (informatics officer, healthcare manager, and radiologist teams) and assigning jobs to each member. The team members will be given the jobs of Chief Informatics Officer (CIO), radiology committee, and individual radiologists. The CIO will take responsibility for safeguarding the use of data. The team in general will also manage other data governance issues. In addition, the CIO must ensure that newly implemented models are compatible with existing infrastructure and programs, such as picture archiving, the communication system (PACS), and Radiology Information Systems (RIS). The radiology committee will be responsible for creating a framework of machine learning throughout the radiologist's workflow and also for ensuring the seamless integration of this framework into the workflow. The committee will be responsible for clinical governance including the development of standards for the radiology service. Individual radiologists will be invited to participate in the development process and evaluation of clinical and radiological information governance using machine learning-based CDSS.

Preparation for integration of machine learning

Medical education in the machine learning age

In terms of education in AI for radiologists, they must understand the foundations of AI and its applications as both developers and end users. Radiologists must also understand the principle of the techniques applied in AI as well as the data used to develop it. In an ideal scenario, the radiologist will be in a team establishing how AI can be applied based on evidence-based medicine. As a result, they should be trained in the clinical relevance and applicability of AI, in addition to the principle of how AI functions. Radiologists should appraise whether the application of AI is reliable and if it has meaning in terms of clinical practice. Additionally, the results from the AI-assisted system can be explained in terms of knowledge of clinical pathophysiology knowledge.

In addition, data protection and ethical issues related to AI development and its application should be taught in a radiology residency program. Radiologists produce medical images which are a type of personal medical data. Therefore, they should take responsibility for future data use and data protection. This training would need to provide a framework for radiologists to inform patients that their data is being used to advance AI applications, or that the patient's diagnosis partially originates from AI-assisted systems. Global healthcare databases will gather other clinical data. This will be a significant opportunity for radiologists to take part and prepare themselves in the creation and analysis of combined big data [21].

AI training in radiology residency programs should be started as early as possible. Continuing medical education should also be promoted to update AI involving applications that rapidly develop and change.

Future roles of radiologists after the implementation of machine learning

Here we explore the role of radiologists in the future after machine learning is integrated into their workflow. First of all, we have to accept that, in the foreseeable future, machine learning will not be able to replace radiologists, who use both knowledge and experience in decision-making in order to form accurate clinical judgments. Radiologists' tasks are much more complex than interpreting medical images. They use both data analysis and interpretation, as well as decision-making which employs not only data from radiology but also clinical data, and patient preferences; moreover, these radiologists rely on their trainings from medical schools and experiences from work they have already carried out. However, radiologists have to adapt their roles beyond the interpretation of medical images. Radiologists must act in more of a clinician role, applying their clinical knowledge in answering diagnostic questions and guiding decision-making. In addition, radiologists should maintain their presence in clinical pathways, considering clinical, personal, and societal contexts in ways that AI alone is not able to replicate.

Current artificial neural networks have accuracy rates that surpass those of human radiologists in narrow-based tasks [66, 67]. It is impossible to exclude the possibility that the efficiency gain provided by AI may lead to a need for fewer radiologists. However, the roles of radiologists will expand as they become more connected to technology and have access to better tools. Radiologists may play a pivotal role in the identification of clinical applications where AI may make a difference. Radiologists could also play a crucial role in data interpretation, cooperating with data scientists in defining clinically useful results. Radiologists should negotiate the supply of these valuable data sets and clinical knowledge while playing a guiding role in the clinical application of AI programs. Creating this kind of "multidisciplinary AI team" will help to ensure that patient safety standards are met and will make the radiologist's responsibilities transparent to patients and regulatory authorities.

Discussion

The integration of machine learning into medical radiology has the potential to significantly enhance diagnostic accuracy, streamline workflows, and improve patient outcomes. Over recent decades, advancements in machine learning have led to its widespread application in various aspects of radiology, including disease detection, image analysis, and radiology reporting. These technologies offer promising solutions to address the increasing demands on radiologists and the growing complexity of medical imaging.

However, the successful integration of machine learning into clinical practice is not without challenges. Issues related to data quality, model performance, and regulatory considerations need to be addressed to fully realize the benefits of these technologies. Ensuring that machine learning systems are robust, reliable, and ethically sound is crucial for their effective implementation in routine radiological practice.

Future developments in machine learning are likely to continue transforming the field of radiology. As technology evolves, there will be increased opportunities for enhancing diagnostic capabilities, optimizing patient care, and refining clinical decision-making processes. Radiologists will need to adapt to these changes by acquiring new skills and embracing the evolving role of machine learning in their practice.

Preparing for the future integration of machine learning involves not only understanding the principles and applications of these technologies but also addressing regulatory, ethical, and educational aspects. By fostering collaboration among radiologists, data scientists, and policymakers, and by investing in ongoing education and training, the medical community can ensure that machine learning contributes positively to the advancement of medical radiology.

In summary, while machine learning presents transformative opportunities for medical radiology, careful consideration of its implementation and continuous evaluation of its impact will be essential to harness its full potential and improve patient care.

References

1. O'Sullivan JW, Stevens S, Hobbs FDR, Salisbury C, Little P, Goldacre B, et al. Temporal trends in use of tests in UK primary care, 2000-15: retrospective analysis of 250 million tests. BMJ 2018;363:k4666. doi: 10.1136/bmj.l444.

2. Smith-Bindman R, Miglioretti DL, Larson EB. Rising use of diagnostic medical imaging in a large integrated health system. Health Aff (Millwood) 2008; 27:1491–502. doi: 10.1377/hlthaff.27.6.1491.

3. Rimmer A. Radiologist shortage leaves patient care at risk, warns royal college. BMJ 2017;359:j4683. doi: 10.1136/bmj.j4683.

4. Savadjiev P, Chong J, Dohan A, Vakalopoulou M, Reinhold C, Paragios N, et al. Demystification of AI-driven medical image interpretation: past, present and future. Eur Radiol 2019;29:1616–24. doi: 10.1007/s00330-018-5674-x.

5. Howell MD, Corrado GS, DeSalvo KB. Three epochs of artificial intelligence in health care. JAMA 2024;331:242- 4. doi: 10.1001/jama.2023.25057.

6. Doi K. Computer-aided diagnosis in medical imaging: historical review, current status and future potential. Comput Med Imaging Graph 2007;31:198–211. doi: 10.1016/j.compmedimag.2007.02.002.

7. Chen CM, Chou YH, Tagawa N, Do Y. Computer-aided detection and diagnosis in medical imaging. Comput Math Methods Med 2013;2013:790608. doi: 10.1155/2013/790608

8. Castellino RA. Computer-aided detection (CAD): an overview. Cancer Imaging 2005;5:17–9. doi: 10.1102/1470-7330.2005.0018.

9. Wang S, Summers RM. Machine learning and radiology. Med Image Anal 2012 ;16:933–51. doi: 10.1016/j.media.2012.02.005.

10. Deo RC. Machine learning in medicine. Circulation 2015;132:1920–30. doi: 10.1161/CIRCULATIONAHA.115.001593.

11. Khajuria R, Sarwar A. Review of reinforcement learning applications in segmentation, chemotherapy, and radiotherapy of cancer. Micron 2024;178: 103583. doi: 10.1016/j.micron.2023.103583.

12. Howard FM, Kochanny S, Koshy M, Spiotto M, Pearson AT. Machine learning-guided adjuvant treatment of head and neck cancer. JAMA Netw Open 2020;3:e2025881. doi: 10.1001/jamanetworkopen.2020.25881.

13. Xie L, Xu D, He K, Tian X. Machine learning-based radiotherapy time prediction and treatment scheduling management. J Appl Clin Med Phys 2023;24:e14076. doi: 10.1002/acm2.14076.

14. Li T, Wang J, Yang Y, Glide-Hurst CK, Wen N, Cai J. Multi-parametric MRI for radiotherapy simulation. Med Phys 2023;50:5273–93. doi: 10.1002/mp.16256.

15. Fechter T, Sachpazidis I, Baltas D. The use of deep learning in interventional radiotherapy (brachytherapy): A review with a focus on open source and open data. Z Med Phys 2024;34:180–96. doi: 10.1016/j.zemedi.2022.10.005.

16. Zhang J, Fang J, Xu Y, Si G. How AI and robotics will advance interventional radiology: narrative review and future perspectives. Diagnostics 2024 ;14:1393. doi: 10.3390/diagnostics14131393.

17. Hosny A, Parmar C, Quackenbush J, Schwartz LH, Aerts HJWL. Artificial intelligence in radiology. Nat Rev Cancer 2018;18:500–10. doi: 10.1038/s41568-018-0016-5.

18. Choy G, Khalilzadeh O, Michalski M, Do S, Samir AE, Pianykh OS, et al. Current applications and future impact of machine learning in radiology. Radiology 2018 ;288:318–28. doi: 10.1148/radiol.2018171820.

19. Marella WM, Sparnon E, Finley E. Screening electronic health record–related patient safety reports using machine learning. J Patient Saf 2017;13:31–6. doi: 10.1097/PTS.0000000000000104.

20. Najjar R. Redefining radiology: a review of artificial intelligence integration in medicaliImaging. Diagnostics (Basel) 2023;13:2760. doi: 10.3390/diagnostics 13172760.

21. SFR-IA Group, CERF, French Radiology Community. Artificial intelligence and medical imaging 2018: French Radiology Community white paper. Diagn Interv Imaging 2018 ;99:727–42. doi: 10.1016/j.diii.2018.10.003.

22. Zhu B, Liu JZ, Cauley SF, Rosen BR, Rosen MS. Image reconstruction by domain-transform manifold learning. Nature 2018;555:487–92. doi: 10.1038/nature25988.

23. Gao Y, Song Y, Yin X, Wu W, Zhang L, Chen Y, et al. Deep learning-based digital subtraction angiography image generation. Int J Comput Assist Radiol Surg 2019 ;14:1775–84. doi: 10.1007/s11548-019-02040-x.

24. Nagayama Y, Emoto T, Kato Y, Kidoh M, Oda S, Sakabe D, et al. Improving image quality with super-resolution deep-learning-based reconstruction in coronary CT angiography. Eur Radiol 2023;33:8488–500. doi: 10.1007/s00330-023-09888-3.

25. Zhang J, Gong W, Ye L, Wang F, Shangguan Z, Cheng Y. A Review of deep learning methods for denoising of medical low-dose CT images. Comput Biol Med 2024 ;171:108112. doi: 10.1016/j.compbiomed.2024.108112.

26. Fujita N, Yasaka K, Katayama A, Ohtake Y, Konishiike M, Abe O. Assessing the effects of deep learning reconstruction on abdominal CT without arm elevation. Can Assoc Radiol J 2023;74:688–94. doi: 10.1177/08465371231169672.

27. Wang T, Yu H, Wang Z, Chen H, Liu Y, Lu J, et al. SemiMAR: semi-supervised learning for CT metal artifact reduction. IEEE J Biomed Health Inform 2023 ;27:5369–80. doi: 10.1109/JBHI.2023.3312292.

28. Man C, Lau V, Su S, Zhao Y, Xiao L, Ding Y, et al. Deep learning enabled fast 3D brain MRI at 0.055 tesla. Sci Adv 2023;9:eadi9327. doi: 10.1126/sciadv.adi9327.

29. Safari M, Eidex Z, Chang CW, Qiu RLJ, Yang X. Fast MRI reconstruction using deep learning-based compressed sensing: A systematic review. arXiv: 2405.00241v1 [Preprint]. 2024 [cited 2024 Dec 17]. Available from: https://arxiv.org/abs/2405.00241.

30. Wessling D, Gassenmaier S, Olthof SC, Benkert T, Weiland E, Afat S, et al. Novel deep-learning-based diffusion weighted imaging sequence in 1.5 T breast MRI. Eur J Radiol 2023;166:110948. doi: 10.1016/j.ejrad.2023.110948.

31. Xie Y, Tao H, Li X, Hu Y, Liu C, Zhou B, et al. Prospective comparison of standard and deep learning-reconstructed turbo spin-echo MRI of the shoulder. Radiology 2024 ;310:e231405. doi: 10.1148/radiol.231405.

32. Cui Z, Fang Y, Mei L, Zhang B, Yu B, Liu J, et al. A fully automatic AI system for tooth and alveolar bone segmentation from cone-beam CT images. Nat Commun 2022;13:2096. doi: 10.1038/s41467-022-29637-2.

33. Rusanov B, Hassan GM, Reynolds M, Sabet M, Kendrick J, Rowshanfarzad P, et al. Deep learning methods for enhancing cone-beam CT image quality toward adaptive radiation therapy: A systematic review. Med Phys 2022; 49:6019–54. doi: 10.1002/mp.15840.

34. Zhang Y, Huang X, Wang J. Advanced 4-dimensional cone-beam computed tomography reconstruction by combining motion estimation, motion-compensated reconstruction, biomechanical modeling and deep learning. Vis Comput Ind Biomed Art 2019;2:23. doi: 10.1186/s42492-019-0033-6.

35. Szczykutowicz TP, Toia GV, Dhanantwari A, Nett B. A Review of deep learning CT reconstruction: concepts, limitations, and promise in clinical practice. Curr Radiol Rep 2022;10:101–15. doi: 10.1007/s40134-022-00399-5

36. Muller B, Wang G, editors. Developments in X-Ray tomography XI. Proceedings volume 10391. SPIE optical engineering application; 2017 Aug 6-10; San Diego, California, United State. Bellingham (WA): SPIE Digital Library; 2024 [cited 2024 Dec 17]. Available from: https://www.spiedigitallibrary.org/conference-proceedings-of-spie/10391.toc?webSyncID=7a434259-d750-205b-5837-e5e3b52e1a93&sessionGUID=a61b9741-6734-4428-b5d6-4bb0bbb9456a37.

37. Yankeelov TE, Abramson RG, Quarles CC. Quantitative multimodality imaging in cancer research and therapy. Nat Rev Clin Oncol 2014;11:670–80. doi: 10.1038/nrclinonc.2014.134.

38. Jimenez-Mesa C, Arco JE, Martinez-Murcia FJ, Suckling J, Ramirez J, Gorriz JM. Applications of machine learning and deep learning in SPECT and PET imaging: General overview, challenges and future prospects. Pharmacol Res 2023;197:106984. doi: 10.1016/j.phrs.2023.106984.

39. Pesapane F, Codari M, Sardanelli F. Artificial intelligence in medical imaging: threat or opportunity? Radiologists again at the forefront of innovation in medicine. Eur Radiol Exp 2018;2:35. doi: 10.1186/s41747-018-0061-6.

40. Shiraishi J, Li Q, Appelbaum D, Doi K. Computer-aided diagnosis and artificial intelligence in clinical imaging. Semin Nucl Med 2011;41:449–62. doi: 10.1053/j.semnuclmed.2011.06.004.

41. Zhang J, Wang Y, Yu B, Shi X, Zhang Y. Application of computer-aided diagnosis to the sonographic evaluation of cervical lymph nodes. Ultrason Imaging 2016;38:159–71. doi: 10.1177/0161734615589080.

42. Liew C. The future of radiology augmented with artificial intelligence: A strategy for success. Eur J Radiol 2018;102:152–6. doi: 10.1016/j.ejrad.2018.03.019.

43. Parisot S, Darlix A, Baumann C, Zouaoui S, Yordanova Y, Blonski M, et al. A probabilistic atlas of diffuse WHO grade II glioma locations in the brain. PLoS One 2016;11:e0144200. doi: 10.1371/journal.pone.0144200.

44. Pejavar S, Yom SS, Hwang A, Speight J, Gottschalk A, Hsu IC, et al. Computer-assisted, atlas-based segmentation for target volume delineation in whole pelvic IMRT for prostate cancer. Technol Cancer Res Treat 2013;12:199–206. doi: 10.7785/tcrt.2012.500313.

45. Gitto S, Serpi F, Albano D, Risoleo G, Fusco S, Messina C, et al. AI applications in musculoskeletal imaging: a narrative review. Eur Radiol Exp 2024;8:22. doi: 10.1186/s41747-024-00422-8.

46. Lacroix M, Aouad T, Feydy J, Biau D, Larousserie F, Fournier L, et al. Artificial intelligence in musculoskeletal oncology imaging: A critical review of current applications. Diagn Interv Imaging 2023;104:18–23. doi: 10.1016/j.diii.2022.10.004.

47. Park CW, Oh SJ, Kim KS, Jang MC, Kim IS, Lee YK, et al. Artificial intelligence-based classification of bone tumors in the proximal femur on plain radiographs: System development and validation. PLoS One 2022;17:e0264140. doi: 10.1371/journal.pone.0264140.

48. Pakdee W, Laohawiriyakamol T, Tanutit P, Laohawiriyakamol S, Liabsuetrakul T. Association of body composition and survival in patients with locally advanced breast cancer: a historical cohort study. Acta Radiol 2024;65:575–87. doi: 10.1177/02841851241241528.

49. Anjanappa M, Corden M, Green A, Roberts D, Hoskin P, McWilliam A, et al. Sarcopenia in cancer: Risking more than muscle loss. Tech Innov Patient Support Radiat Oncol 2020 ;16:50–7. doi: 10.1016/j.tipsro.2020.10.001.

50. Sevenster M, Buurman J, Liu P, Peters JF, Chang PJ. Natural language processing techniques for extracting and categorizing finding measurements in narrative radiology reports. Appl Clin Inform 2015;6:600–10. doi: 10.4338/ACI-2014-11-RA-0110.

51. Oliveira L, Tellis R, Qian Y, Trovato K, Mankovich G. Follow-up recommendation detection on radiology reports with incidental pulmonary nodules. Stud Health Technol Inform 2015;216:1028.

52. Bizzo BC, Almeida RR, Alkasab TK. Artificial intelligence enabling radiology reporting. Radiol Clin North Am 2021;59:1045–52. doi: 10.1016/j.rcl.2021.07.004.

53. Park J, Oh K, Han K, Lee YH. Patient-centered radiology reports with generative artificial intelligence: adding value to radiology reporting. Sci Rep 2024;14: 13218. doi: 10.1038/s41598-024-63824-z.

54. C. Pereira S, Mendonça AM, Campilho A, Sousa P, Teixeira Lopes C. Automated image label extraction from radiology reports — A review. Artif Intell Med 2024;149:102814. doi: 10.1016/j.artmed.2024.102814.

55. Erickson BJ, Kitamura F. Magician's Corner: 9. Performance metrics for machine learning models. Radiol Artif Intell 2021;3:e200126. doi: 10.1148ryai. 2021200126.

56. European Medicines Agency [Internet]. Amsterdam: The Agency; c1995 - 2024 [cited 2024 Jul 29]. The use of artificial intelligence (AI) in the medicinal product lifecycle. Available from: https://www.ema.europa.eu/en/use-artificial-intelligence-ai-medicinal-product-lifecycle.

57. Zhang K, Khosravi B, Vahdati S, Erickson BJ. FDA review of radiologic AI algorithms: Process and challenges. Radiology 2024;310:e230242. doi: 10.1148/radiol.230242.

58. Thrall JH, Li X, Li Q, Cruz C, Do S, Dreyer K, et al. Artificial intelligence and machine learning in radiology: opportunities, challenges, pitfalls, and criteria for success. J Am Coll Radiol 2018;15(3 Pt B):504–8. doi: 10.1016/j.jacr.2017.12.026.

59. Gallix B, Chong J. Artificial intelligence in radiology: who's afraid of the big bad wolf? Eur Radiol 2019;29:1637–9. doi: 10.1007/s00330-018-5995-9.

60. Mayo RC, Leung JWT. Impact of artificial intelligence on women's imaging: cost-benefit analysis. AJR Am J Roentgenol 2019;212:1172–3. doi: 10.2214/AJR.18.20419.

61. Brady SL. Implementation of AI image reconstruction in CT-how is it validated and what dose reductions can be achieved. Br J Radiol 202396:20220915. doi: 10.1259/bjr.20220915.

62. Pesapane F, Volonté C, Codari M, Sardanelli F. Artificial intelligence as a medical device in radiology: ethical and regulatory issues in Europe and the United States. Insights Imaging 2018;9:745–53. doi: 10.1007/s13244-018-0645-y.

63. Jaremko JL, Azar M, Bromwich R, Lum A, Alicia Cheong LH, Gibert M, et al. Canadian Association of Radiologists white paper on ethical and legal issues related to artificial intelligence in radiology. Can Assoc Radiol J 2019;70:107–18. doi: 10.1016/j.carj.2019.03.001.

64. Mayo RC, Leung J. Artificial intelligence and deep learning – Radiology's next frontier? Clin Imaging 2018;49:87–8. doi: 10.1016/j.clinimag.2017.11.007.

65. Fazal MI, Patel ME, Tye J, Gupta Y. The past, present and future role of artificial intelligence in imaging. Eur J Radiol 2018;105:246–50. doi: 10.1016/j.ejrad.2018.06.020.

66. Wang H, Zhao T, Li LC, Pan H, Liu W, Gao H, et al. A hybrid CNN feature model for pulmonary nodule malignancy risk differentiation. J XRay Sci Technol 2018;26:171–87. doi: 10.3233/XST-17302.

67. Becker AS, Marcon M, Ghafoor S, Wurnig MC, Frauenfelder T, Boss A. Deep learning in mammography: Diagnostic accuracy of a multipurpose image analysis software in the detection of breast cancer. Invest Radiol 2017;52:434–40. doi: 10.1097/RLI.0000000000000358.

THE ASEAN JOURNAL OF RADIOLOGY
ISSN 2672-9393

ASEAN Movement in Radiology

The report from the 2024 annual meeting of thoracic radiologists in Thailand: Advancements and consensus on standards, guidelines, and practices for thoracic disorders

Chayaporn Kaewsathorn, M.D.[(1)]
Phakphoom Thiravit, M.D.[(2)]
Chayanin Nitiwarangkul, M.D.[(3)]
Thitiporn Suwatanapongched, M.D.[(3)]
Warawut Sukkasem, M.D.[(3)]
Wiwatana Tanomkiat, M.D.[(4)]
From [(1)]Department of Radiology, Surat Thani Hospital, Surat Thani, Thailand,
[(2)]Department of Radiology, Faculty of Medicine Siriraj Hospital, Mahidol University, Bangkok, Thailand,
[(3)]Department of Diagnostic and Therapeutic Radiology, Faculty of Medicine Ramathibodi Hospital, Mahidol University, Bangkok, Thailand,
[(4)]Department of Radiology, Faculty of Medicine, Prince of Songkla University, Hat Yai, Songkla, Thailand.
Address correspondence to W.T. (e-mail: twiwadha@hotmail.com)

Received 23 December 2024; accepted 23 December 2024
doi:10.46475/asean-jr.v25i3.930

Keywords: Checklist, Chronic obstructive pulmonary disease, Connective tissue disease, COPD, HRCT, Interstitial lung disease, Pod khaeng, Progressive pulmonary fibrosis, Protocol, Pulmonary cirrhosis, Screening.

Figure 1. *(A) Engaging atmosphere during the comprehensive meeting discussion (B) Group photo of the panel captured post-meeting.*

On 26 July 2024, a panel of thoracic radiology experts from across Thailand (Figure 1) convened to address key topics pertinent to thoracic diagnostic imaging within both the private and public sectors. Organized by the Royal College of Radiologists of Thailand (RCRT) in collaboration with the Foundation for Orphan and Rare Lung Disease (FORLD), the meeting took place in Asoke Conference Room on the fourth floor of Eastin Grand Hotel, Phaya Thai, Bangkok. The agenda covered five main topics:

(1) proposing a CT protocol and a report checklist for screening chronic obstructive lung disease (COPD), (2) suggesting reporting guidelines for chest imaging to screen for connective tissue disease-related interstitial lung disease (CTD-ILD), (3) revisiting the post-implementation accuracy of the proposed visual scoring method for quantifying global disease and fibrotic extents on high-resolution CT scans (HRCT), (4) establishing nationwide collaboration to define Dose Reference Levels (DRLs) for HRCT in Thailand, and (5) proposing a simple Thai terminology to educate patients about progressive pulmonary fibrosis (PPF).

Agenda 1: Proposing a CT protocol and a report checklist for screening COPD

presented by Warawut Sukkasem

According to the World Health Organization (WHO), chronic obstructive pulmonary disease (COPD) is a major public health issue of global concern and the fourth leading cause of death worldwide, causing 3.5 million deaths in 2021 [1]. While pulmonary function tests (PFTs) remain the gold standard for diagnosing Chronic Obstructive Pulmonary Disease (COPD), their use is limited in uncooperative patients or those with severe dyspnea who are unable to perform the test. CT scans offer greater sensitivity and specificity in diagnosing emphysema compared to PFTs [2]. The widespread availability of CT machines in all provincial hospitals enhances accessibility beyond that of PFTs [3]. Advances in CT technology now allow for a complete examination of the entire chest within just a few seconds, and comorbidities associated with COPD can also be demonstrated on CT scans [2]. During the meeting, a CT protocol (Figure 2) and a report checklist (Figure 3) for screening COPD were proposed.

CT Protocol for COPD

Parameter	Supine Inspiratory CT	Supine Expiratory CT	Prone Inspiratory CT **(Optional พิจารณาในรายที่สงสัย dependent density or ILA)**
IV contrast examination	Noncontrast examination	Noncontrast examination	Noncontrast examination
Respiratory phase	Full inspiration	Dynamic Forced expiration (เพื่อประเมิน TBM or EDAC และเพื่อ quantitative assessment) End-expiration (optional) (10-20 mm interval)	Full inspiration
Detector configuration	$\geq$ 16 detectors	$\geq$ 16 detectors	$\geq$ 16 detectors
Scan type, mode	Spiral (volumetric)	Spiral (volumetric)	Sequential (10-20 mm interval)
Rotation time (s)	As short as possible, usually no greater than 0.5 s	As short as possible, usually no greater than 0.5 s	As short as possible, usually no greater than 0.5 s
Pitch	Highest, $\geq$ 1	Highest, $\geq$ 1	Highest, $\geq$ 1
Acquisition collimation (mm)	$\leq$ 1 mm	$\leq$ 1 mm	$\leq$ 1 mm
Tube potential (kVp)	120	100-120	120
Tube current (mAs)	40 mAs (low dose) up to 200 mAs (moderate dose) (Automated exposure control)	40 mAs up to 60 mAs (Automated exposure control)	40 mAs up to 80 mAs (Automated exposure control)
Reconstruction for visual assessment			
Algorithm	Sharp or high frequency kernel	Sharp or high frequency kernel	Sharp or high frequency kernel
Section thickness	0.625-1 mm	0.625-1 mm	0.625-1 mm
Interval	0.5-0.9 mm	0.5-0.9 mm (Dynamic forced expiration) 10 mm (end expiration)	10 mm
Field of view (FOV)	To cover the whole lung	To cover the whole lung	Optional: lower lung zone
Reconstruction for quantitative assessment (QCT)			
Algorithm	Neutral, smooth kernel	Neutral, smooth kernel	-
Section thickness	0.625-1 mm	0.625-1 mm	-
Interval	0.5-0.9 mm	0.5-0.9 mm (Dynamic forced expiration) 10 mm (end expiration)	-
Field of view (FOV)	To cover the whole lung	To cover the whole lung	-

เอกสารอ้างอิง:

1.) Lynch DA, Austin JHM, Hogg JC, Grenier PA, Kauczor HU, Bankier AA, Barr RG, Colby TV, Galvin JR, Gevenois PA, Coxson HO, Hoffman EA, Newell JD Jr, Pistolesi M, Silverman EK, Crapo JD. CT-definable subtypes of chronic obstructive pulmonary disease: a statement of the Fleischner Society. Radiology. 2015;277(1):192-205.
2.) https://www.rcrt.or.th/hrct-protocol-และ-checklist/

Figure 2. *A proposed CT protocol for screening COPD.*

CT Report Checklist for COPD

ID(HN) ☐☐☐☐☐☐

Date of Examination (date-month-year) ☐☐-☐☐-☐☐☐☐

1. Imaging Quality ☐ Good ☐ Suboptimal ☐ Inadequate

If not good, mark the boxes that apply

☐ Not full inspiration ☐ Not full expiration ☐ Artifact ☐ Others.........

2. Parenchymal Abnormalities Consistent with COPD ☐ Yes (*Complete Section 2.1 and 2.2*) ☐ No (*Proceed to Section 3*)

2.1 Predominant Zone

	R	L
Upper	☐	☐
Middle	☐	☐
Lower	☐	☐

2.2 Major Emphysematous Phenotypes with Severity

	R	L
Centrilobular Emphysema	☐	☐
Trace (<0.5% of lung zone)	☐	☐
Mild (0.5-5% of lung zone)	☐	☐
Moderate (>5% of lung zone)	☐	☐
Confluent	☐	☐
Advanced destructive	☐	☐

	R	L
Paraseptal Emphysema	☐	☐
Mild (≤1 cm)	☐	☐
Substantial (> 1 cm and Large amount)	☐	☐
Panlobular Emphysema	☐	☐

3. Airway Abnormalities Consistent with COPD ☐ Yes (*Complete Section 3.1 and 3.2*) ☐ No (*Proceed to Section 4*)

3.1 Large Airway Disease

☐ Bronchial Wall Thickening
☐ Mucous Plugging
☐ Saber Sheath trachea

3.2 Small Airway Disease (SAD)

☐ Inflammatory SAD (Centrilobular Opacities)
☐ Obstructive SAD (Air Trapping)

4. Comorbidities

☐ Lung cancer/mass/nodule
☐ Bronchiectasis
☐ Combined Pulmonary Fibrosis with Emphysema (CPFE)
☐ Cyst/Airspace enlargement with fibrosis (AEF)/Thick-walled cystic lesion (TWCL)
☐ Tracheobronchomalacia (TBM)
☐ Excessive dynamic airway collapse (EDAC)
☐ Pulmonary infection

☐ ILA/ILD...................
☐ Giant bulla
☐ Pleural Lesion ....
☐ Enlarged main pulmonary artery
☐ Vascular/coronary calcifications
☐ Pulmonary cachexia/sarcopenia
☐ Osteoporosis/osteopenia
☐ Others ....

Comments

Signature

Date

Figure 3. *A proposed report checklist for COPD after minor modifications.*

Participants' conclusion: The meeting suggested that the slice thickness for CT scans should be 1.5 mm or less, rather than the previously suggested 1 mm or less, depending on the performance of the CT machine. All panel members concurred with the other CT parameters specified in the protocol and endorsed the proposed checklist, subject to minor modifications.

Agenda 2: Suggesting reporting guidelines for chest imaging to screen for connective tissue disease-related interstitial lung disease (CTD-ILD)

presented by Chayanin Nitiwarangkul

The increasing prevalence of lung fibrosis has raised concerns among referring physicians regarding the adequacy of information provided in certain HRCT reports for subsequent clinical decision-making. In response, HRCT report guidelines were established at the 2023 annual meeting of thoracic radiologists in Thailand and documented in The ASEAN Journal of Radiology under the title "The Report from the 2023 annual meeting of thoracic radiologists in Thailand: The development and reviews of the standards, guidelines, and advice concerning diagnostic radiology of thoracic disorders in Thailand" [4]. In Thailand, the most common cause of interstitial lung disease (ILD) is connective tissue disease (CTD), with lung fibrosis being the leading cause of death among these patients [5]. Despite this, there are no clear guidelines for screening and follow-up imaging. Each imaging modality has its strengths and limitations:

Chest radiography is the most widely available and accessible imaging method [6]. However, its relatively low sensitivity (around 60-80%) [6] may make it less effective for early disease screening. Nonetheless, due to the limited accessibility of HRCT, chest radiography remains a useful tool for initial screening and for evaluating intra-thoracic complications in patients with CTD-related ILD.

HRCT is recognized as the gold standard for diagnosing interstitial lung disease (ILD), with a sensitivity exceeding 90% and specificity over 95% [7]. Despite its advantages in detecting subtle changes, monitoring disease progression, and providing detailed assessments of patterns, extent, and severity, limited accessibility and higher radiation doses compared to chest radiography remain challenges, particularly in Thailand. While ultralow-dose HRCT has been explored to reduce radiation exposure, its reduced image quality can compromise diagnostic accuracy [8, 9]. The 2023 guidelines from the American College of Rheumatology (ACR) and the American College of Chest Physicians (CHEST) conditionally recommend HRCT for initial screening and monitoring of ILD in patients with systemic autoimmune rheumatic diseases (SARDs) [10], although the proper HRCT protocol and ideal time interval for routine follow-up has yet to be determined.

Participants' conclusion: It is crucial to communicate clearly with treating physicians about the inadequacies of chest radiography in effectively detecting or characterizing ILD, which may result in conditions being undiagnosed or underestimated. Additionally, discussions need to address the radiation dose of CT scans, the proper timing and criteria for initiating screening, and determining the optimal frequency for follow-up screening should be conducted.

Agenda 3: Revisiting the post-implementation accuracy of the proposed visual scoring method for quantifying global disease and fibrotic extents on HRCT

presented by Phakphoom Thiravit

The meeting revisited the 2022 annual meeting publications, which outlined the recommended HRCT estimation methods for evaluating global disease and fibrotic extents of ILD in Thailand [11-13]. These methods are categorized based on anatomical HRCT levels. Method 1, proposed by Sanchez et al., utilizes three anatomical landmarks [14]. Method 2, introduced by Well et al., expands this to five levels for a more detailed assessment [15]. Method 3, introduced by Goh et al., also utilizes a 5-level system but with different anatomical reference points [16]. Method 4, developed by chest radiologists in Thailand, incorporates six anatomical levels by retaining the upper 5 levels from Method 3 and adding an additional level below the diaphragm, allowing a more comprehensive evaluation [13]. This progression demonstrates the evolution of HRCT estimation methods aimed at enhancing their accuracy and applicability in the ILD context, particularly addressing the disease's lower and basal lung predominance.

A follow-up publication in 2023 [4] evaluated the post-implementation effectiveness of these methods. This year’s meeting facilitated discussions on the outcomes of these practices and any necessary adjustments to the methods.

Using all four methods, chest radiologists from Siriraj Hospital conducted a comparative study to evaluate the fibrotic extent in idiopathic pulmonary fibrosis [unpublished study]. The study found that Method 1 had the highest mean score for global disease or fibrotic extents among the four methods tested, while Method 2 yielded the lowest mean score. Method 3 produced scores that were intermediate between Methods 1 and 2. Comparisons between Methods 3 and 4 revealed that Method 4 generally reported 10-15% more fibrotic extent than Method 3. Since the increase in fibrotic extent is likely attributed to level 6 in Method 4, which contains less lung parenchyma but is a frequent site for pulmonary fibrosis, the researchers proposed a correction factor of 0.3 for the score at this level. This adjustment aims to align the scores from Method 4 with those of other methods.

Participants’ conclusion: Further post-implementation review should be revisited in the next meeting to determine the necessity of modifying Method 4 by either removing level 4 (anatomical level between levels 3 and 5) or applying a correction factor of 0.3 to the score at level 6.

Agenda 4: Establishing nationwide collaboration to define DRLs for chest HRCT in Thailand

presented by Thitiporn Suwatanapongched

DRLs are established benchmarks for radiation doses in medical imaging aimed at optimizing patient safety, protecting against unnecessary exposure, and ensuring diagnostic efficacy [17-19]. In Thailand, the Department of Medical Sciences in the Ministry of Public Health published the national DRLs in Thailand 2023, providing comprehensive guidelines for various imaging modalities, including CT [20]. These guidelines serve as a primary reference for healthcare facilities to align their practices with national standards, minimizing radiation exposure while maintaining the diagnostic quality.

As chest HRCT plays a pivotal role in thoracic imaging, especially for diseases such as ILD and COPD [3, 7, 8, 10], establishing DRLs specific to chest HRCT is crucial. Although national DRLs for chest HRCT have been reported in various countries [21-26], no such benchmarks currently exist in Thailand. Implementing DRLs for chest HRCT in Thailand would help standardize practices, improve regulatory compliance, and enhance patient safety by minimizing cumulative radiation risks. Establishing DRLs requires addressing key factors, such as population-specific differences (e.g., adults vs. pediatric patients), and implementing simplified, size-adjusted benchmarks [17, 27, 28]. Discussions during the meeting underscored significant variability in practices across facilities, rapid advancements in CT technology, and the necessity of ongoing training for radiologists and technicians [19, 29]. By emphasizing continuous education and aligning with global best practices, this initiative aims to implement DRLs for chest HRCT in Thailand effectively. Such efforts will encourage long-term improvements in patient safety, diagnostic quality, and the standardization of thoracic imaging practices nationwide.

Participants' Conclusion: All participants agreed to collaborate in establishing and defining national DRLs for chest HRCT through the systematic collection of the computed tomography dose index volume (CTDIvol) and dose-length product (DLP) data, showing their readiness to contribute to this initiative.

Agenda 5: Proposing a simple Thai terminology to educate patients about PPF

presented by Wiwatana Tanomkiat

PPF is a recently introduced condition in clinical practice [30], characterized by a progressive ILD phenotype involving worsening lung scarring (fibrosis) over time. It is commonly associated with patients who have CTDs with lung involvement. PPF underscores the importance of proactive monitoring and timely interventions to prevent disease progression to severe or end-stage lung fibrosis, thereby improving patients' quality of life.

Currently, no Thai terminology clearly represents this condition, and the abbreviation "PPF" may be difficult for Thai patients to understand. To address this, the meeting proposed the term **"Pod Khaeng"** (ปอดแข็ง), translated as "Pulmonary Cirrhosis," for use in patient education. This term simplifies communication and aligns with the widely recognized Thai terminology for hepatic cirrhosis (ตับแข็ง), which is commonly understood to represent end-stage liver fibrosis. Additionally, "pulmonary cirrhosis" was historically used to describe the pathology of usual interstitial fibrosis [31-33].

The proposal to use "Pod Khaeng" was also supported by several key similarities between pulmonary cirrhosis and hepatic cirrhosis:

- **Pathological process:** Both conditions represent the final stage of various underlying diseases rather than being specific disease entities,
- **Dynamic progression:** Both are chronic and dynamic processes that can worsen over time, with progression patterns ranging from slow to rapid deterioration,
- **Morphological similarities:** Both share similar gross features, such as a reduction in the organ size and nodular surfaces (Figure 4),
- **Impact on life:** Both significantly affect health, daily life, and life expectancy.

By linking "Pod Khaeng" to the familiar concept of hepatic cirrhosis, Thai patients are more likely to understand the condition compared to the previously proposed term "ภาวะปอดเป็นพังผืดชนิดลุกลาม" (a literal description of PPF). Using this terminology would enhance patient education, improve communication, and raise awareness among patients and their families. It may help bridge the gap between complex medical terminology and patient understanding, fostering better engagement and improved management. Furthermore, it could serve as an effective tool to promote smoking cessation, encourage ILD monitoring, and facilitate timely management to mitigate PPF, particularly in patients with CTDs.

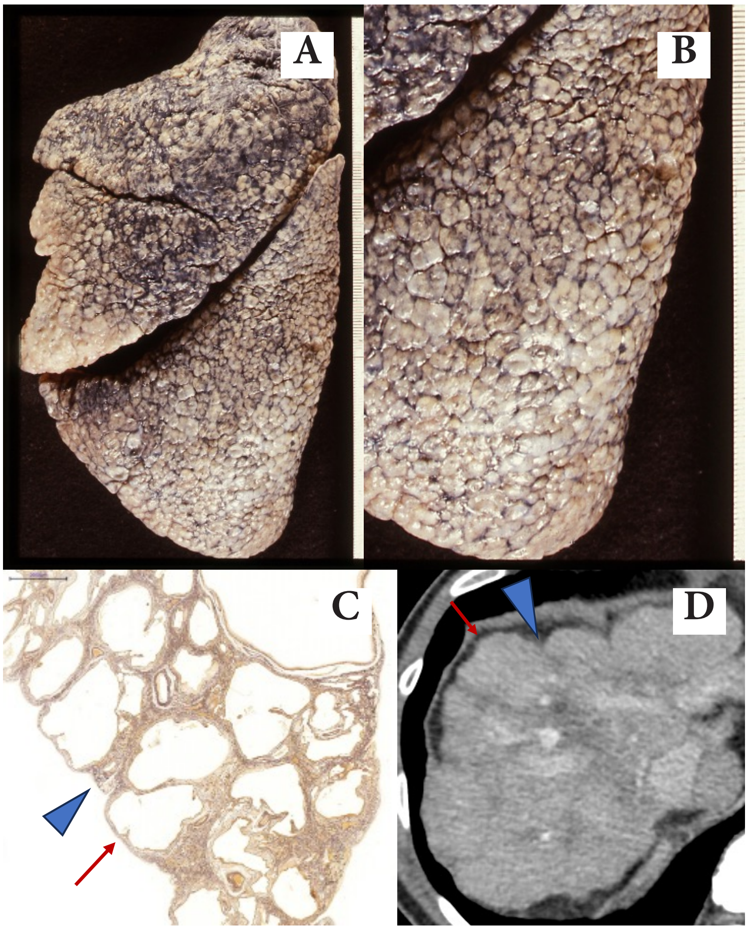

Figure 4. *Comparing pulmonary and hepatic cirrhoses; (A) Gross appearance of a lung with usual intersititial pneumonia (UIP) showing nodular surface similar to hepatic cirrhosis (B) Magnified gross surface and (C) cross section of the lung with UIP showing that the bulging nodules of the surface are the enlarged lobules (blue arrowhead) alternating with indented bands of fibrosis (red arrow) similar to (D) hepatic cirrhosis on CT; (Pictures A, B and C are courtesies of Dr. Tamiko Takemura).*

Participants' Conclusion: All participants agreed and suggested communicating with pulmonary physicians' societies to commonize the use of this term in patient education practice.

THE ASEAN JOURNAL OF RADIOLOGY
ISSN 2672-9393

Participant list:

Panelists

1. Wiwatana Tanomkiat	Songklanagarind Hospital, Prince of Songkla University.
2. Sitang Nirattisaikul	Songklanagarind Hospital, Prince of Songkla University.
3. Nantaka Kiranantawat	Songklanagarind Hospital, Prince of Songkla University.
4. Chayaporn Kaewsathorn	Surat Thani hospital, Office of Permanent Secretary, Ministry of Health.
5. Sutarat Tungsagunwattana	Central Chest Institute of Thailand, Department of Medical Services, Ministry of Public Health.
6. Krisna Dissaneevate	Rajavithi Hospital, Department of Medical Services, Ministry of Public Health.
7. Thitiporn Suwatanapongched	Ramathibodi Hospital, Mahidol University.
8. Warawut Sukkasem	Ramathibodi Hospital, Mahidol University.
9. Chayanin Nitiwarangkul	Ramathibodi Hospital, Mahidol University.
10. Narisara Chobaroon	Ramathibodi Hospital, Mahidol University.
11. Nisa Muangman	Siriraj Hospital, Mahidol University.
12. Kanyarat Totanarungroj	Siriraj Hospital, Mahidol University.
13. Phakphoom Thiravit	Siriraj Hospital, Mahidol University.
14. Krittachat Butnian	Siriraj Hospital, Mahidol University.

15. Wariya Chintanapakdee	King Chulalongkorn Memorial Hospital, Chulalongkorn University.
16. Itthi Itthisawatpan	King Chulalongkorn Memorial Hospital, Chulalongkorn University.
17. Nitra Piyavisetpat	King Chulalongkorn Memorial Hospital, Chulalongkorn University. Department of Radiology, MedPark Hospital.
18. Juntima Euathrongchit	Maharaj Nakorn Chiang Mai Hospital, Chiang Mai University.
19. Yuttaphan Wannasopha	Maharaj Nakorn Chiang Mai Hospital, Chiang Mai University.
20. Pakorn Prakaikietikul	Maharaj Nakorn Chiang Mai Hospital, Chiang Mai University
21. Panaya Tumsatan	Srinagarind Hospital, Khon Kean University.
22. Wannaporn Soontrapa	Srinagarind Hospital, Khon Kean University.
23. Watanya Jaidee	Faculty of Medicine, Burapha University.
24. Amolchaya Kwankua	Faculty of Medicine, Thammasat University.
25. Sornsupha Limchareon	Burapha University Hospital, Burapha University.

Observers

1. Apisada Siripraiwan	Songklanagarind Hospital, Prince of Songkla University.
2. Warat Setasuban	Songklanagarind Hospital, Prince of Songkla University.
3. Phum Inseeyong	Songklanagarind Hospital, Prince of Songkla University.

Meeting recorder	Chayaporn Kaewsathorn, MD.
Reviewer	Wiwatana Tanomkiat, MD.

References

1. World Health Organization [Internet]. Geneva: WHO; c2024 [cited 2024 Dec 22]. Chronic obstructive pulmonary disease (COPD), 6 November 2024. Available from: https://www.who.int/news-room/fact-sheets/detail/chronic-obstructive-pulmonary-disease-(copd)

2. Agusti A, Calverley PM, Celli B, Coxson HO, Edwards LD, Lomas DA, et al. Characterisation of COPD heterogeneity in the ECLIPSE cohort. Respir Res 2010;11:122. doi: 10.1186/1465-9921-11-122.

3. Stolz D, Mkorombindo T, Schumann DM, Agusti A, Ash SY, Bafadhel M, et al. Towards the elimination of chronic obstructive pulmonary disease: a Lancet Commission. Lancet 2022;400:921-72. doi: 10.1016/S0140-6736(22)01273-9.

4. Kaewsathorn C, Thiravit P, Piyavisetpat N, Nitiwarangkul C, Totanarungroj K, Tanomkiat W. The Report from the 2023 annual meeting of thoracic radiologists in Thailand: The development and reviews of the standards, guidelines, and advice concerning diagnostic radiology of thoracic disorders in Thailand. ASEAN J Radiol [Internet]. 2023 [cited 2024 Aug 11];24:320–39. Available from: https://www.asean-journal-radiology.org/index.php/ajr/article/view/890

5. Tanomkiat W, Areewattana N, Juthong S, Navaskulpong A, Siripaitoon B, Geater SL. High-resolution computed tomography (HRCT) disease patterns and survival times in patients with interstitial lung disease at a university tertiary hospital in Southern Thailand from 2006 to 2012. Asian J Med Radiol Res [Internet]. 2021 [cited 2024 Dec 23];9:80-6. Available from: https://aijournals.com/index.php/ajmrr/article/view/2205

6. Ghodrati S, Pugashetti JV, Kadoch MA, Ghasemiesfe A, Oldham JM. Diagnostic accuracy of chest radiography for detecting fibrotic interstitial lung disease. Ann Am Thorac Soc 2022;19:1934-7. doi: 10.1513/AnnalsATS.202112-1377RL.

7. Doshi JA, Mundhra KS, Shah DS, Shah SN, Patel TV, Bhatt A. Role of high-resolution CT thorax in diagnosing interstitial lung disease and its association with smoking and connective tissue disorder. Cureus 2022;14:e31107. doi: 10.7759/cureus.31107.

8. Ahmed S, Handa R. Management of connective tissue disease-related interstitial lung disease. Curr Pulmonol Rep 2022;11:86-98. doi: 10.1007/s13665-022-00290-w.

9. Hata A, Yanagawa M, Honda O, Miyata T, Tomiyama N. Ultra-low-dose chest computed tomography for interstitial lung disease using model-based iterative reconstruction with or without the lung setting. Medicine (Baltimore) 2019 ;98:e15936. doi: 10.1097/MD.0000000000015936.

10. Johnson SR, Bernstein EJ, Bolster MB, Chung JH, Danoff SK, George MD, et al. 2023 American College of Rheumatology (ACR)/American College of Chest Physicians (CHEST) guideline for the treatment of interstitial lung disease in people with systemic autoimmune rheumatic diseases. Arthritis Rheumatol 2024;76:1182-200. doi: 10.1002/art.42861.

11. Tanomkiat W, Nitiwarangkul (Thongprasert) C, Euathrongchit J, Thiravit P, Tongbai T, Suwatanapongched T. Multidisciplinary working group for interstitial lung disease in Thailand: Part 1-rationale in developing a guide to estimate the global disease and fibrotic extents on high-Resolution computed tomography. ASEAN J Radiol [Internet]. 2021 [cited 2024 Dec 22];22(3):47-60. Available from: https://www.asean-journal-radiology.org/index.php/ajr/article/view/158

12. Euathrongchit J, Thiravit P, Tanomkiat W, Nitiwarangkul C, Tongbai T, Wannosopha Y, et al. Multidisciplinary working group for interstitial lung disease in Thailand: Part 2 – a concise review of published visual scoring methods for interstitial lung disease. ASEAN J Radiol [Internet]. 2022 [cited 2024 Dec 22];23:42-55. Available from: https://www.asean-journal-radiology.org/index.php/ajr/article/view/170

13. Suwatanapongched T, Nitiwarangkul C, Euathrongchit J, Thiravit P, Tongbai T, Tanomkiat W. Multidisciplinary working group for interstitial lung disease in Thailand: Part 3 – the proposed visual scoring method for quantifying the global disease and fibrotic extents on high-resolution CT. ASEAN J Radiol [Internet]. 2022 [cited 2024 Dec 22];23:56-65. Available from: https://www.asean-journal-radiology.org/index.php/ajr/article/view/171

14. Sánchez RP, Fernández-Fabrellas E, Samper GJ, Montañana MLD, Vilar LN. Visual HRCT score to determine severity and prognosis of idiopathic pulmonary fibrosis. Int J Respir Pulm Med 2018;5:084. doi.org/10.23937/2378-3516/1410084.

15. Wells AU, Hansell DM, Corrin B, Harrison NK, Goldstraw P, Black CM, et al. High resolution computed tomography as a predictor of lung histology in systemic sclerosis. Thorax 1992;47:738-42. doi: 10.1136/thx.47.9.738.

16. Goh NS, Desai SR, Veeraraghavan S, Hansell DM, Copley SJ, Maher TM, et al. Interstitial lung disease in systemic sclerosis: a simple staging system. Am J Respir Crit Care Med 2008;177:1248-54. doi: 10.1164/rccm.200706-877OC.

17. International Atomic Energy Agency. Patient radiation exposure monitoring in medical imaging. Safety reports series no. 112. Vienna: IAEA; 2023.

18. Vañó E, Miller DL, Martin CJ, Rehani MM, Kang K, Rosenstein M, et al. ICRP publication 135: Diagnostic reference levels in medical imaging. Ann ICRP 2017;46:1-144. doi: 10.1177/0146645317717209.

19. Malik MMUD, Alqahtani M, Hadadi I, AlQhtani AGM, Alqarni A. An analysis of computed tomography diagnostic reference levels in India compared to other countries. Diagnostics (Basel) 2024;14:1585. doi: 10.3390/diagnostics14151585.

20. National diagnostic reference levels in Thailand 2023. Nonthaburi: Ministry of Public Health; 2023. Thai.

21. Qurashi AA, Rainford LA, Foley SJ. Establishment of diagnostic reference levels for CT trunk examinations in the western region of Saudi Arabia. Radiat Prot Dosimetry 2015;167:569-75. doi: 10.1093/rpd/ncu343.

22. Salama DH, Vassileva J, Mahdaly G, Shawki M, Salama A, Gilley D, et al. Establishing national diagnostic reference levels (DRLs) for computed tomography in Egypt. Phys Med 2017;39:16-24. doi: 10.1016/j.ejmp.2017.05.050.

23. Amalaraj T, Satharasinghe D, Pallewatte A, Jeyasugiththan J. Establishment of national diagnostic reference levels for computed tomography procedures in Sri Lanka: first nationwide dose survey. J Radiol Prot 2022;42(2). doi: 10.1088/1361-6498/ac40e8.

24. Bouchareb Y, Al-Maimani A, Al-Balushi AY, Al-Kalbani M, Al-Maskari H, Al-Dhuhli H, et al. Establishment of diagnostic reference levels in computed tomography in two large hospitals in Oman. Radiat Prot Dosimetry 2023;199:2148-55. doi: 10.1093/rpd/ncad225.

25. Kahraman G, Haberal KM, Ağıldere AM. Establishment of local diagnostic reference levels for computed tomography with cloud-based automated dose-tracking software in Türkiye. Diagn Interv Radiol 2024;30:205-11. doi: 10.4274/dir.2023.232265.

26. UK Health Security Agency [Internet]. UKHSA-RCE-1: doses from computed tomography examinations in the UK: 2019 review. [cited 2024 Dec 22]. Available from: https://assets.publishing.service.gov.uk/media/62b19331e90e0765d523ca5f/UKHSA-CT-report.pdf

27. Smith-Bindman R, Yu S, Wang Y, Kohli MD, Chu P, Chung R, et al. An image quality-informed framework for CT characterization. Radiology 2022;302:380-9. doi:10.1148/radiol.202121059.

28. Rawashdeh M, Saade C, Al Mousa DS, Abdelrahman M, Kumar P, McEntee M. A new approach to dose reference levels in pediatric CT: age and size-specific dose estimation, Radiat Phys Chemist 2023:205:110698.

29. American College of Radiology [Internet]. Reston (VA): ACR; c2024-2025 [cited 2024 Dec 22]. ACR appropriateness criteria. Radiation dose assessment introduction. Available from: https://www.acr.org/-/media/ACR/Files/Appropriateness-Criteria/RadiationDoseAssessmentIntro.pdf

30. Raghu G, Remy-Jardin M, Richeldi L, Thomson CC, Inoue Y, Johkoh T, et al. Idiopathic pulmonary fibrosis (an update) and progressive pulmonary fibrosis in adults: An official ATS/ERS/JRS/ALAT clinical practice guideline. Am J Respir Crit Care Med 2022;205:e18-e47. doi: 10.1164/rccm.202202-0399ST.

31. Hirshfield HJ, Krainer L, Coe GC. Cystic pulmonary cirrhosis (bronchiolar emphysema): (muscular cirrhosis of the lungs), Dis Chest 1962;42:107-10. doi: 10.1378/chest.42.1.107.

32. Davies D, MacFarlane A, Darke CS, Dodge OG. Muscular hyperplasia ("cirrhosis") of the lung and bronchial dilatations as features of chronic diffuse fibrosing alveolitis. Thorax 1966;21:272-89. doi: 10.1136/thx.21.3.272.

33. Sante LR. Cirrhosis of lungs. Radiology 1924;3:91-182.

Memorial

Received 27 April 2024; accepted 22 December 2024
doi:10.46475/asean-jr.v25i3.908

Professor Emeritus Charindr Eurvilaichit, 1944-2024.

On March 16, 2024, Professor Emeritus Charindr Eurvilaichit passed away at the age of 79 years. He was born on December 18, 1944. He graduated from the Faculty of Medicine Ramathibodi Hospital, Mahidol University before receiving the American Board of Diagnostic Radiology from Beth Israel Medical Center, New York, USA, in 1978, and the Certificate of Fellowship in Cardiovascular Radiology from Downstate Medical Center, New York, USA, in 1979.

After completing the training program, Professor Charindr worked as an instructor in the Department of Radiology, the Faculty of Medicine, Ramathibodi Hospital, Mahidol University. He was a highly esteemed and deeply respected senior faculty member in the field of Vascular and Interventional Radiology (VIR). Besides his expertise in VIR, his profound knowledge of contrast agents was legendary. He had many national and international publications as well as standard textbooks. He authored the first comprehensive textbook on vascular radiology in Thailand, "Angiography," a landmark achievement that served as a cornerstone for generations of medical professionals in the field of VIR. It has been used as the reference for training and practice since 1999.

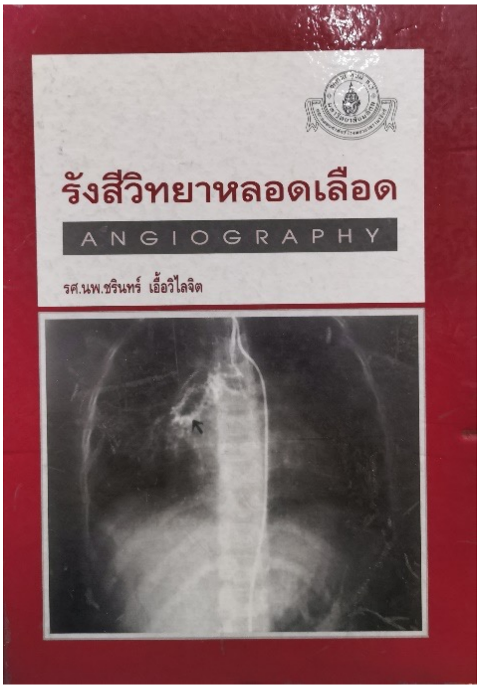

His work significantly shaped the landscape of interventional radiology in the country, establishing him as one of the pioneers of this field in Thailand. He was also a committee member of the Thai Society of Vascular and Interventional Radiology (TSVIR) until his retirement.

Image courtesy of http://live.siammedia.org/index.php/society/101008.

Beyond his remarkable professional accomplishments, Professor Charindr was a loving father and a dedicated family man. We extend our deepest condolences to his family. He will be missed and eternally honored.

Keerati Hongsakul, M.D.
President, Thai Society of Vascular and Interventional Radiology (TSVIR)

Krisna Dissaneevate, M.D.
Registrar, Royal College of Radiologists of Thailand (RCRT)

Wiwatana Tanomkiat, M.D.
President, Radiological Society of Thailand (RST)

ASEAN

This journal provide 4 areas of editorial services: language editing, statistical editing, content editing, and complete reference-citation check in 8 steps:

Step	Services to authors	Services providers
I	Manuscript submitted	Editor
II	Language editing/ A reference-citation check	Language consultant/Bibliographer
III	First revision to ensure that all information remains correct after language editing	Editor
IV	Statistical editing	Statistical consultant
V	Content editing*	Three reviewers
VI	Second revision	Editor
VII	Manuscript accepted/ rejected	Editor/Editorial board
VIII	Manuscript published	Editorial office

*Content editing follows a double-blind reviewing procedure

JOURNAL OF RADIOLOGY